Thermometry and Cooling of Ultracold Atoms in an Optical Lattice

by

Patrick Medley

Submitted to the Department of Physics
in partial fulfillment of the requirements for the degree of

Doctor of Philosophy

at the

MASSACHUSETTS INSTITUTE OF TECHNOLOGY

June 2010

Author .....
Department of Physics
June 8, 2010

Certified by .....
Wolfgang Ketterle
John D. MacAurther Professor of Physics
Thesis Supervisor

Certified by .....
David Pritchard
Cecil and Ida Green Professor of Physics
Thesis Supervisor

Accepted by .....
Krishna Rajagopal
Professor of Physics, Associate Department Head for Education

Thermometry and Cooling of Ultracold Atoms in an Optical Lattice

by

Patrick Medley

Submitted to the Department of Physics
on June 8, 2010, in partial fulfillment of the
requirements for the degree of
Doctor of Philosophy

Abstract

Ultracold atoms of ^{87}Rb were prepared in a mixture of two hyperfine states, $|F = 1, m_F = -1>$ and $|2, -2>$. This two-component system was then studied in the presence of a magnetic field gradient and an optical lattice.

The presence of a magnetic field gradient separated the atoms into regions of opposite spin, with a boundary region of mixed spin in the center. In the presence of an optical lattice, the width of this region was found to be proportional to the system's temperature and inversely proportional to the strength of the magnetic field. This allowed the measurement of the size of the boundary region to act as a thermometer for the system, representing the first demonstration of spin gradient thermometry. This thermometer represents the first practical method for thermometry in the Mott insulator, and has features of high dynamic range and tunable sensitivity. Given sufficient optical resolution and control over the magnetic field gradient, the lower limit of this thermometer is set by quantum magnetic ordering effects.

The dynamic response of this system to changes in magnetic field gradient was studied, both in the weak and strong lattice regimes. The result of these studies was the development of spin gradient demagnetization cooling. By performing an adiabatic drop in gradient strength while still in the superfluid, significant cooling of the entire system was observed. When the same process was performed in the Mott insulator, the spin temperature was cooled dramatically, while remaining out of equilibrium with the remaining degrees of freedom of the system. By reversing the gradient direction, inverted spin populations with negative temperatures have been produced. Spin gradient demagnetization has produced the closest approach to absolute zero yet recorded: 300 pK for the equilibrated system, and spin temperatures of 75 pK as well as -75 pK. The ability to achieve these temperatures puts studies of quantum magnetism in optical lattices within reach.

Thesis Supervisor: Wolfgang Ketterle

Title: John D. MacAurther Professor of Physics

Thesis Supervisor: David Pritchard
Title: Cecil and Ida Green Professor of Physics

Acknowledgments

My time at MIT has been an interesting one. Sometimes frusterating, but more often enjoyable, I will miss it greatly when I move on. There are many people who have helped brighten my time here, and I hope to give them some of the thanks they deserve.

First, I want to thank my thesis supervisors Wolfgang Ketterle and Dave Pritchard. Both have given me excellent guidance and advice over the years here at MIT. I have always been impressed with Wolfgang's perception of physics, and the sharp discussions I have had with him in group meetings have been very enlightening. As for Dave, I have been impressed with his insight, not just into physics, but into all manner of topics. When Dave spoke, it was rarely a dull topic.

The former members of the Rubidium lab that I worked with have also given me excellent guidance, and helped me develop the skills I have today. Gretchen Campbell and Erik Streed provided early guidance, and Gretchen especially played a crucial role in maintaining lab and group cohesion. The Ketterle-Pritchard group was never the same after she left. Micah Boyd, with whom I worked directly in my first couple years at MIT, was great fun to work with and introduced me to many things that have greatly enlivened my life. All three of these people were involved with the construction and early development of the Rubidium machine, and it is only as a result of their efforts early on that any of the work I have done could be accomplished.

After the three of them graduated, there was a vacuum in the Rubidium lab that Jongchul Mun and I had to fill. The time I spent working with Jongchul was both interesting and fun, and he was a great person to work with in lab. I also enjoyed having the chance to discuss all manner of things with him, both physics-related and not.

After Jongchul, in turn graduated, the Rubidium lab had four remaining members:

myself, postdoc David Weld, and two other graduate students, David Hucul and Hiro Miyake. David Hucul's early departure was very saddening for me and the other members of the lab, but I am sure he will find success in the future at Maryland. As for Hiro and David Weld, I could not imagine the latter half of my time at MIT without them. They have greatly brightened my time here as I have spent countless hours working alongside them. The time spent watching bits of television shows and enjoying internet silliness with them both while working late into the night running the machine is something without which my time would have been much less fun.

I am also greatful to the many members of BEC I, II, and III, and the other CUA labs along the hallway, for lending me so many pieces of optics and other tools, as well as having so much fun playing soccer and softball, and hanging out at conferences.

And of course, I'd like to thank my family for always being there for me. My parents, Mike and Carol, have always supported me in whatever I did, and allowed me to find my path in life. And my brother, Jonathan, who is currently also here at MIT, pursuing his own research in chemistry, has been the source of many great weekends playing games and having fun. And lastly, my fiancée Lara Rogers: thank you for your constant love, and for your patience during the long periods of time we had to spend apart. We shall be together soon.

Contents

List of Figures

List of Tables

Chapter 1

Introduction

1.1 From BEC to Optical Lattices

Fifteen years ago, Bose-Einstein Condensates (BEC) were first produced experimentally in atomic gasses [4, 19]. Their creation marked the opening of a new field of atomic physics involving the study of ultracold atoms. Initially, the field focused on measuring the properties of BEC themselves, but as time moved on the role of BEC expanded. No longer was it solely the subject of direct experimental study: it increasingly has become a tool used to enable the creation of other cold atomic systems. BEC have since been used in countless other roles. To count just a few: they have been used as a refrigerant to produce degenerate fermions, as a storage medium to slow and stop photons through electromagnetically induced transparency, and as a source of cold atoms to fill optical lattices.

It is this last use, to produce ultracold atoms in an optical lattice, that is the focus of this thesis, and that represents an important area in the future of atomic physics. While past studies of BEC, even many of those involving optical lattices, were often concerned with the properties of the superfluid state, optical lattices also point the way toward an area beyond superfluidity: static but highly-ordered, crystal-like

structures where superfluidity is left behind. Traditionally the realm of condensed-matter physics, the advent of optical lattices puts the study of crystalline ordering within the grasp of the atomic physicist as well. Already the superfluid to Mott insulator transition has been the subject of thorough experimental study, and in the future, many new and exotic phases will be open for experimental study in deep optical lattices. As this field matures, the study of phases exhibiting magnetic ordering will be within reach, and the work presented in this thesis will represent a significant step in making the study of these phases possible.

1.2 Optical Lattices as a Simulation Tool

Whereas atomic physics once dealt primarily with dilute gasses of free-moving atoms, much of condensed matter physics deals with solids with essentially rigid crystal structures. The new states made possible by optical lattices provide an important link between these two fields. By subjecting a cloud of ultracold atoms to a precisely-tailored optical lattice potential, a wide range of crystal structures can be simulated using the atoms loaded from the condensate as a proxy for particles in a crystal lattice. This represents the possibility of a new frontier for the investigation of many-body physics [7, 48].

An optical lattice is created by subjecting a cloud of atoms to a standing wave of light. Via the AC Stark effect, this creates a periodic potential for the atoms. As atoms are attracted to the minima of this potential, they arrange themselves in a periodic structure similar to the structure of a crystal.

Optical lattices can offer many advantages over the direct probing of condensed matter systems. Optical lattices can be tailored to the specific problem you wish to solve, providing flexibility in the states and identities of the constituent atoms, the strength of their interactions, their dimensionality, and the geometry of the lattice

that holds them. Many of these properties can be changed continuously and independently, even in the course of a single experimental run. This makes it possible for a single atomic system to model many different types of condensed matter systems without the need to fabricate them individually. It also allows the creation of simple model systems that may be difficult to fabricate in solids in order to study particular phenomena of interest in a controlled manner. Already, many studies involving the Mott insulator transition have been made, and as research in optical lattice simulation continues, interest is growing in producing states that exhibit more complicated physics, such as magnetically ordered states. Achieving these sorts of states, however, presents significant new problems to be overcome, not just in engineering the necessary interactions, but also in producing systems cold enough to exhibit them.

1.3 Why Temperature Matters

To achieve a magnetically-ordered state, it is necessary to have at least two components- either two separate atomic species, or two states of the same species. The most straightforward such system to produce experimentally is a system of two spin states of a single atom in a cubic optical lattice. This system is described by the two component Bose-Hubbard model, and can give rise, under the appropriate conditions, to two types of ferromagnetic ordering, as well as antiferromagnetic ordering [21]. However, this potential also highlights the difficulties in achieving such orderings.

One of the clearest such difficulties is that of temperature. The acievement of lower temperature scales has consistently led to new advancements in physics, and the case of quantum magnetism is no exception. The strength of interactions between atoms in an optical lattice is much weaker than those between their condensed matter counterparts. As a result, extremely low temperatures, far below even the μK critical temperature for Bose condensation, are required before any magnetic effects could

reasonably be observed. For atoms of ^{87}Rb in a lattice deep enough to form a Mott insulator, this temperature is in the range of tens to hundreds of pK.

The low temperatures demanded by such systems are themselves a significant challenge, but of equal concern has been the lack of an effective method for measuring temperature in this regime. Temperatures as low as 450pK have been measured in atomic gasses before [46]; however, the method used to do so required the atoms to be in an unperturbed harmonic trap. The same method is unable to measure temperatures of atoms in the presence of a lattice. Other methods for measuring temperatures of atoms in an optical lattice have been tried, but they are largely unable to measure with precision temperatures as low as needed. [16, 29, 38, 51, 56]

This thesis presents a method that has been developed to solve this problem in a system of two spin components. Through the use of a carefully-controlled magnetic field gradient to induce low-energy modes of excitation in the distribution of spins, it becomes possible to image the Boltzmann distribution of those spins directly. The resulting spin gradient becomes a thermometer from which one can straightforwardly read out the temperature. Furthermore, experiments will be described in which this thermometer is transformed into a refrigerator, cooling the atoms to the lowest temperatures ever recorded.

1.4 The Rubidium Lab

This thesis describes experimental work performed in BEC IV, also known as Rubidium lab, as it is the only one of the machines in the Ketterle-Pritchard group to work with ^{87}Rb. While all of the current research efforts in the Rubidium lab (and all the results presented in this thesis) are focused on optical lattices, this was not the case when I first joined nearly six years ago. At that time, the lab had just published a paper on photon recoil in a dispersive medium [11], and still viewed itself largely

as a machine optimised to produce high atom number BEC. Indeed, some of the earliest projects I worked on as a junior student were still focused on the superfluid: an early experiment involving scattering of atom pairs from a condensate in a one-dimensional optical lattice potential [13] and an experiment involving the quantum Zeno effect [68].

However, as time passed, it became increasingly evident that optical lattices were the way of the future. The experiments I worked on involved systems of increasingly lower dimension: a two-dimensional potential created by radio frequency (RF) dressing of a magnetic trap [9], a one-dimensional magnetic tube potential above a hard disk platter [8], and ultimately, in "zero-dimensions" a measurement of the shell structure of the Mott Insulator state via RF spectroscopy [12].

The final project I worked on before beginning the experiments detailed in this thesis was a first step toward the ultimate goal of probing phase diagrams in optical lattices. In it, the transport properties of atoms in the presence of an optical lattice were studied using a moving lattice to simulate AC particle flow. The result was a phase diagram showing stable versus unstable flow as a function of lattice depth and speed [53]. This diagram was compared to theoretical predictions based on a mean field model [1], and the results showed excellent agreement. Additionally, these experiments allowed a precision measurement of the lattice depth of the Mott insulator transition.

While this result was a significant step forward, it also represented a kind of limit in the interesting physics that was available in a simple, single component lattice. To proceed further, into the realm of magnetic ordering, it was necessary to work with a second component. Furthermore, the temperature scale required to probe this kind of ordering—the superexchange tempreature scale—was a scale far colder than what had yet been achieved. The experimental work that this thesis comprises opens up this scale, providing both a method to measure these temperatures in the presence of

a lattice and a means by which these temperatures can be attained. The development of spin gradient thermometry and spin gradient demagnetization cooling represents an important step towards bringing together the fields of atomic and condensed matter physics. I can only hope that in the future this combined field will be as fruitful as it appears today.

1.5 Outline

The remainder of this thesis will have the following structure. Chapter 2 will discuss the basic theory underlying our experiments. It will begin with the theory of BEC, and then discuss the theory of optical lattices, including the one and two component Bose Hubbard models and the Mott insulator transition. Chapter 3 will cover the basic experimental procedures and the setup of the machine used in the production of ^{87}Rb BEC. The next two chapters will then describe two experiments performed to measure and lower the temperature of a system comprising an optical lattice loaded with ^{87}Rb atoms in two spin states. Chapter 4 describes how a thermometer was be created and used to measure temperatures in the presence of a lattice, resulting in the process of spin gradient thermometry. Chapter 5, meanwhile, discusses how this thermometer was used to cool atoms through the process of spin gradient demagnetization cooling, which has resulted in some of the coldest temperatures yet recorded.

Chapter 2

Theory of BEC and Optical Lattices

2.1 BEC in a Harmonic Trap without Interactions

Although all of the important experimental measurements described in this thesis occur outside of the pure superfluid state, in optical lattice potentials, the atoms begin as a BEC. Since the properties of BEC are important to the preparation of our atoms and their transferral into the optical lattice, I will devote the first two sections of this chapter to a brief overview of BEC. For a more thorough discussion of BEC, I refer you to previous theses from this group [9, 10, 52, 64], review articles [17, 18, 43, 44, 47], and books [32, 55, 60].

In this section, I will derive an exact expression for the critical temperature and condensate fraction for the simplest model of trapped bosons: that of a gas of non-interacting bosons in a harmonic potential. For a harmonic potential with trap frequencies ω_x, ω_y, and ω_z, the energy levels for noninteracting particles are given by equation 2.1. Recall that BEC occurred when the chemical potential μ became equal the ground state energy, which for the noninteracting case was set to zero. In the

case of interactions, however, the ground state energy is no longer zero, because it depends on interactions. However, we know that in a BEC, the ground state energy is equal to the chemical potential. Thus

$$E(n_x, n_y, n_z) = \hbar(\omega_x n_x + \omega_y n_y + \omega_z n_z) \tag{2.1}$$

If the gas is at temperature T and chemical potential μ, then the population in each energy state is given by the Bose Einstein distribution

$$p(n_x, n_y, n_z) = \frac{1}{\exp(\frac{E(n_x,n_y,n_z)-\mu}{k_B T}) - 1} \tag{2.2}$$

and the total number is then

$$N = \sum_{n_x,n_y,n_z} \frac{1}{\exp(\frac{E(n_x,n_y,n_z)-\mu}{k_B T}) - 1} \tag{2.3}$$

As the temperature of the system is lowered, the chemical potential (which is necessarily negative) must rise to maintain constant total number. Eventually, the chemical potential will reach zero and the expression for the population in the ground state, $p(0, 0, 0)$ will diverge. The temperature at which this will occur is the critical temperature for Bose-Einstein condensation, and can be calculated by solving equation 2.3 for T when μ is set to zero. In the limit of large N, so we can treat the above sum as an integral over energy times a density of states ($\sum_{n_x,n_y,n_z} \rightarrow \int d\epsilon \frac{\epsilon^2}{2\hbar^3\omega_x\omega_y\omega_z}$), the critical temperature is given by

$$k_B T_c = \hbar\omega_{ho}(N/\zeta(3))^{1/3} \tag{2.4}$$

where $\omega_{ho}^3 = \omega_x\omega_y\omega_z$ and $\zeta(3) \approx 1.202$ is the Riemann Zeta function. in our experiments with ^{87}Rb, this temperature will be typically be $300 - 400$ nK. At and below

this temperature, the distribution of particles changes so that the population of the ground state and the excited states are described differently. The population of each excited state is still given by equation 2.2, but the fraction of atoms in the ground state—the condensate fraction—is now

$$N_0/N = (1 - (T/T_c)^3). \tag{2.5}$$

2.2 The Effect of Interactions

The approximation of the trapping potential as harmonic is reasonably accurate—the actual potential produced in the experiments described in following chapters is the sum of two gaussians. The approximation of the atoms as noninteracting, however, is not so accurate. In reality, ^{87}Rb atoms do interact, albeit weakly. Under experimental densities and temperatures, only two-body s-wave scattering collisions will contribute to the overall potential, although three-body collisions contribute to loss processes and heating via recombination. The effective two-body potential generated by s-wave scattering interactions can be written in terms of the scattering length a_s and the distance between a pair of particles r_{12} as $U(r) = 4\pi\hbar^2 a_s/m\delta(r_{12})$. This adds an extra term to the original Hamiltonian, resulting in a corrected Hamiltonian given by

$$\hat{H} = \int d\vec{r}\hat{\psi}^\dagger(\vec{r})(\frac{\hbar^2}{2m}\nabla^2 + V_{trap}(\vec{r}) + \frac{4\pi\hbar^2 a_s}{m}\hat{\psi}^\dagger(\vec{r})\hat{\psi}(\vec{r}))\hat{\psi}(\vec{r}) \tag{2.6}$$

where V_{trap} is the trapping potential. For $T \ll T_c$ so that the thermal fraction can be neglected, and neglecting also quantum fluctuations, we can then describe the BEC as a single wavefunction $\psi(\vec{r})$ with the normalization condition $\int d\vec{r}|\psi(\vec{r})|^2 = N$. This wavefunction will then obey the Gross-Pitaevskii equation:

$$i\hbar\frac{\partial\psi(\vec{r},t)}{\partial t} = (\frac{\hbar^2}{2m}\nabla^2 + V_{trap}(\vec{r}) + \frac{4\pi\hbar^2 a_s}{m}|\psi(\vec{r},t)|^2)\psi(\vec{r},t). \tag{2.7}$$

To solve the Gross-Pitaevskii equation, we should first write it in a time-independent form, of the type $\hat{H}\psi = E\psi$. The energy of the condensate is the ground state energy, which can easily be derived by appealing to equation 2.3. Recall that BEC occurred when the chemical potential μ became equal the ground state energy, which for the noninteracting case was set to zero. In the case of interactions, however, the ground state energy is no longer zero, because it depends on interactions. However, we know that in a BEC, the ground state energy is equal to the chemical potential. Thus, we can insert it into the Gross-Pitaevskii equation to produce a time independent version:

$$\mu\psi(\vec{r}) = (\frac{\hbar^2}{2m}\nabla^2 + V_{trap}(\vec{r}) + \frac{4\pi\hbar^2 a_s}{m}|\psi(\vec{r})|^2)\psi(\vec{r}). \tag{2.8}$$

The final approximation to solve this equation is the Thomas-Fermi approximation: we throw out the kinetic term from equation 2.8. The resulting density distribution is then easy to calculate:

$$n(\vec{r}) = \frac{m}{4\pi\hbar^2 a_s}(\mu - V_{trap}(\vec{r})). \tag{2.9}$$

This approximaiton is valid as long as the ratio of kinetic energy to interaction energy is small. Then, the kinetic term will make no important correction to the density function. The length scale over which the kinetic term is important is given by the healing length ξ—for changes in the wavefunction occuring over a distance shorter than the healing length the kinetic term dominates over the interaction term. The healing length is thus the length scale over which these two terms are equal, or

$$\frac{\hbar^2}{2m\xi^2} = \frac{4\pi\hbar^2 a_s n}{m} \Rightarrow \xi = \frac{1}{\sqrt{8\pi n a_s}} \tag{2.10}$$

. The function of the healing length is to take any sharp edges in the density distribution given by the Thomas-Fermi approximation and transform them into a more-

or-less smooth transition over the width of the healing length. This will be important later on, as it will provide a limit to the resolution of the thermometry technique of chapter 4 when applied by the superfluid. As we shall see, the presence of a reasonably deep lattice eliminates this limitation by lowering the condensate fraction to the point that the Gross-Pitaevskii equation is no longer valid.

2.3 Atoms in Optical Potentials

2.3.1 Scattering Forces

An atom illuminated by a laser beam is subject to two different types of forces: scattering and dipole forces. In optical dipole traps and lattices, the dipole force is used to form potentials to trap atoms, while the scattering force leads to heating and is generally desired to be as small as possible. Scattering occurs as photons from the laser transfer the atom into an excited state, then the atom undergoes spontaneous emission, sending out a photon of the same energy in a random direction. Assuming, as is a good approximation for ^{87}Rb, that the atom has only one relevant transition to be excited, the scattering rate can be written in terms of the laser intensity I, the transition's saturation intensity I_{sat}, the detuning δ, and the transition's natural linewidth Γ:

$$\Gamma_{sc} = \frac{\Gamma}{2} \frac{I/I_{sat}}{1 + I/I_{sat} + (2\delta/\Gamma)}. \tag{2.11}$$

Each photon scattered imparts a momentum kick on the atom of $\hbar k$ in the direction of the laser beam, where k is the wavevector of the light, as well as an additional kick of $\hbar k$ in a random direction. The kick along the laser beam is used in instruments such as Zeeman slowers and magneto-optical traps to slow and cool atoms, but is not put to any use in dipole traps. The main reason for this is that the random kick leads

to heating, with a heating rate

$$\dot{U} = \frac{\hbar^2 k^2}{2m}\Gamma_{sc}. \tag{2.12}$$

For atoms at temperatures well below $1\mu K$, as is typical in experiments involving BEC, this heating usually dominates any cooling effect that can be harnessed, so the scattering rate should be made as small as possible.

2.3.2 Dipole Forces

The dipole force, on the other hand, has no dissipative component: it creates an ordinary conservative potential. The dipole force arises because the electric field of the light induces a dipole moment μ in the atom, which itself interacts with the electric field with interaction energy $U_{dip} = -\mu \cdot E$. The resulting shift in energy is known as the AC Stark effect and in the limit of large detuning is equal to

$$U_{dip} = \frac{\hbar\Gamma^2}{8\delta}\frac{I}{I_{sat}}. \tag{2.13}$$

The sign of the detuning determines the sign of the potential: blue-detuned light repels atoms from positions of high intensity, while red-detuned light attracts to those positions. This allows one to produce an optical dipole trap (ODT) by focusing a red-detuned laser beam, as the focus of the beam will be a point of maximum intensity. If a beam of wavelength λ is focused with a beam waist of w_0 it will have a Rayleigh range of $z_R = \frac{\pi w_0^2}{\lambda}$ and will create a potential near the focus of

$$V_{trap}(r, z) \approx V_0[1 - (\frac{r}{w_0})^2 - (\frac{z}{z_R})^2]. \tag{2.14}$$

All optical traps used to hold atoms in the experiments described in this thesis are formed by one or more such traps, produced using light at 1064 nm, which is far to the red of the nearest optical transition—the D lines of ^{87}Rb at 780 nm and 795 nm. This

large detuning is important to minimize scattering losses: note that while the dipole force drops as $1/\delta$, the scattering rate drops as $1/\delta^2$. Thus, a large detuning allows deep optical traps with very low scattering rates. Typical spontansous scattering rates even in very deep potentials are $0.01Hz$, making them essentially negligible.

2.4 Optical Lattices

While an ODT is a simple and straightforward use of the dipole force, a more interesting potential can be made by taking advantage of optical interference to produce a standing wave. If a laser beam is reflected back onto itself, it will create a standing wave with a node at the reflecting mirror. The total potential this standing wave creates is

$$V_{latt}(r,z) = 4V_0 \cos^2(kz)[1 - (\frac{r}{w_0})^2 - (\frac{z}{z_R})^2]. \tag{2.15}$$

In our experiments, a combination of ordinary ODT beams confines the atoms to a radius much smaller than the waist of the lattice beam, so the lattice potential may safely be treated as a uniform sine wave with depth $4V_0$. This depth is usually measured in recoils, where $E_{rec} = \frac{\hbar^2 k^2}{2m}$ for a laser with wavenumber k and an atom of mass m. By creating an optical lattice in each of three orthogonal dimensions, one creates a three-dimensional sine wave potential, where the wells are arranged like the atoms of a simple cubic crystal.

2.4.1 Band Structure

If we ignore the external potential, we can understand the behavior of particles in the abscence of interactions by solving the Hamiltonian of a single particle in a sine wave potential. In each dimension we can write:

$$H = -\frac{\hbar^2}{2m}\frac{\partial^2}{\partial x_i^2} + \frac{s_i E_{rec}}{2}(1 - \cos(2kx_i)) \tag{2.16}$$

where s_i is the lattice depth, measured in recoils, for each dimension (usually all dimensions have the same depth in our experiments, but this is not necessary). The Schrödinger equation then admits solutions in the form of Mathieu functions, or equivantly, by Bloch's theorem, in the form of functions [50]

$$F_{aq}[x] = e^{i\mu_{aq}x} P_{aq}(x) \tag{2.17}$$

where $\mu(a, q)$ is the Mathieu characteristic exponent, $a = E/Erec - s/2$, and $q = s/4$. As μ appears in the leading exponent as though it were a momentum, and indeed is equal to momentum in the limit of zero lattice depth, it is called the quasimomentum. The function P_{aq} is periodic with period π/k, and each function $F_{aq}[x]$ has a sister function $F_{aq}[-x]$ which is also a solution with the same energy but negative quasimomentum. These solutions are only normalizable if $\mu(a, q)$ is real, which is true only within certain ranges. This implies the existence of energy bands where particles below a certain threshold can only have energies within certain ranges. Figure 2.1 shows the appearance and growth of the first three energy bands as a function of lattice depth. It is often useful to rewrite $F_{aq}(x)$ in terms of the quasimomentum μ and band level n, forming the Bloch function $\psi_{\mu n}(x)$. Note that these functions also depend on the lattice depth s, even though it has been left off as an index.

2.4.2 Wannier Functions

While Bloch functions are useful for describing atoms in a shallow lattice and in the absence of interactions, as the lattice becomes deeper, and especially as interactions are taken into account, a delocalized wavefunction such as the Bloch function becomes less and less useful as a basis to describe the atoms. Increasingly, atoms are confined to a single site, and perhaps those adjacent to it, so an ideal basis would be one that was likewise localized. The Wannier functions provide just such a basis. For an atom

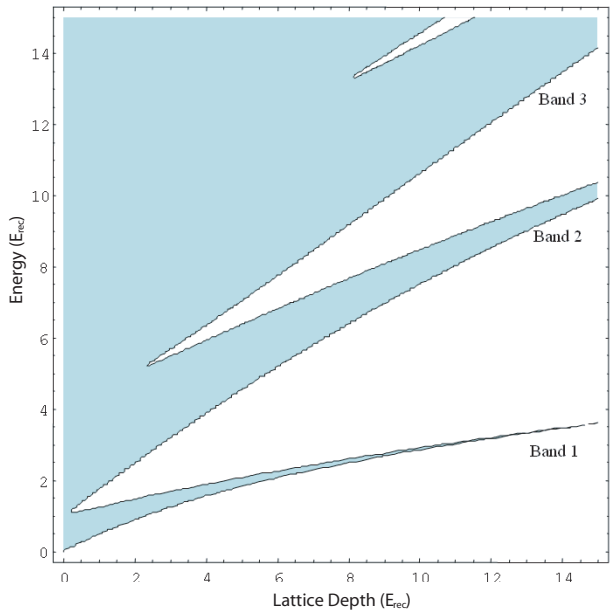

Figure 2-1: Bloch bands. Bloch bands begin to form with increasing lattice depth. This plot shows allowed energies in light blue and forbidden energies in white, as a function of lattice depth. The first three bands are labelled on the plot. Each band appears at a progressively higher lattice depth.

localized to the j^{th} lattice site and in the n^{th} band, the Wannier function is

$$w_{jn}(x) = \frac{1}{L}\int d\mu e^{-i\mu j}\psi_{\mu n}(x). \tag{2.18}$$

where L is the width of the band, and acts as a constant to normalize the wavefunctions. In experiments with ultracold atoms, nearly all of the atoms will find themselves in the lowest band, with a large energy gap separating the other bands at higher lattice depths, so we can generally take n to equal 1.

Using Wannier functions, we can finally begin to deal with interacting atoms in a lattice by producing a proper expression for tunneling and onsite interaction matrix elements. These matrix elements will be the key components in writing the Bose-Hubbard Hamiltonian. The tunneling matrix element J is given by the overlap integral between the Wannier functions of two adjacent sites as coupled by the Hamiltonian:

$$J_{ij} = \int dx w_i(x)(-\frac{\hbar^2}{2m}\frac{\partial^2 x}{\partial x^2} + V_{latt}(x))w_j(x). \tag{2.19}$$

The interaction matrix element, U, for a given site is the repulsion felt between two particles located at the same site. Recalling that the interaction term is $U(r) = 4\pi\hbar^2 a_s/m\delta(r_{12})$, we can easily write:

$$U_i = \frac{4\pi\hbar^2 a_s}{m}\int dx|w_i(x)|^4. \tag{2.20}$$

With these ingredients, we are finally ready to tackle the Bose-Hubbard Hamlitonian.

2.5 The Bose-Hubbard Model

The Bose-Hubbard model is a model for the Hamiltonian for atoms in an optical lattice that assumes that the energy of an atom at a particular site is the sum of three terms: the kinetic term, given by the tunneling matrix element to each adjacent site;

the onsite interaction term, given by the interaction energy between that atom and any others at the same site; and the external potential term $\epsilon_i = V_{trap}(x_i)$, which is the potential energy of the atom at that location given by whatever external trapping potential is imposed on top of the lattice. For a lattice potential that is relatively flat compared to the external trapping potential, so that U_i and J_{ij} are the same for all lattice sites, the full Bose-Hubbard Hamiltonian is then [42]:

$$H = -J \sum_{<i,j>} a_i^\dagger a_j + U/2 \sum_i n_i(n_i - 1) + \sum_i (\epsilon_i - \mu) n_i \tag{2.21}$$

where $a_i^\dagger$ and a_i are the creation and annihilation operator for an atom at site i and $n_i = a_i^\dagger a_i$ is the number operator at site i, while $< i, j >$ denotes the sum over all states $i \neq j$.

2.5.1 The Mott Insulator transition

As U and J are the only two energy scales imposed by the lattice in the Bose-Hubbard model, it is natural that the physics of this model depends on their ratio, given by the dimensionless interaction energy $u = U/J$. As the lattice depth increases, U rises linearly, while J falls exponentially. Thus, u rises exponentially with increasing lattice depth. To understand what happens to the ground state wavefunction as u rises, let us consider two extreme cases: the small u case, where $J \gg U$ and the large u case, where $U \gg J$.

The small u case corresponds to a vanishingly small lattice, and thus to a superfluid state. This state would be best described in the basis of Bloch states, but one can write it also in the Bose-Hubbard basis. In the limit of no interactions, each atom is independent, and is simply in the trap ground state. If the single particle ground

state wavefunction is $< x|\phi_g >= \phi_g(x)$, then the ground state for N particles is simply

$$|\psi_{SF} > \propto (\sum_i a_i^\dagger \phi_g(x_i))^N |0> . \tag{2.22}$$

If, as in the simplest case, $\phi_g(x)$ is a constant, we can easily see the expected behavior of a superfluid: phase coherence along with poissonian number fluctuations for each site. As the lattice raises, however, and J begins to vanish in favor of U, this phase coherence gives way to well defined values of atom number, and Fock states form the new basis for the ground state. The transition between these two limits is the Mott Insulator transition, and its ground state wavefunction

$$|\psi_{MI} > \propto \sum_i a_i^{\dagger n_i} |0> \tag{2.23}$$

where $\sum_i n_i = N$. The actual value of n_i is determined by the external potential and the chemical potential. We can think of filling each well with particles until the onsite energy equals the chemical potential minus the trapping potential. In other words, we can minimize the expression $E_i = U/2 n_i(n_i - 1) - (\mu - \epsilon_i)n_i$. Since n_i must be an integer, however, the actual expression for n_i moves in discrete steps:

$$n_i = \lceil \frac{\mu - \epsilon_i}{U} \rceil. \tag{2.24}$$

This simple expression is only valid in the limit as $J \to 0$—a more thorough analysis for nonzero J produces the phase diagram in figure 2.2. The actual point of the Mott insulator transition, where certain sites first stop showing number fluctuations, occurs for sites at the top of the $n = 1$ peak. The precise location of the Mott insulator transition is not easy to measure, and has been the subject of many experimental attempts [12, 24–26, 30, 42, 54, 66]. Nevertheless, a previous experiment performed in this lab [53] measured the transition to be at $u = 34.2 \pm 2.0$ for ^{87}Rb in a 3-dimensional

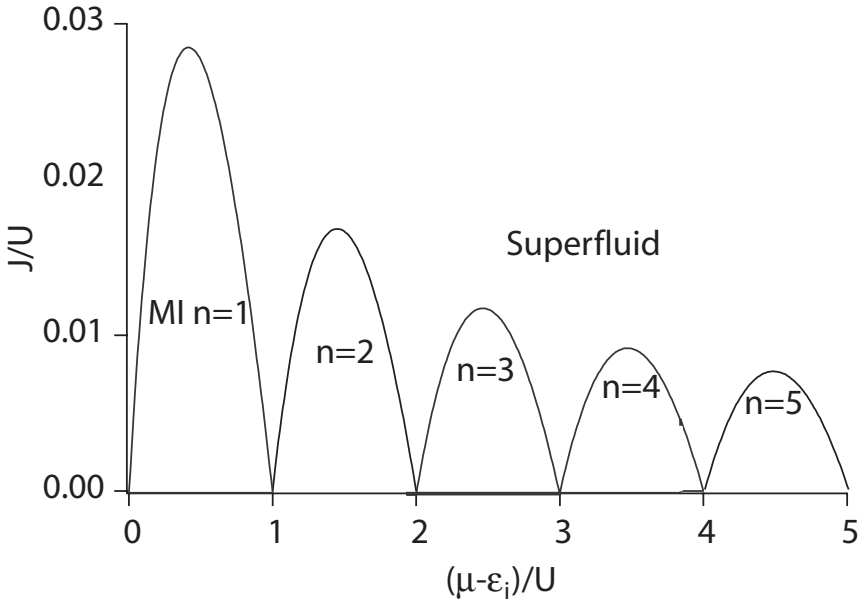

Figure 2-2: Phase diagram for the superfluid-Mott insulator transition. As J/U decreases, the system will undergo a phase transition into the Mott insulator. The system will form regions of superfluid and insulating regions with fixed atom number, determined by the value of $(\mu - \epsilon_i)/U$ at that lattice site. Higher chemical potentials lead to higher atom numbers at each site.

lattice made with light at $1064\mu m$, which occurs at a depth of $13.5 \pm 0.2 E_{rec}$. This result is in good agreement with the prediction of mean field theory [42], although it is lower than the predictions from quantum monte carlo [14, 28]. The measurement was precise, but may have had systematic errors affecting its accuracy, so the transition point may be slightly under the measured value. Nonetheless, it seems safe to say that any lattice above $14E_{rec}$ is well into the Mott insulator regime.

2.5.2 Excitation Spectrum

An important difference between the superfluid state and the Mott insulator can be seen in their different excitation spectra. The superfluid state has a continuous excitation spectrum described by Bogoliubov theory. In terms of momentum k, interaction

parameter $U_0 = 4\pi\hbar^2 a_s/m$ and density n, the excitation energy is [65]

$$\epsilon_k = \sqrt{(\frac{\hbar^2 k^2}{2m} + U_0 n)^2 - U_0^2 n^2}. \tag{2.25}$$

For small k this expression is approximately linear, implying excitations in the form of phonons with speed of sound $c = \sqrt{nU_0/m}$ while for high k we have free particle-like excitations with $\epsilon_k \approx \frac{\hbar^2 k^2}{2m} + nU_0$.

This continuous excitation spectrum stands in sharp contrast to the Mott insulator, whose excitation spectrum is gapped. Since the only variable determining the energy of a state in the deep Mott insulator is n_i, the only form an excitation can take is a change in distribution of n_i. For example, in an $n = 1$ Mott insulator, one site can be left vacant while another is occupied by two atoms. This can be thought of as a particle-hole excitation, as a "hole" is created in the form of an $n = 0$ site, while a "particle" is created in the form of an $n = 2$ site. Such an excitation is illustrated in figure 2.3, and has energy U.

Of course, in a real system, the inhomogeneous trap potential will cause different atoms to be at different effective chemical potentials. Looking in figure 2.2, any atoms that happen to be in the superfluid region will have continuous excitation spectra. In a harmonic trap, these atoms will be located around a particular radius determined by the trap frequency, forming ellipsoids of superfluid commonly referred to as superfluid "shells." However, for a reasonably deep lattice only a small fraction of the atoms will be located in positions to form superfluid shells; the remainder will exhibit a gapped excitation spectrum.

The effect of this gapped excitation spectrum is double-edged: on the one hand, for temperatures $k_B T \ll U$ there will be few excitations, giving a relatively pure system, but on the other hand, this freezing out of excitations makes it very difficult to read temperatures. Only the superfluid shell regions show significant responses to

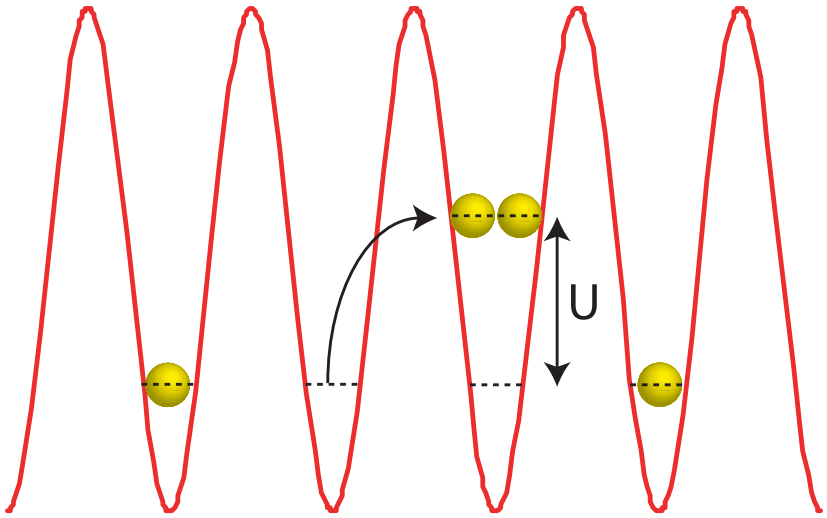

Figure 2-3: Mott insulator excitations. In the Mott insulator, the lowest energy excitation occurs when an atom tunnels to an adjacent lattice site. This lowers the original site's occupation number by 1 while raising the new site's by 1, at an energy cost of U, the onsite interaction energy.

temperature changes in this range, but they can be very small and difficult to resolve. As we shall see, using atoms in a different hyperfine state as a second component, a step necessary anyway for the observation of magnetic phenomena, provides a method to overcome this difficulty.

2.5.3 Two-Component Bose-Hubbard Model

The presence of a second type of atom modifies the Bose-Hubbard Hamiltonian in the following ways: for atoms numbered 1 and 2, we must introduce separate tunneling matrix elements J_1 and J_2 if the two components have different tunneling rates, and we must introduce different interaction energies U_{11}, U_{22}, U_{12} to represent the differences in inter- and intra-species interactions. The resulting Hamiltonian is then

$$H = -\sum_{<ij>,\sigma} J_\sigma a^\dagger_{\sigma i} a_{\sigma j} + \sum_{i,\sigma}(\frac{U_{\sigma\sigma}}{2} n_{\sigma i}(n_{\sigma i}-1) + U_{12}\sum_i n_{1i} n_{2i} + \sum_{i\sigma}(\epsilon_{\sigma i} - \mu_\sigma) n_{\sigma i} \quad (2.26)$$

where sigma represents the index 1 or 2. In our experiments, the two species will be two different hyperfine states of ^{87}Rb, the $|F = 1, m_F = -1 >$ state and the $|2, -2 >$ state, where F and m_F are the total spin and its projection along the axis of the local magnetic field. The value J can be manipulated by the appropriate choice of optical lattice: a spin dependent lattice can have different lattice depths for each state, and hence different J. Similarly, differences in U can be achieved either by using Feschbach resonances to manipulate the relative scattering lengths of the two species (recalling that $U \propto a_s$), or again by the use of specially engineered spin dependent lattices [39, 49]. In the experiments described here, however, no use is made of spin dependent lattices, so J is identical for the two species. Also, the scattering lengths of the two species are not manipulated, and the natural differences in scattering lengths for ^{87}Rb are very small. The only remaining term is the different potentials, $\epsilon_{\sigma i}$ felt by the species, and it is this term that is the key to allowing thermometry in the lattice. Nonetheless, it is instructive to briefly go over the resulting phase diagram for lattices in the case of variable J and U, as we will see what magnetically ordered phases will arise and why they require the very precise temperature control that is the subject of this thesis.

2.5.4 Phase Diagram Of the Two-Component Bose Hubbard Model

In the Mott Insulator regime, J is much less than U, so it is appropriate to expand the Hamiltonian perturbatively in J. Taking only terms out to order J^2/U, and ignoring the external potential, it is possible to use the Schrieffer-Wolf transformation [2,21,45] to write the Bose-Hubbard Hamiltonian in the form

$$H = \sum_{<ij>} \lambda_z \sigma_i^z \sigma_j^z - \lambda_\perp (\sigma_i^x \sigma_j^x + \sigma_i^y \sigma_j^y) + \sum_i h_z \sigma_i^z. \tag{2.27}$$

Here $\sigma_i^\mu = a_k^\dagger \sigma_{kl}^\mu a_l$ for the Pauli matrices σ_{kl}^μ, so $\sigma_i^z = n_{1i} - n_{2i}$ is the difference in number at site i. Similarly, σ_i^x gives the component of the net spin angular momentum pointing along the x-axis and σ_i^y along the y. The term h_z is a term proportional to the applied magnetic field plus a constant which may be neglected as a being an offset to the total field. Meanwhile λ_z and $\lambda_\perp$ can be written in terms of U and J as

$$\lambda_z = \frac{J_1^2 + J_2^2}{2U_{12}} - \frac{J_1^2}{U_1} - \frac{J_2^2}{U_2} \tag{2.28}$$

$$\lambda_\perp = \frac{J_1 J_2}{U_{12}}. \tag{2.29}$$

Depending on the values of λ_z, $\lambda_\perp$, and h_z, this Hamiltonian gives rise to a ground state in one of three different magnetically ordered phases: a z-ferromagnetically ordered phase, where all spins align along the direction of the applied magnetic field; an xy-ferromagnetically ordered phase, where the spins align orthogonal to the field; and an antiferromagnetically ordered phase, where spins are alternately aligned and anti-aligned to the field in a checkerboard pattern. Roughly speaking, as U_{12} drops relative to U_1 and U_2, the xy-ferromagnet tends to be favored over the z-ferromagnet, and as the tunneling difference $\beta = J_1/J_2 + J_2/J_1$ grows above its base value of 2, the antiferromagnet tends to be favored over the xy-ferromagnet. The resulting phase diagram is shown in figure 2.4.

Because these phases arise as a perturbative correction to the $J = 0$ model of the Mott insulator, the energy involved in creating them will be on the order of J^2/U. This scale is known as the superexchange energy, as it is the energy term involved in an interaction where a particle tunnels to an adjacent site, interacts with whatever particles are there, then returns. It is when the system is below this scale that it is possible for it to exhibit the ordering effects of quantum magnetism [35]. Various proposals [3, 22] have focused on the realization of quantum spin Hamiltonians in this regime. But the small value of this scale is a serious problem for atomic systems:

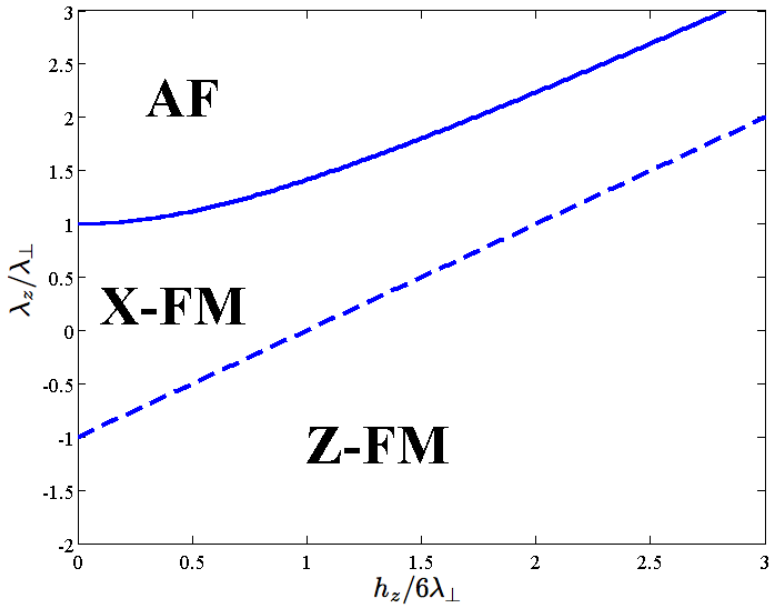

Figure 2-4: Two-component phase diagram. Two-component bosonic atoms in an optical lattice obey this phase diagram very low temperatures. The three phases depicted are labelled as follows: AF is the antiferromagnetic phase. X-FM is the xy-ferromagnetic phase. Z-FM is the z-ferromagnetic phase. The variables λ_z and $\lambda_\perp$ used in the axes are defined in equations 2.28 and 2.29, respectively, while h_z is the magnetic field. In the simplified case where J_1=J_2 and $U_{11} = U_{22} = U_\sigma$, the vertical axis is proportional to the ratio U_{12}/U_σ, plus a constant.

for ^{87}Rb in a lattice with average depth near the Mott insulator transition, recent quantum Monte Carlo calculations have shown the Curie temperature for the xy phase to be a mere 200 pK [15]. While the obvious answer might seem to be to raise J or lower U to make J^2/U larger, this would result in leaving the Mott insulator regime and the failure of our perturbative assumption: the system would instead be a superfluid, so we could no longer probe the phase diagram we wish to. Thus, we are left with little alternative but to find a way to measure lattice temperatures in the picoKelvin range, and find a way to produce such temperatures in experimental conditions. Although some cooling schemes have been proposed [6, 36, 57, 58], their implementation has not been easy. Chapters 4 and 5 will describe how these two goals have been achieved experimentally through the development of spin gradient thermometry and the use of adiabatic demagnetization cooling.

Chapter 3

Experimental Setup

In this chapter I will review the basic details involved in the preparation of ultracold ^{87}Rb atoms to be loaded into an optical lattice. The design of the experimental apparatus has already been clearly described in Refs. [67], [52], and [69], so I will only give a very brief description of the procedure for producing ultracold ^{87}Rb atoms. The ^{87}Rb machine is composed of an oven, Zeeman slower, and two chembers: the main chamber and the science chamber. The main chamber contains a Magneto-Optical Trap that catches and cools ^{87}Rb atoms exiting the Zeeman slower. The atoms are then optically pumped into the in the $|1, -1>$ hyperfine state and transferred to a magnetic trap. The atoms are evaporatively cooled to a temperature of a few times T_c before being loaded into an Optical Dipole Trap (ODT). This trap is produced by focusing a 1064 nm wavelength laser through a lens on a translation stage. The stage then moves the lens, translating the trapped atoms into the Science Chamber, where they are then transferred into another ODT.

3.1 Science Chamber Setup

The Science Chamber is a vacuum chamber connected to the main chamber and designed specifically for use with optical lattices. The design of this chamber is

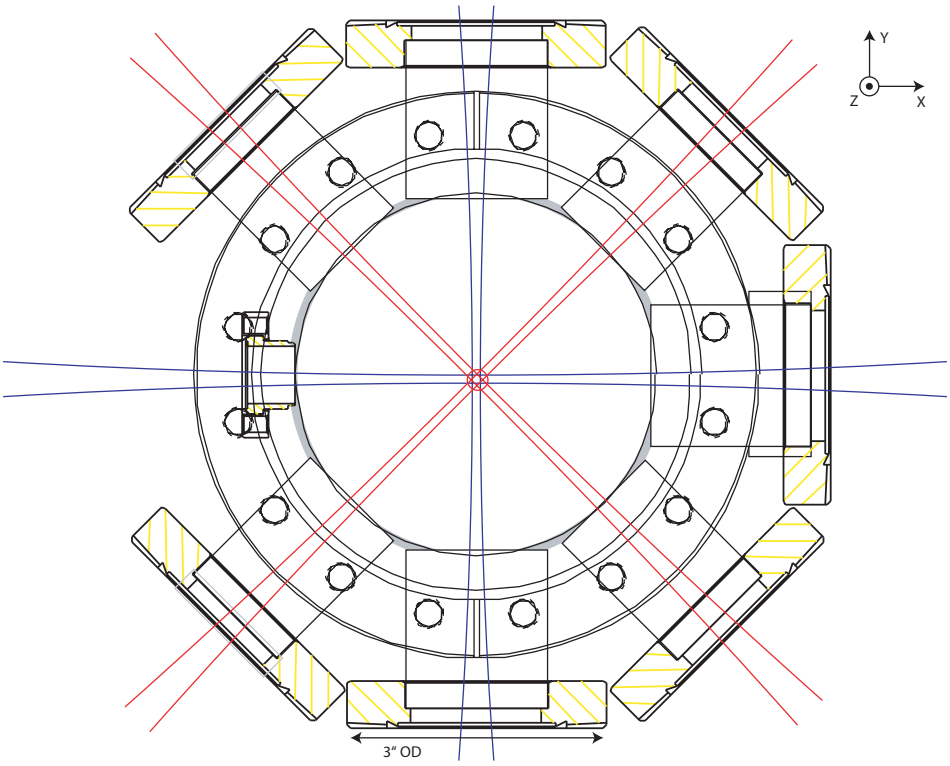

Figure 3-1: ODT and lattice diagram. This diagram shows the top view of the Science Chamber. The configuration shows optical dipole traps in blue and optical lattices in red. One lattice beam is oriented vertically through the atoms, coming out of the page.

described in detail in Ref. [52]. Atoms are delivered into this chamber from the Main Chamber using a translating ODT, then loaded into a crossed ODT formed by two horizontal beams aligned 90 degrees apart from each other. The depth of the trap of these two beams is lowered to evaporatively cool the atoms, and the atoms form a BEC. Aligned with the trap bottom created by these beams are three optical lattices, each formed by a retroreflected laser beam. One of the beams is vertical, while the other two are horizontal at 45 degrees from the beams of the crossed ODT. The configuration of these five beams is shown in figure 3.1.

All of these beams originate from the same source, a 1064 nm laser. The frequencies of these beams are offset by at least 3 MHz from each of the others using

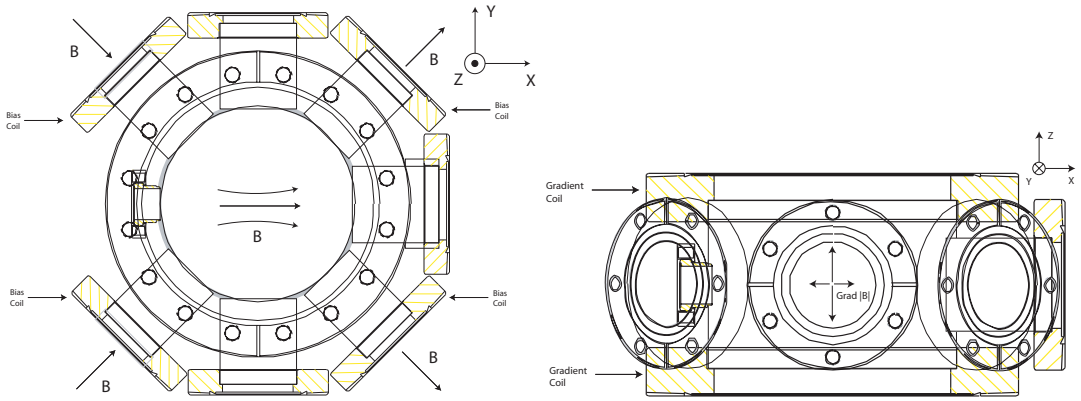

Figure 3-2: Magnetic field geometry. These diagrams show the configuration of magnetic bias fields and gradients generated by the Science Chamber coils. The left shows bias fields from a top view. The right shows a side view of $\nabla|\mathbf{B}|$ near the atoms in the *absence* of bias fields. With bias fields on, $\nabla|\mathbf{B}|$ points along x axis only.

Acousto-Optical Modulators so that any interference effects are at high frequency and will average out. The two optical dipole traps are given orthogonal polarizations, and each of the lattice beams is also given a polarization orthoganal to each of the other two so as to further minimize interference effects.

Magnetic field control is very important in our experiments, and it is performed using six bias coils. Four small coils in the horizontal plane are configured to provide a bias field of up to 15 G along the x-axis. Two larger coils, located above and below the chamber are arranged in an anti-Helmholtz configuration to produce a magnetic field gradient. In the presence of a strong bias field in the x direction, the gradient of the absolute value of the field, $\nabla|B|$, will point along the x-axis. In experiments, the strength of this gradient can be varied from 2 G/cm to -1 G/cm. Figure 3.2 shows the configuration of these coils and the fields they produce.

3.2 State Preparation and Gradient Evaporation

The Main Chamber produces atoms in the $|1,-1>$ hyperfine state, and the atoms remain in this state as they are transferred into the Science Chamber and evaporated to BEC. Since we wish to have atoms in a mixture of two states, we transfer a fraction of those atoms into the $|2,-2>$ hyperfine state. There are several reasons why the $|2,-2>$ state is an attractive choice for a second state. First, it is a stretched state in the same direction as the $|1,-1>$ state, so it cannot collide with a $|1,-1>$ atom, or with itself, and produce atoms in different hyperfine states. This means that the $|1,-1>/|2,-2>$ mixture acts as a two-spin system with conserved magnetization. Secondly, the transition from the $|1,-1>$ to the $|2,-2>$ state is a single photon magnetic transition, so it is easy to drive with microwave radiation while at the same time having an extremely long lifetime in the upper state. Finally, the two states have opposite g-factors, so they are pulled in opposite directions by a magnetic field gradient. This is important, because the interaction between spin and magnetic field gradients is critical to our experiments.

The transition between $|1,-1>$ and $|2,-2>$ is driven with microwaves using a rapid, nonadiabatic sweep of the magnetic field. A microwave signal at 6.844 GHz is mixed with an RF signal at 36 MHz to produce microwave radiation at 6.808 GHz (as well as a 6.880 GHz signal which is far off resonance and has no effect). The mixer allows the use of RF function generators to provide easy control of the frequency and intensity of the microwave radiation, but the same effect could be achieved using a single frequency microwave source at 6.808 GHz instead. The microwaves are fed into a microwave horn, which then exposes the atoms to radiation at that frequency. Meanwhile, the bias field is swept linearly from about 12 G to 13.5 G over the course of 20 ms. This sweep causes the resonance frequency of the atoms to pass over the frequency of the microwaves, transferring some, but not all, of the atoms to the $|2,-2>$ state. In the end, we want an equal mixture of the two states, but we

initially prepare an excess number of $|2,-2>$ atoms. The reason for this is that in the next step, gradient evaporation, the $|2,-2>$ atoms evaporate more rapidly due to their high magnetic moment. Thus, we overpopulate the $|2,-2>$ state initially so that after the evaporation the $|2,-2>$ atoms will be equal in number to the $|1,-1>$ atoms.

After preparing the two spin states, we then begin another round of evaporation in the presence of a magnetic field gradient. The gradient is turned on and increased to a strength of 2 G/cm and held for between 1 and 4 seconds as the atoms evaporatively cool. The reason for this extra evaporation step is that our state preparation adds a great deal of entropy to the system, and evaporation in the presence of a gradient can remove it [40]. The sweep is nonadiabatic, with the two states decohering within milliseconds, so each atom can basically be thought of as having a random spin, either $|1,-1>$ or $|2,-2>$. Thus, we have added entropy of around $k_B \ln 2$ per particle. This entropy can be mostly removed through gradient evaporation. Because the two states have opposite g-factors, they are pulled in opposite directions by the magnetic field: the $|1,-1>$ atoms toward the region of weaker field and the $|2,-2>$ atoms towards the region of stronger field.

As the spins segregate, their spin entropy decreases, changing into kinetic entropy in the form of heat. This heat is then removed by evaporation. Because the $|2,-2>$ atoms have twice the magnetic moment of the $|1,-1>$ atoms, they are pulled more strongly and evaporate more rapidly. The $|2,-2>$ population is initially made to be more than half so that after this process they are equal in number to the $|1,-1>$ atoms. Ultimately, in a stong gradient, the two spin states are completely separated on opposite sides of the cloud. Figure 3.3 shows a cartoon picture of this process. The state that results from this evaporation is then ready to be used in our experiments.

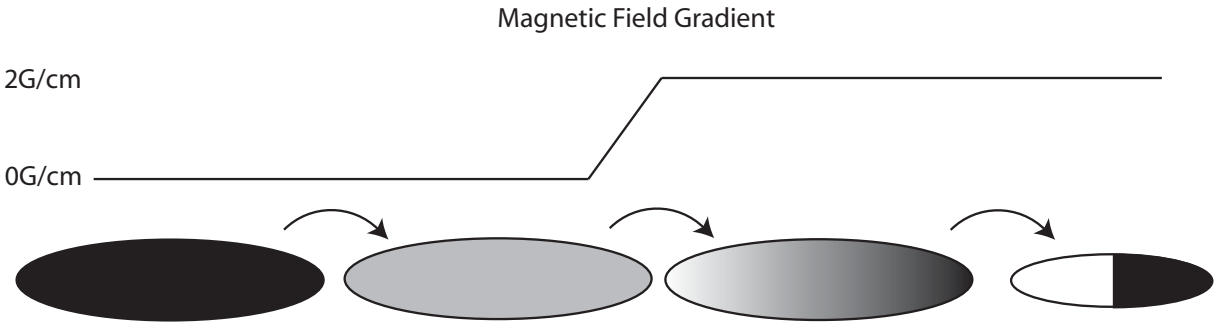

Figure 3-3: Gradient evaporation procedure. Atoms are initially in the $|1,-1>$ state (black) and zero magnetic field gradient. Roughly half of the atoms are then swept into the $|2,-2>$ state (white). The gradient is then ramped up to 2 G/cm, partially separating the two spins. As the atoms evaporate, the entropy added from state preparation is removed, and the spins segregate on opposite sides of the trap.

3.3 Imaging the Atoms

At the end of each experimental run, we image the atoms using resonant absorption imaging. The atoms are illuminated with light at 780 nm, resonant with the $F = 2$ to $F = 3$ cycling transition of ^{87}Rb. Any atoms in the $F = 2$ hyperfine level cast a shadow onto a camera—this image is the "probe with atoms" (PWA) frame. Two additional images are taken immediately afterwards, one with the same light pulse but no atoms, called the "probe without atoms" (PWOA) frame and one more frame without the light, called the "dark field" (DF) frame. The absorption image is then the ratio

$$ABS = \frac{PWA - DF}{PWOA - DF}. \tag{3.1}$$

The number of atoms in a given pixel $N(x, y)$ is then given by the equation

$$N(x,y) = -\frac{A \ln ABS}{\sigma_0}, \tag{3.2}$$

where A is the area of a single pixel and σ_0 is the resonant cross section. In-trap images are taken with a magnification factor of 10, and our camera has $13\mu m$ pixels,

so the area A for in-trap images is $(1.3\mu m)^2$. This basic equation can be used to generate a two dimensional image of atom number density; however, there are two corrections we use in processing images that improve the accuracy of of our absorption images.

3.4 Saturation Correction

The first correction involves saturation effects. Equation 3.2 is only valid in the limit of unsaturated imaging. As the light intensity approaches or exceeds the saturation intensity I_{sat}, that equation no longer remains accurate. The obvious solution would seem to be to always use light intensities well below saturation, but this is not always possible. Sometimes, especially when imaging dense clouds of atoms in-trap, the parts of the cloud we are interested in measuring are optically dense. When this is the case, unsaturated light will be almost entirely extinguished, so what signal does get through will be only a few counts per pixel—this will result in high noise and poor accuracy. In those cases, it is necessary to use much more intense light to retrieve any signal at all, but of course, the signal will no longer give the correct density if simply plugged into equation 3.2.

The solution is to use a correction term to cancel out the effects of saturation and retrieve the correct signal. To do this, we must know the properties of the atoms we are measuring and what the original intensity of the light was at each pixel. The first part is no problem, as the optical properties of ^{87}Rb are well understood. As for the second part, we can retrieve that information from the PWOA shot. We can then use an equation given by Ref. [59] to retrieve the real number of atoms:

$$N(x,y) = \frac{A}{\sigma_0}[\alpha \ln(\frac{PWA - DF}{PWOA - DF} - \frac{PWOA - PWA}{I_{sat}}]. \tag{3.3}$$

Here, I_{sat} is the saturation intensity, in units of camera counts per pixel and α is a cor-

rection factor that depends on a variety of factors such as imaging beam polarization and the structures of the upper and lower states. We determined α experimentally by imaging a constant number of atoms with different intensities of light. The best fit value was 2.1 for our primary imaging setup, and this value was used in all in trap shots to determine the correct atom number. For many of our experimental runs, specifically those performed with unsaturated light, the correction factor is basically negligible and equation 3.3 provides no more accurate informaiton than equation 3.2. Nonetheless, when imaging clouds with large atom number, the flexibility given by equation 3.3's correction helps significantly.

3.5 Principal Component Analysis Correction

While the saturation correction described above is a correction based on the interaction between ^{87}Rb atoms and light, there is a second correction we also make that involves only the laser. Specifically, the problem is the appearance of fringes arising from the division of the PWA by the PWOA images to obtain an absorption image. We normally assume that the only difference between the PWA and PWOA images is that the atoms are gone—in other words, that the intensity distribution of the laser is the same. But this is not necessarily true: the shots are taken about 1 second apart, and in this time the shape of the light may change. Imaging artifacts can arise due to vibrations in the different optics components, changes in intensity, and other effects. These give rise to fringes in the absorption image.

One way of thinking about this problem is that the PWOA shot is equal to what the PWA shot would have been in the absence of the atoms, plus some fringes that arise due to vibrations and other imperfections in the apparatus. Basically, what we want to know is not what the PWOA *was*, but rather what it *should have been.* We can make a good guess at what the PWOA should have been by looking at correlations

between different parts of an image. By masking off the part of the frame containing the atoms in the PWA, we can infer what that area would have been be comparing the rest of the image to a set of many PWOAs from different shots. We can then think of reconstructing the "true" PWOA as a weighted sum over the set of several different PWOAs, where the weighting coefficients are based on a comparison between the masked PWA and each PWOA in the set. The mathematical method of determining these coefficients is principal component analysis.

Principal component analysis can be used on a set of vectors to generate a principal component matrix [62, 63, 72]. In this case, the original set of vectors are the masked PWA shots and the (unmasked) PWOA shots. Let the principal component matrix be P, whose column vectors $\mathbf{p}_i$ are called the principal component vectors. The vectors are two-dimensional arrays of the same size as our images, and P has an additional dimension equal in length to the number of images used to generate it. Similarly, let us call the PWA image $\mathbf{I}_{PWA}$ and the PWOA image $\mathbf{I}_{PWOA}$, where again each vector is a two-dimensional array. These images are used to generate the principal component matrix. Finally, we choose a mask around the atoms, and so can break the PWA image into two parts, $\mathbf{I}_{PWA} = \mathbf{I}^{-}_{PWA} + \mathbf{I}^{0}_{PWA}$ where $\mathbf{I}^{0}_{PWA}$ is the masked off region—the part with the atoms. The correction prescribed by principal component analysis then depends on whether the fringes in an image arise due to elements in the beam path before or after the atoms.

3.5.1 Post-Atom Fringes

If the fringes arise from elements in the beam path after the atoms, then the correction is effectively one to the dark field of each of the probe beams. Each frame, the PWA and PWOA, must then be corrected. The corrected frames can be straightforwardly written as

$$\mathbf{I}'_{PWA} = \mathbf{I}_{PWA} - \sum_i (\mathbf{I}^{-}_{PWA} \cdot P)_i \mathbf{p}_i \tag{3.4}$$

$$\mathbf{I}'_{PWOA} = \mathbf{I}_{PWOA} - \sum_i (\mathbf{I}_{PWOA} \cdot P)_i \mathbf{p}_i \tag{3.5}$$

and the normalized absorption image is

$$\mathbf{I}'_{ABS} = \frac{\mathbf{I}'_{PWA} - \mathbf{I}_{DF}}{\mathbf{I}'_{PWOA} - \mathbf{I}_{DF}} \tag{3.6}$$

However, in our experiments, we find that this type of correction, being an additive correction of the same type as the dark field, does not significantly diminish the visible fringes. This is reasonable, as the path length between the atoms and camera is shorter, and contains fewer optical elements, than the path length leading up to the camera. Thus, the multiplicative form of correction, which accounts for pre-atom fringes, will be the one we use in the experiment.

3.5.2 Pre-Atom Fringes

When the fringes arise from elements in the beam path prior to the atoms, as we find to be the case in our experiment, then a multiplicative correction should be applied. This correction is only to the PWOA shot, and essentially involves first subtracting the fringes of the PWOA, then adding in the fringes of the PWA, so that in the end these fringes will divide out cleanly and give an accurate absorption image. The procedure is more complicated than the additive correction, proceeding in the following manner:

First, we must decompose the basis vectors $\mathbf{p}_i$ in the same manner as the PWA shots, writing $\mathbf{p}_i = \mathbf{p}_i^- + \mathbf{p}_i^0$ where $\mathbf{p}_i^0$ is the part of the basis vector under the mask. Next, we renormalize the remaining part of the basis vector by writing

$$\mathbf{p}'_i = \frac{1}{\sqrt{\mathbf{p}_i^- \cdot \mathbf{p}_i^-}} \mathbf{p}_i^- . \tag{3.7}$$

Now we can extract the principal component coefficients c_i from the PWA:

$$c_i = \mathbf{I}_{PWA} \cdot \mathbf{p}'_i. \tag{3.8}$$

Now, we are ready to correct the PWOA image in two steps.

In the first step, we subtract the fringes of the PWOA in the same way as we did for post-atom fringes:

$$\mathbf{I}'_{PWOA} = \mathbf{I}_{PWOA} - \sum_i (\mathbf{I}_{PWOA} \cdot P)_i \mathbf{p}_i. \tag{3.9}$$

In the second step, we then add to the PWOA the fringes that the PWA frame has, so that we may properly divide them out later:

$$\mathbf{I}''_{PWOA} = \mathbf{I}'_{PWOA} + \sum_i c_i \mathbf{p}_i. \tag{3.10}$$

Finally, the absorption image is given by

$$\mathbf{I}'_{ABS} = \frac{\mathbf{I}_{PWA} - \mathbf{I}_{DF}}{\mathbf{I}''_{PWOA} - \mathbf{I}_{DF}}. \tag{3.11}$$

The effect of using this image processing routine is to significantly reduce visible fringes in images. This allows a more accurate in-trap image of the atom cloud to be resolved. Figure 3.4 shows an example of a pair of frames before and after fringe removal. Principal component analysis requires many frames to be useful in subtracting fringes, so we use all the shots in a data set to produce the principal component matrix. One problem to keep in mind is that bad frames—those caused by camera malfunctions, for example—can cause the fringe subtraction routine to worsen, rather than improve, the images. We occasionally had such bad frames, and it was important to remove them prior to computing the principal component

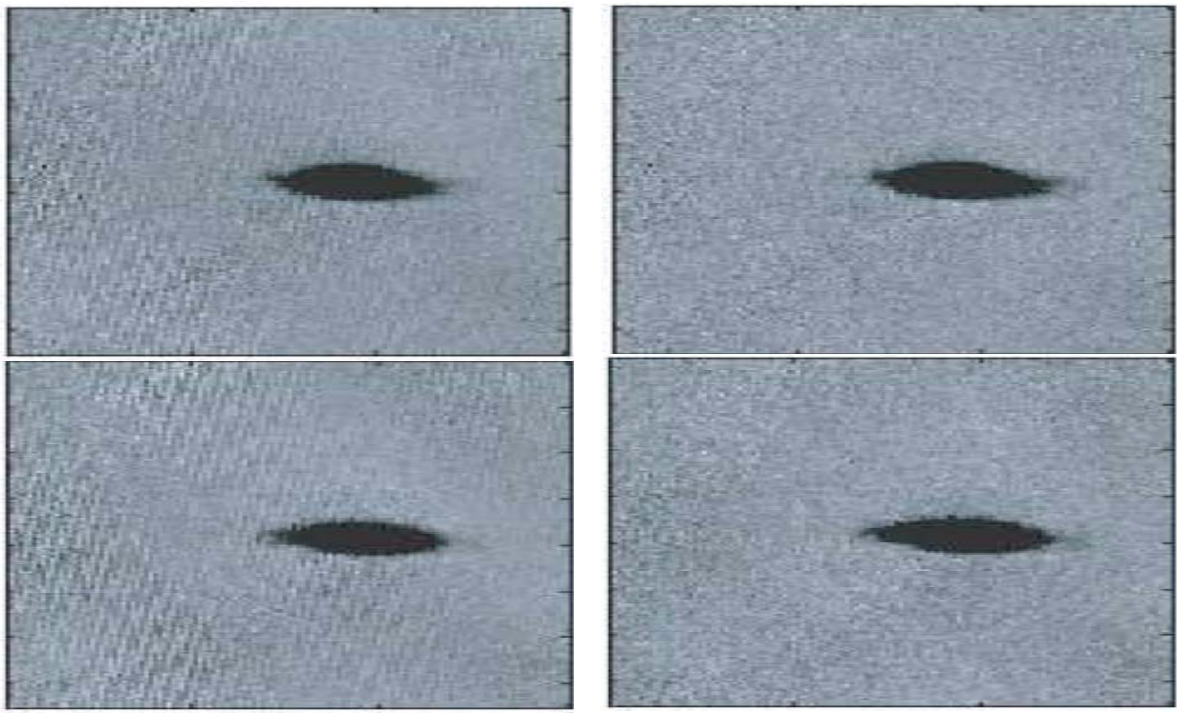

Figure 3-4: Fringe removal results. The left frames show absorption images of our atoms without fringe removal, while the right frames show the results of fringe removal using principal component analysis. Imaging artifacts are clearly removed (note, for example, the uneven "blotches" on the left part of the images which are gone in the corrected images), while the image of the atoms themselves is preserved.

matrix. Removing the bad frames afterwards is not sufficent, as they will contiminate the remaining frames through the erroneous matrix.

3.6 Magnetic Field Gradient Calibration

A final topic important to the experiments presented in the following chapters is the calibration of the magnetic field gradient. Precise control over the strength and direction of the magnetic field gradient, as well as accurate knowledge of the point at which the gradient strength is zero, are very important both for spin gradient thermometry and spin gradient demagnetization cooling. This section will describe the procedures used to calibrate all three of these.

The direction of the gradient must remain constant, in the x direction, over the full range of gradients used. To assure this, a strong bias field, of approximately 15 G, is maintained in the x direction. As long as this field is maintained, the direction of the gradient will stay constant, as any gradients in orthogonal directions will be quadratically suppressed. To see why, consider that we can expand the magnetic field to first order in $\vec{x}$ as

$$\vec{B} = B_0\hat{x} + \sum_i B_i'\vec{x_i} \tag{3.12}$$

where $B_i' = \frac{\partial B_i}{\partial x_i}$ is the gradient due to our antihelmholtz coils (other terms give rise to curvature and can be neglected for well-aligned coils). Then the magnitude of the magnetic field $|B|$ can be written

$$|B| = \sqrt{B^2} = \sqrt{B_0^2 + 2B_0B_x'x + \sum_i (B_i')^2 x_i^2}. \tag{3.13}$$

Finally, to get $\nabla|B|$, we expand the square root in the limit of large B_0 to get

$$\nabla|B| = B_x'\hat{x} + O(B'/B_0) \tag{3.14}$$

. Thus, we can treat $\nabla|B|$ as a single number value B', representing the strength of the gradient along the x axis, $\nabla|B|\cdot\hat{x}$.

To be sure that as we vary the strength of the gradient, we do not introduce magnetic field components in the $\hat{y}$ and $\hat{z}$ directions, we make a Stern-Gerlach measurement at various gradient strengths. The atoms are prepared in a mixture of $|2,-2>$ and $|1,-1>$ as described in section 3.2. The gradient is set to a variable value, then the trap holding the atoms is turned off, and the two atomic species separate in time of flight. As long as the atoms are separated along the same axis for all values of gradient applied, we know the gradient is along that axis alone. If they do not remain along the x axis, coils are adjusted and shimming currents are added until

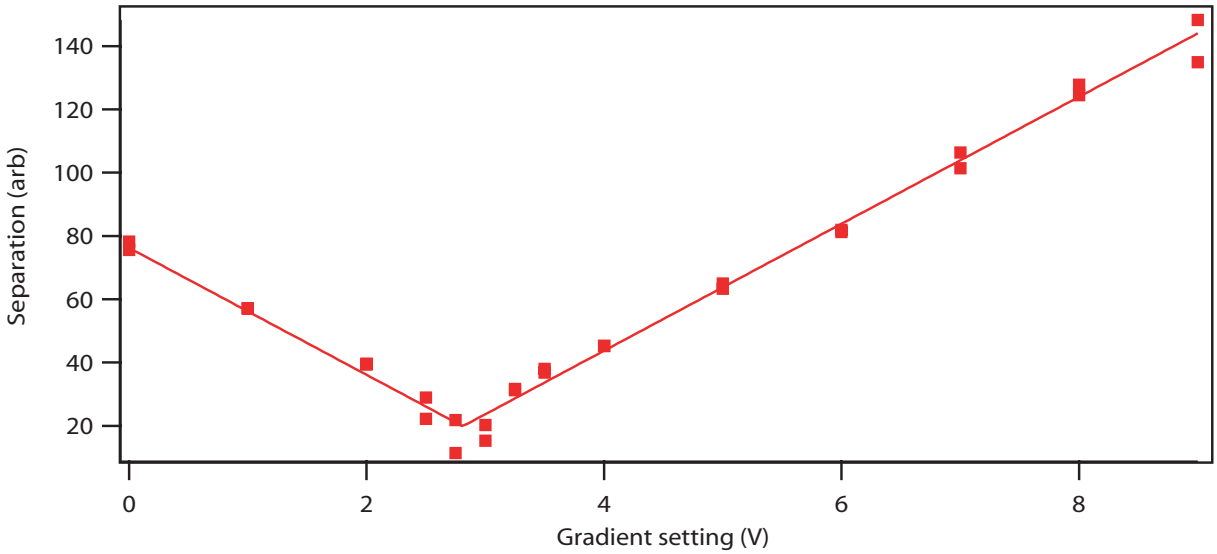

Figure 3-5: Stern-Gerlach calibration. Atoms in the $|2,-2>$ and $|1,-1>$ states are dropped in time of flight in varying magnetic fields. The x axis is voltage of the control apparatus, and is proportional to the magnetic field gradient. These data can be fit to an absolute value function to extract the strength of the gradient in G/cm/V. These data fit to a gradient strength of approximately 0.336 G/cm/V. The vertical offset from zero is due to the finite trap size.

they do. This same measurement gives us the gradient strength, as the separation of the atoms for a given time of flight should be proportional to the strength of the gradient. Figure 3.5 shows a plot of such a set of measurements; the separation of the atoms is an absolute value function because we do not differentiate between species in this measurement.

The most important measurment, however, is the location of the magnetic field zero. This value can be estimated from a Stern-Gerlach experiment, but for our purposes we need to be much more precise in our zero determination, at a level of about 1 mG/cm. To achieve this level of precision, we make an in-trap measurement of the atoms. After gradient evaporation, the two atom species will be on opposite sides of the trap. If the gradient is then lowered, the atoms will remain on opposite sides until the gradient passes through zero and reverses, whereupon the atoms will switch

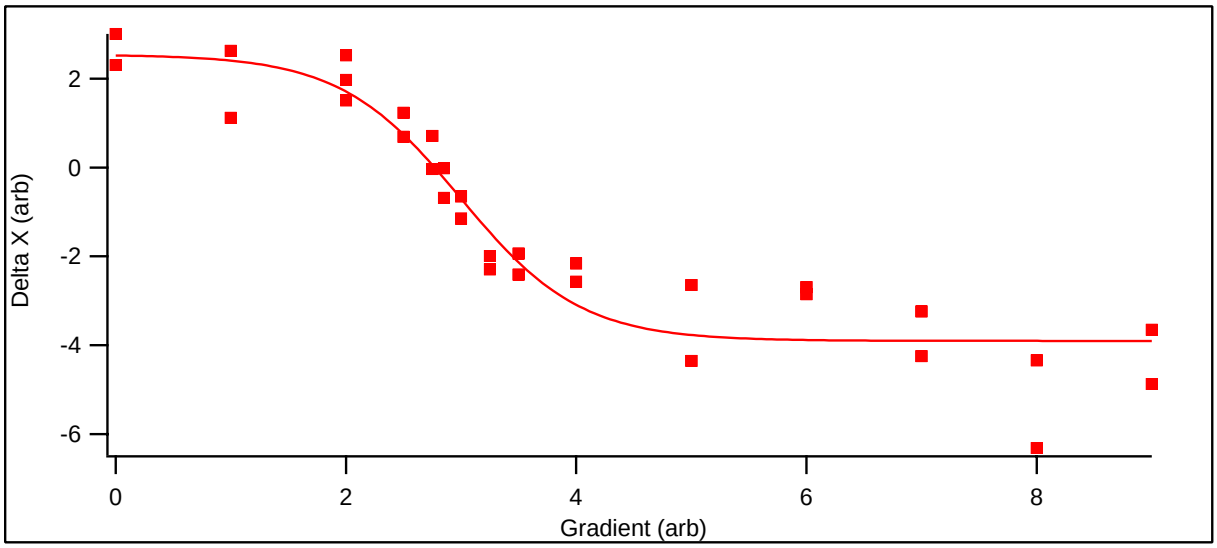

Figure 3-6: Magnetic field gradient zero measurement. Atoms in the $|2,-2>$ and $|1,-1>$ states are evaporated in a strong magnetic field gradient. The gradient is then lowered to a new value, and the positions of the $|2,-2>$ atoms and the atom cloud as a whole are measured. The x axis is gradient in arbitrary units with an unknown offset, and the y axis is the difference in positions, also in arbitrary units. The fit curve is to guide the eye; the gradient zero value is where the position difference equals zero.

sides. To determine the zero point, we make a series of measurements comparing the center position of the $|2,-2>$ atoms to the center of the atoms as a whole. The zero is where the difference between the two goes to zero. Figure 3.5 shows an example of the data from such a calibration run. This procedure can measure the gradient zero position accurate to a few mG/cm. To achieve a precision of 1 mG/cm, the same procedure is used, but the gradient is lowered more rapidly, in a manner similar to the process of spin gradient demagnetization cooling described in chapter 5, and the atoms are imaged in the presence of the lattice. This produces much colder atoms, which have a correspondingly higher sensitivity to the gradient zero.

Chapter 4

Spin Gradient Thermometry for Ultracold Atoms in Optical Lattices

As atoms in optical lattices are increasingly used to simulate condensed matter systems, the temperature of those atoms becomes more and more important to know. New realms of physics open themselves up at ever decreasing temperatures. Mott insulator shells first form at temperatures $T \sim 0.2U$, and the layers between those shells become superfluid at $T \sim zJ$ where z is the coordination number. For two-component systems, magnetic ordering first arises at temperatures $T \sim J^2/U$. All of these temperatures are well below the condensation temperature T_c, and the lowest are difficult to achieve at all, even in the absence of a lattice. Before one can even think about achieving these temperatures, however, it is important to have a method to measure them. While methods exist to measure temperatures in this range in the superfluid state, the development of similarly effective methods that can be applied in the Mott insulator has proven more difficult [16, 29, 38, 51, 56]. The spin gradient thermometry method described in this chapter provides such a method applicable in

a two-component system. These experimental results have reported in [74], a reprint of which is included in Appendix A.

4.1 Model of Spin Gradient Thermometry

Spin gradient thermometry admits a very simple theoretical treatment. The system involved consists of a collection of ^{87}Rb atoms in two different hyperfine states, $|2,-2>$ and $|1,-1>$. These atoms are put in the presence of a three-dimensional cubic optical lattice made from light at 1064 nm. The lattice is typically raised to a depth of $15E_{rec}$, putting the system above the Mott insulator transition. Finally, the atoms are subjected to a magnetic field gradient. Since the two atoms have different magnetic moments, they are pulled in different directions by the gradient: the $|2,-2>$ atoms are pulled towards the region of higher field while the $|1,-1>$ atoms are pulled towards the region of lower field. The ground state of the system, assuming a gradient high enough that we can neglect superexchange interactions, is for the particles to be completely segregated on opposite ends of the trap. Conversely, at high temperatures and low gradients, we should see a completely random mixture, with each particle equally likely to be on either side of the trap. The behavior of particles in between these two extreme cases is what we must understand.

Assume we have a lattice with total occupation number $n = 1$, composed of an equal mix of $|2,-2>$ and $|1,-1>$ atoms. The magnetic moments of the $|2,-2>$ and $|1,-1>$ atoms are $-\mu_B$ and $\mu_B/2$, respectively for a difference of $\Delta\mu = 3\mu_B/2$. First, we can treat the force on these atoms due to a magnetic field gradient as a constant force on both plus a symmetric force separating two particles of pseudospin $+1$ and -1, with effective magnetic moments of $\Delta\mu/2$. The constant force will just shift the trap, so it can be neglected, leaving only the symmetric force. Then, as long as we are in a regime where spin coherence effects are negligible, we can treat

each lattice site as being isolated, with a partition function factorizable as $Z = Z_\sigma Z_0$. Here, Z_0 is the partition function corresponding to the atom number n_i, and Z_σ is the partition function for the spin. The latter is then given by

$$Z_\sigma = \cosh(\frac{\beta}{2}\mathbf{\Delta}\mu\cdot\mathbf{B}(\mathbf{x})) \tag{4.1}$$

for magnetic field $\mathbf{B}(\mathbf{x})$ and $\beta = 1/k_B T$.

This expression is generally valid when the occupation number $n_i = 1$, while for occupation numbers other than 1, there are two correction factors. One is due to a difference in scattering lengths, and is proportional to $\Delta U = U_{12} - \frac{U_{11}+U_{22}}{2}$. This difference, due to different scattering lengths, is very small for ^{87}Rb and can generally be neglected. The other correction is due to the indistinguishibility of the particles, and acts as a multiplier on the temperature, usually less than a factor of two unless atom numbers are very large. The experimental data presented in this chapter ignore these corrections and treat atoms as being in the $n = 1$ case, while section 4.5 examines the corrections more closely and quantifies their size.

Setting these corrections aside, however, we can use this partition function to easily find the expected spin. Using the formula $< E >= -\frac{\partial \ln Z}{\partial \beta}$ to get the energy at a site, we then divide by $\mathbf{\Delta}\mu\cdot\mathbf{B}(\mathbf{x})/2$, half the energy difference between the spin up and down states. We can then write $< s >$ as a function of position:

$$< s(x) >= \tanh(-\frac{\beta}{2}\mathbf{\Delta}\mu\cdot\mathbf{B}(\mathbf{x})) \tag{4.2}$$

By measuring the actual spin distribution in a known magnetic field and fitting it to the above equation, one can then extract the temperature. Roughly speaking, as the temperature rises, the area near the boundary between the two spin regions changes from a sharp step to a gradual slope. The width of this boundary region is proportional to the temperature, and inversely proportional to the gradient of the

magnetic field.

Because the magnetic moment of the atoms will always follow the direction of the magnetic field, only the magnitude of the field is physically relevant. So we can write the field term as a constant field plus a gradient $B' = \frac{\partial |B|}{\partial x}$, in the form $\mu \cdot \mathbf{B}(\mathbf{x}) = \mu B'(x - x_0)$. The actual value of the constant magnetic field term is irrelevant to the physics of the problem: the position offset x_0 actually acts as a fit parameter to determine the ratio of spin up to spin down. If x_0 is in the center of the cloud, for example, then the spin ratio is $1 : 1$.

4.2 Experimental Procedure

A mixture of ^{87}Rb atoms in the $|2, -2>$ and $|1, -1>$ states is prepared in the presence of a magnetic field gradient as described in section 3-2. Initially, the strength of the magnetic field gradient is 2 G/cm, and in the same direction as the weakest axis of the trap. This gradient is always kept in the same direction, but its magnitude can be changed to any of a variety of other values. In equation 4.2, the argument of the tanh function is proportional to the magnetic field gradient, while inversely proportional to the temperature. Thus, applying a lower field gradient makes this thermometry technique sensitive to lower temperatures.

After lowering the gradient to the desired value, a three dimensional optical lattice is raised, typically to a depth of $15E_{rec}$. Since this depth is past the Mott insulator transition for ^{87}Rb, which occurs at $13.5E_{rec}$, the spin distribution should be decoupled from the particle-hole distribution, meaning equation 4.2 is a good approximation of the spin distribution. This distribution can then be measured and fit to extract the temperature.

The measurement of the spin distribution is done via a pair of absorption images. Although it is possible to extract the spin distribution from just a single image, using

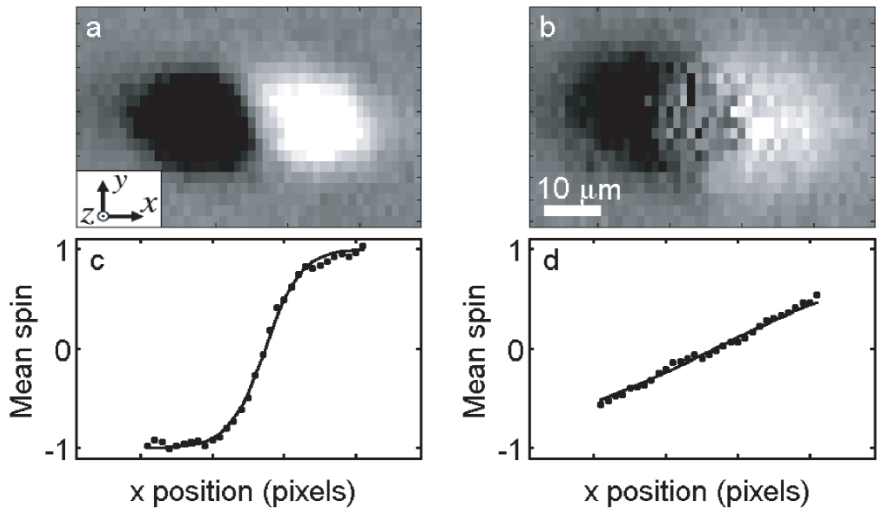

Figure 4-1: Images used for spin gradient thermometry. Data on the left were taken at a lower optical trap power than data on the right. Panels **a** and **b** are images of the spin distribution. Panels **c** and **d** show the mean spin versus x position. The fit to **c** gives a temperature of 52 nK; the fit to **d** gives a temperature of 296 nK. The inset of **a** shows the axes referred to in the text. The bar in **b**) is a size scale.

two images simplifies the fitting procedure and guards against systematic errors. On two consecutive runs, an absorption image is taken: the first run images the atoms in the $|2,-2>$ state, while in the second run the $|1,-1>$ atoms are optically pumped into the $F=2$ manifold, and then an image of all the atoms is taken. The difference between twice the first image and the second image shows the mean spin times the column density of atoms at each pixel, so the difference divided by the image of all atoms shows the mean spin as a function of x and y. Since the mean spin should only depend on x (the direction parallel to the gradient), integrating over the y axis gives a simple curve $< s(x) >$, which can then be fit to a hyperbolic tangent to extract the temperature. Figure 4.1 shows a pair of composite images at two different temperatures, along with the mean spin $< s(x) >$.

If the density of $|2,-2>$ atoms is $\rho_2(x)$ and the density of all atoms is $\rho(x)$, then

the fitting function used is

$$2\rho_2(x) - \rho(x) = \rho(x)\tanh[\frac{3}{4}\mu_B\frac{B'}{k_BT}(x - x_0)]. \tag{4.3}$$

The only free parameters used to fit are the position offset x_0, which measures the spin ratio, a vertical offset to cancel imaging errors, and the temperature, T.

4.3 Experimental Results

Figure 4.2 shows the results of this thermometry performed on ^{87}Rb atoms at two different temperatures, each at a variety of magnetic field values. As predicted by equation 4.2, the inverse width of the spin distribution is proportional to the strength of the magnetic field gradient for each constant temperature curve. However, the low temperature curve disagrees with this prediction for high gradients. This is a result of finite optical resolution of our apparatus–the real width is too small to resolve at high gradients and low temperatures. This effect was approximated by applying a 4 μm Gaussian blur to the predicted curve, shown as a dash-dotted line. This curve agrees with both the low and high gradient measurements. As a rule, however, this effect will limit our ability to resolve temperatures using an arbitrary gradient: to measure colder temperatures, it is necessary to lower the gradient to such a point that the width is no longer less than our optical resolution. If one leaves the gradient too high, the result is to overestimate the temperature.

In order to gauge the accuracy of spin gradient thermometry, it is necessary to compare it to other thermometric techniques. While there currently exist no other techniques capable of precisely extracting temperatures of atoms in optical lattices at the coldest ranges measured in our experiments, there do exist other reliable methods at higher temperatures. Figure 4.3 shows a comparison of one such technique to spin gradient thermometry. The other method estimates the temperature by a comparison

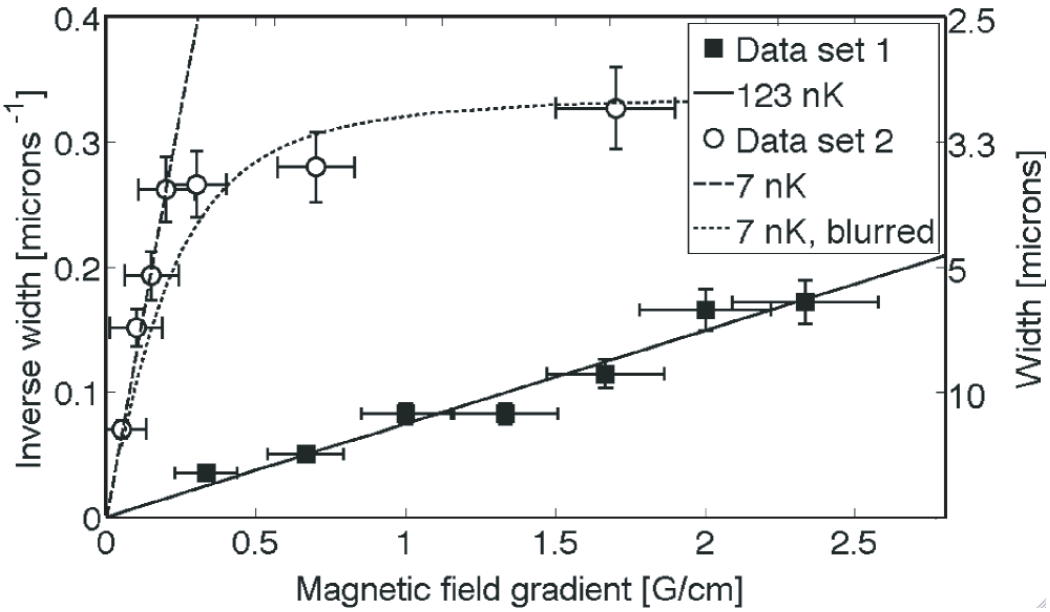

Figure 4-2: Independence of temperature on gradient. The inverse of the width of the spin profile is plotted as a function of magnetic field gradient for two data sets at two different temperatures. For constant temperature, a linear curve is expected. The width is defined as the distance from the center to the position where the mean spin is 1/2. The solid (dashed) line assumes a temperature of 123 nK (7 nK) and perfect imaging. The measured width of the colder data set saturates at high gradient because of finite imaging resolution. The dotted line assumes a temperature of 7 nK and an imaging resolution of 4 μm.

to the width of the cloud in the lattice, using the relation $\sigma^2 = k_B T/m\omega^2$, where σ is the $1/e^2$ half-width of the cloud along one axis and ω is the trap frequency along that same axis [51]. The x-axis is the strength of the optical dipole trap in arbitrary units. Because the depth of the optical dipole trap determines the rate of evaporative cooling, higher trap depths should correspond to higher temperatures.

The width is extracted from the wings of the atomic cloud, and the simple relation to the temperature depends on the approximation that the atoms are noninteracting. For high temperatures, this is a reasonable approximation as there will be many empty sites in the lattice, so atom-atom interactions are less important. However, as temperatures fall and the atoms become more closely packed, the atomic cloud becomes incompressible and this approximation breaks down. Figure 4.3 agrees with this expectation: at high temperatures, the two techniques give similar results, while at low temperatures width thermometry gives consistently higher estimated temperatures than spin gradient thermometry. The good agreement between these thermometry techniques lends credence to the claim that spin gradient thermometry also produces accurate results in temperature ranges where no other technique can currently be used.

4.4 Limits and Comparison to Other Techniques

One of the most useful aspects of spin gradient thermometry is its wide range of applicability. As the data in Figure 4.3 indicate, spin gradient thermometry can provide accurate temperature values at high temperatures, even those higher then the critical temperature for Bose condensation. Moreover, this same technique can be used to measure ever lower temperatures by setting the magnetic field gradient to lower values. The lowest temperature we measured in the lattice using ordinary evaporative cooling techniques was approximately 1 nK, but even this temperature is by no means

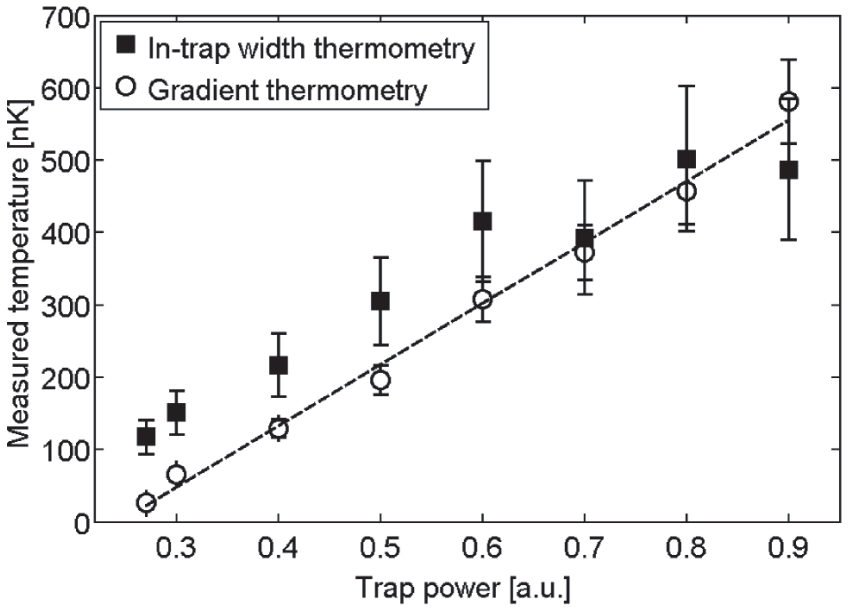

Figure 4-3: Validation of spin gradient thermometry. Comparison of two measured temperatures versus final power in one of the optical trapping beams. Squares represent the results of in-trap cloud width thermometry, and circles represent the results of spin gradient thermometry. Error bars represent estimated uncertainties. The dashed line is a linear fit to the spin gradient thermometry data. The closeness of this fit suggests that the temperature reached is proportional to the trap depth.

the lower limit of the resolution of this thermometry technique. The ultimate lower temperature limit of spin gradient thermometry arises from a comparison of the optical resolution available and the precision of control over magnetic field gradient. For our apparatus, for example, control over the gradient on the order of 1 mG/cm will give a lower limit of approximately 50 pK. Of course, depending on the lattice depth and atom-atom interactions, superexchange ordering may arise, in which case that will instead determine the lower limit. In chapter 5, we will see how a new cooling technique developed in this lab has measured spin temperatures down to this limit.

To further shed light on the utility of this technique, in is helpful to compare spin gradient thermometry to other thermometric techniques available for use, both in and out of the lattice. Because temperatures measured in the condensate do not always correspond to temperatures in the lattice, it is most helpful to compare the range

of entropies per particle, S/Nk_B, in which a thermometer can function. Condensate fraction thermometry, for example, has difficulty measuring condensate fractions below 10%, and as a result its effective range is from $.35 < S/Nk_B < 3.5$. The cloud size thermometry discussed above and used in figure 4.3 has a similar lower limit, although its upper limit is unbounded. Theromometry based on interference peak visibility is computationally intensive, requiring advanced Quantum Monte Carlo calculations, but has been used to measure temperatures as low as $0.08U$ [70]. However, this technique is not applicable in the deep Mott insulator [56]. Measurement of the width of the conducting layers between Mott shells is the only other technique that can be used in the Mott regime [27, 29, 35], but the range is narrow: $0.4 < S/Nk_B < \ln(2)$. Here the upper limit is the entropy at which the Mott shells melt, while the lower limit is determined depends on the optical resolution and trap shape, but will not vary too much from this estimated value for typical experiments.

By way of comparison, spin gradient thermometry is applicable in the range $0.1 < S_\sigma/Nk_B < \ln(2)$, where S_σ is the total *spin* entropy. By adjusting the strength of the magnetic field gradient, entropy can be freely shifted between spin and particle-hole degrees of freedom to keep S_σ/Nk_B within this range. In essence, spin gradient thermometry measures the penetration of a boundary region similar to Mott shell width thermometry. However, whereas Mott shell width thermometry's boundary is of a strength fixed by the lattice geometry, spin gradient thermometry involves a boundary whose strength can be freely tuned by changing the gradient. This is related to the fact that the energy of lowest energy excitations of the Mott insulator is determined by U, as shown earlier in figure 2.3, which is intimately tied to the lattice depth and not easy to change. For temperatures much less than U, this freezes out excitations everywhere but the narrow superfluid shells, making resolution of the temperature very difficult. By comparison, the lowest energy excitations in spin gradient thermometry are given by $B'\Delta\mu\Delta x$, where Δx is the distance between

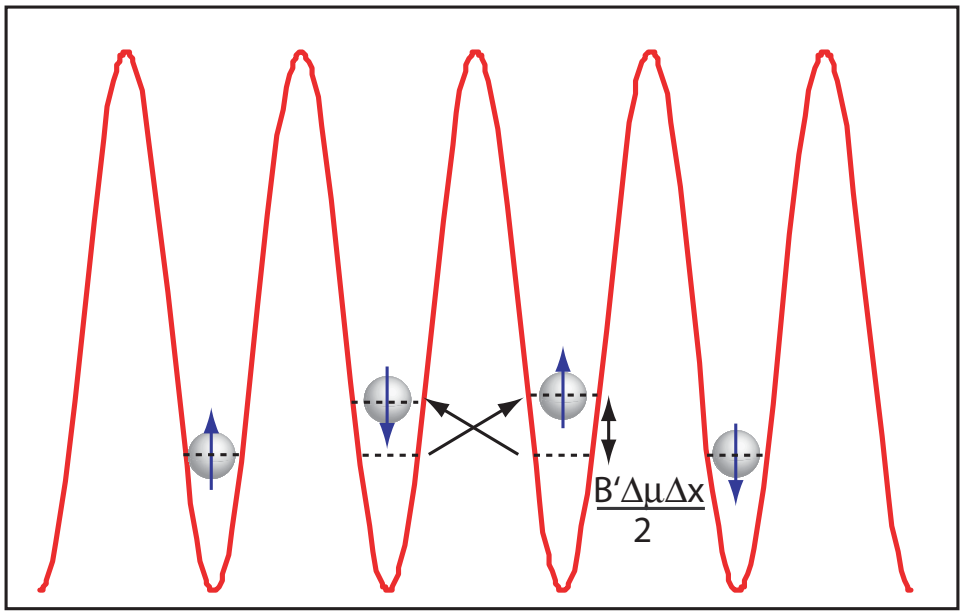

Figure 4-4: Excitations in spin gradient thermometry. In contrast to the Mott insulator, which has a fixed energy U as its lowest excitation, spin gradient thermometry introduces an excitation of tunable strength. The lowest energy excitation is a spin exchange over a distance Δx between adjacent lattice sites, and has total energy $B'\Delta\mu\Delta x$, or $B'\Delta\mu\Delta x/2$ per particle. In this graph, the gradient is oriented to push spin up particles to the left, and the ground state energy for each site, including the energy due to the magnetic field gradient, has been set to zero.

lattice sites. These excitations are shown in figure 4.4. Because B' is a freely settable parameter, one can make these excitations as large or small as needed in order to resolve them.

Furthermore, because of the decoupling between the spin and particle-hole degrees of freedom, the bulk porperties of the Mott insulator are not significantly changed by the existence of a second spin component or the gradient. Rather, they behave as an extra thermometer attached to the cloud as a whole. It is only in the regime of superexchange-driven magnetic ordering, when even spin gradient thermometry breaks down, that the presence of a gradient and a second component begin to modify the bulk properties of the system.

4.5 Effects of Occupation Number $n_i > 1$

The technique of spin gradient thermometry is most easily applicable in a lattice with occupation $n = 1$ at all sites. At higher densities, where $n_i > 1$, there are two corrections for spin gradient thermometry, one to the partition function as a whole, due to the indistinguishibility of the bosons, and one to the potential as a result of unequal interaction strength between species. This section will quantify these two effects, the first of which takes the form of a multiplier to temperature, and the second of which acts approximately as an added term.

4.5.1 The Effect of Indistinguishability

The partition function Z_σ described in section 4.1 is valid for sites with $n = 1$ filling, and also for distinguishable particles at any occupation number. It is not, however, valid for indistinguishable bosons with $n > 1$. This is because the degeneracy of the different levels is miscounted. For example, in the case of $n = 3$, there are four possible total spin values for the site: 3, 1, -1, and -3. In the classical (indistinguishable) case, these values have degeneracy 1, 3, 3, 1, and these degeneracies are reflected in the simple model where $Z_3 = Z_1^3$. This partition function would imply that the spin per particle for an $n = 3$ site is the same for an $n = 1$ site. However the same spin levels in the indestinguishable case all have degeneracies of 1. Thus, $Z_3 \neq Z_1^3$. Instead, we can write the general n particle partition function as $Z_n = \sum_{j=-n/2}^{n/2} \exp(-\frac{\beta}{2}\mathbf{\Delta}\mu \cdot \mathbf{B}(\mathbf{x}) \cdot 2n)$, or in a simpler form,

$$Z_n = \frac{\sinh[(n+1)\beta/2\mathbf{\Delta}\mu \cdot \mathbf{B}(\mathbf{x})]}{\sinh(\frac{\beta}{2}\mathbf{\Delta}\mu \cdot \mathbf{B}(\mathbf{x}))}. \tag{4.4}$$

This partition function can then be used to predict the mean spin per particle at a site. This value is easily calculated as

$$< s >= \frac{n+1}{n}\coth[(n+1)\frac{\beta}{2}\Delta\mu B'x] - 1/n\coth(\frac{\beta}{2}\Delta\mu B'x). \tag{4.5}$$

It can easily be checked that this simplifies to equation 4.1 in the $n = 1$ case, but for $n \neq 1$ the form of the equation is not so easy to work with. It is especially not simple to fit to when, as is common in experiments with higher filling factors, one must integrate over a range of sites with different values of n. Nonetheless, with a good knowledge of how many atoms are in each given n state, a good approximation can be made. As n increases, the spin function changes from a hyperbolic tangent to a similar function with a steeper slope. This makes it appear as though the temperature has decreased. Thus, a site with n particles will look like it is a n=1 site, but with temperature of approximately

$$T_{apparent} = \frac{3}{n+2} T_{real}. \tag{4.6}$$

So, by fitting the temperature as though it the lattice were at $n = 1$ filling, then multiplying by $\frac{n+2}{3}$, we get an approximately correct temperature. If we are integrating over a range of values for n, the correction to the temperature can then be approximated as

$$T_{real} = (\sum_n f_n \frac{n+2}{3}) T_{apparent} \tag{4.7}$$

where f_n is the fraction of atoms in sites with occupation number $n_i = n$. The correction to the temperature caused by this is independent of the temperature itself, and is a relatively small multiplier: for a lattice of pure $n = 2$ sites, for exemple, the temperature appears 25 percent colder than it really is. Because sites with three atoms or more decay rapidly through 3-body recombination [12], most experiments will not have many lattice sites with three or more atoms, especially when trying to achieve lower temperatures.

Property	Symbol	Value
$\|1,-1>$ s-wave scattering length	a_{11}	$100.44a_0$
$\|1,-1>/\|2,-2>$ s-wave scattering length	a_{12}	$98.09a_0$
$\|2,-2>$ s-wave scattering length	a_{22}	$95.47a_0$

Table 4.1: ^{87}Rb scattering lengths. Values are taken from [34]. The uncertainties of these values are not given, but a measurement of $a_{22} - a_{11}$ in the same reference has uncertainty $0.31a_0$.

4.5.2 Scattering Length Correction

In addition to the above correction to the partition function, there is also a correction to the potential the atoms feel in sites where $n_i > 1$. This arises when the interaction energy U depends on spin. Although atoms in both states experience the same lattice potential in our experiment due to our lattice's large detuning, there is a slight difference in their interaction energies due to the states' different scattering lengths. In ^{87}Rb, the scattering lengths of atoms in the $F = 2$ and $F = 1$ manifolds are nearly identical, there is nevertheless a small difference: the best known values [34, 73] are given in terms of the bohr radius a_0 in table 4.1. While the variation between the values a_{11}, a_{12}, and a_{22} is small on its own, ranging over only a few percent in value, it is actually the much smaller difference $\Delta a = a_{12} - \frac{a_{11}+a_{22}}{2} = 0.135a_0$, that matters. To see why, imagine two sites, separated by distance Δx, one with n atoms in the $|2,-2>$ state and one with the same number in the $|1,-1>$ state. The energy cost per particle of switching one of the atoms from one well with one from the other would normally be $\Delta\mu B'\Delta x/2$. However, the interaction energy difference adds an additional cost equal to $(n-1)\Delta U$ where $\Delta U = U_{12} - \frac{U_{11}+U_{22}}{2}$, the difference between the interspecies interaction energy and the mean of the two intraspecies interaction energies. Since $U_{ij} \propto a_{ij}$, we can write $\Delta U \approx U\Delta a/a$, which in a $15E_{rec}$ lattice is about $k_B \cdot 40$ pK. This should be treated as a rough value, as the scattering lengths of ^{87}Rb very nearly cancel, so this remainder is similar in size to the precision of measurement.

Clearly, this energy scale is much smaller than any of the temperatures measured above, but in chapter 5, temperatures are reached that are sufficiently low that this correction becomes significant—comparable in size to the partition function correction. Thus, it is worth writing out the full form of the correction to the potential now. It can be written in a self-consistent manner as a function of the spin distribution $s(x)$ in the following manner:

$$E(x) = \frac{\Delta\mu}{2} B' x + s(x)(n-1)\Delta U \tag{4.8}$$

Because ΔU is positive, meaning these two states are naturally immiscible, the effect is to make the sample appear colder than it really is. Of course, given the size of the error bars on ΔU compared to its size, it is even possible that the sign of the effect is opposite, favoring a mixture of spins rather than a segregation at zero temperature. Nonetheless, the best estimate is that a small positive correction term must be added to temperatures when they drop below 100 pK or so.

4.6 Dependence of Temperature on Gradient

As a final point of consideration, on careful examination of figure 4.2, one question that may arise in the reader's mind is this: Why do the data points in a given set all fit to the same temperature? At first glance, the answer may appear obvious: each shot was prepared in the same manner, with the same trap depth and lattice depth, so of course they should be the same temperature. However, this is not quite true. One thing that does vary between the shots is the final strength of the gradient. While each shot is prepared by evaporatively cooling the two components in a gradient of 2 G/cm, that gradient is changed to the various values on the x-axis before turning on the lattice. Might this changing gradient not affect the temperature? After all, section 4.4 describes how changing the gradient moves entropy between spin entropy

and bulk entropy, so it is natural to question whether this transfer of entropy would heat or cool the system. Indeed, one would expect that if the gradient is lowered, more entropy would go into spin, leaving less in the bulk and thus cooling the system as a whole. Since we do not see this in the data in figure 4.2, we must explain why. That is, why is the process of lowering the gradient isothermal in our experiment rather than, say, adiabatic?

The answer to this question lies in the exact manner in which the gradient was lowered. In each experimental run, the gradient was lowered from 2 G/cm to its final value over a very long time: the gradient was changed linearly over the course of $400ms$. Then, the atoms were held an additional $400ms$ before ramping up the lattice over the course of about $150ms$. Thus, the atoms had nearly a second to spend "adjusting" to the new lattice depth. The reason this kept the system at its initial temperature is the same reason it was at that temperature to begin with: the balance between heating and evaporative cooling. The trap depth determines the temperature of the atoms by determining the rate of evaporative cooling. As the atoms cool, the rate of evaporation drops. But this evaporative cooling is balanced by heating due to three body losses, collisions with background gas particles, and other mechanisms. The final temperature is the point at which this heating and the evaporative cooling rate balance. If the atoms are suddenly cooled when the gradient changes, the rate of evaporative cooling will drop, and on net, the system will begin to heat up. Given enough time, this heating will continue until the atoms are back to their initial temperature. Thus, a very slow change in gradient, such as was done in our experiment, will be approximately isothermal.

But what about a more rapid change. one that did not allow time for heating from collisions and other mechanisms to warm the atoms back up? Naturally, the expectation is that we really would see cooling as entropy was shifted between spin and bulk excitations. A fast enough ramp time could be almost perfectly adiabatic,

allowing for a maximum cooling effect. And indeed, it is precisely this phenomenon, analogous to the condensed matter technique of adiabatic demagnetization refrigeration, that is used in the experiments of chapter 5 to achieve temperatures well into the picoKelivn range. Also in that chapter, data will be presented that explicitly check this transition between isothermal and adiabatic changes in gradient.

4.7 Conclusion

Spin gradient thermometry represents an important new technique for measuring the temperature of ultracold atoms in optical lattices. We have demonstrated its wide dynamic range, and its compatibility with other techniques within their own dynamic ranges. It is well suited for measuring lattice temperatures for two-component systems, making it a valuable tool for use in quantum simulation of magnetically-ordered systems. The limitations of this technique are very few, arising only at especially high densities or at very low temperatures, as superexchange physics begins to play a role. With future experiments, such as those described in the next chapter, it is hoped that these limits will be put to the test, leading to a new frontier in atomic physics.

Chapter 5

Spin Gradient Demagnetization Cooling

Spin gradient thermometry provides the ability to measure very cold temperatures in the presence of an optical lattice, but it does not, on its own, provide a means to achieve them. For ^{87}Rb, magnetically ordered states in the Mott insulator are expected to arise at temperatures around $100 - 200$ pK [21], which is significantly below the temperatures usually accesible in ultracold atoms, even outside of a lattice. However, the same physics that allows spin gradient thermometry to measure the temperature of a two-component system can be harnessed to cool that same system. By changing the strength of the gradient separating the two spin components, it is possible to substantially cool the system. This process, which we call spin gradient demagnetization cooling, is analogous to the condensed matter process of adiabatic demagnetization refrigeration. By using a time-varying magnetic field gradient to change the spin energy scale, it is possible either to cool the spins as an isolated system, or to pump entropy into the spin degrees of freedom, thereby cooling the system as a whole. Using this technique, we have prepared states with spin temperatures of 75 pK and -75 pK. We have also produced bulk temperatures in an apparent

equilibrium at 300 pK, although we cannot rule out long-lived metastable excitations that may fail to couple to our thermometer. These temperatures represent the lowest temperatures which have been achieved in any system [33, 46, 71]. The experimental results described in this chapter were reported in [5] and is included in Appendix B.

5.1 Basic Theory

To understand the basic theory of this cooling technique we need only look at the theory behind spin gradient thermometry. In the presence of a magnetic field gradient, a two-component Mott insulator will separate into to regions of opposite spin, with a boundary region of mixed spin in the center. The width of this region will be proportional to the temperature of the spins and inversely proportional to the strength of the magnetic field gradient. If the strength of the magnetic field gradient changes, then one or both of the other two properties—the temperature or the width—must change to maintain this equality. The way these two change depends on the manner in which the gradient is changed, so it is useful to look at two different models to explain it. The first will be most useful if the gradient is changed nonadiabatically and the spin system is held out of equilibrium with the particle-hole degrees of freedom, while the second covers the case where it is changed adiabatically and in thermal contact with the particle-hole degrees of freedom.

5.1.1 Direct Cooling for Nonadiabatic Demagnetization

In the first, simplest case, we treat the nonadiabatic case in which the spin degree of freedom is isolated from the particle-hole degrees of freedom. This case can be accomplished experimentally by placing the atoms in a deep Mott insulator. In a Mott insulator, the rate of spin relaxation is proportional to J^2/U, a quantity which can become very small at high lattice depths. Then, if the strength of the gradient

is changed on a timescale much shorter than the spin relaxation time, we can treat the spin as an isolated system and ignore the particle-hole degrees of freedom (which remain at their original distribution and temperature).

Because the spin system is "frozen" in place, the width of the domain wall will not change, and the total spin entropy is conserved. In this case the temperature of the spin system will scale proportional to the strength of the magnetic field. To see why this is, recall the thermodynamic definition of temperature

$$T = \frac{\partial E(S)}{\partial S}|_{N,V}. \tag{5.1}$$

If $E(S)$ is simply scaled by a constant without changing the configuration of the system, then obviously T will be scaled by the same constant.

A good toy model to illustrate this effect is that of a system of spin-1/2 particles with magnetic moment μ in a uniform magnetic field of initial strength B_1. Figure 5.1 illustrates this system. The lower state has energy $-B_1\mu/2$ while the upper has energy of $B_1\mu/2$. If the population in the upper state is p, then one can easily work out from the Boltzmann distribution that the temperature is

$$T_1 = \frac{\mu B_1}{k_B \ln \frac{1-p}{p}}. \tag{5.2}$$

If the magnetic field is changed to B_2 while the magnetization is held fixed then the new temperature must be $T_2 = TB_2/B_1$. Furthermore, if the field is reversed in direction, then the temperature will be negative as a result, indicating that the swapping of the two energy states has led to an inverted population.

The toy model illustrated in figure 5.1 is actually a reasonable approximation of the spin physics behind the process of adiabatic demagnetization refrigeration used in condensed matter systems. However, the full process of adiabatic demagnetization refrigeration is more closely analogous to the adiabatic case, which is discussed in the

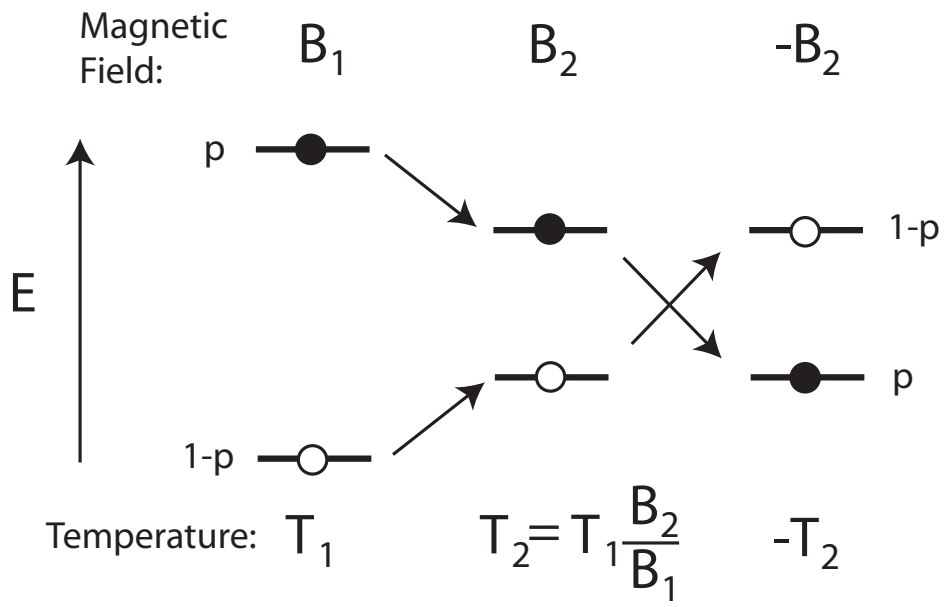

Figure 5-1: Demagnetization toy model. This model illustrates the physics behing the spin part of adiabatic demagnetization cooling. If the particles cooled by demagnetization are decoupled from other degrees of freedom, then their spin can be cooled in exactly this manner. In real atomic systems, the difficulty of controlling magnetic fields to the necessary μK level limits the practicality of using this simple scheme of demagnetization.

next subsection. Regardless, magnetic field demagnetization of this sort is impractical for use in atomic systems due to difficulties in magnetic field control [23]. However, a magnetic field gradient can be used to generate a similar effect in a much easier manner. As discussed in chapter 4, a two-component Mott insulator in the presence of magnetic field gradient will have a spin distribution given by

$$< s(x) >= \tanh(-\frac{\Delta\mu B' x}{2k_B T}). \tag{5.3}$$

Clearly, if the spin distribution is held fixed and the gradient B' is changed, the temperature must shift by the same factor. Magnetic field gradients are much easier to control than magnetic fields, so that cooling that would require an impractical μG magnetic field control can be achieved with gradient control at the relatively easy mG/cm level. Also, magnetic field gradients can easily be reversed in direction without inducing spin flips, allowing the straightforward production of negative temperature systems.

5.1.2 Adiabatic Demagnetization as an Entropy Pump

The nonadiabatic case described above is simple because the spin distribution is held fixed. As a result, it is only the spin temperature that is cooled—the particle-hole degrees of freedom are thermally isolated and remain at their starting temperature. This is fine if we only wish to cool the spin degree of freedom, but if we wish to cool the system as a whole, it becomes more complicated. As this process requires the system to equilibrate, it is best used as a model when the gradient is changed in a shallow lattice, or none at all, so the system remains in equilibrium throughout the demagnetization process. If this condition holds, we can model the process as adiabatic.

In contrast to the nonadiabatic case, this process will be almost directly analogous

to adiabatic demagnetization refrigeration [20, 31]. In adiabatic demagnetization refrigeration, a paramagnetic material is prepared in a strong magnetic field. The magnetic field strength is then decreased, and entropy is absorbed into spin-flip excitations, cooling the system. In our system, the total magnetization is conserved, so there are no spin flips; however, the same role is played by spin exchanges across the boundary region of randomly oriented spins in the center of the system. This will allow the elimination of particle-hole excitations in favor of spin-exchange excitations.

In adiabatic spin gradient demagnetization, the gradient is lowered, causing the energy scale of the spin degrees of freedom to fall while the energy of the particle-hole degrees of freedom remain fixed. But since these two parts of the system are now in thermal contact, entropy will flow out of particle-hole excitations to create spin exctations. As a result, the width of the central "domain wall" of random spin will widen. However, it will not widen proportionally to the change in magnetic field: since entropy is leaving the particle-hole excitations, they are cooled, and therefore the entire system must be colder. Roughly speaking, if the gradient changes from B_1' to B_2', then the final temperature will be

$$T_2 = \frac{B_2'}{B_1'} \frac{S_0 + \Delta S}{S_0} T_1 \tag{5.4}$$

where S_0 is the initial spin entropy and ΔS is the entropy absorbed by the spins. The size of ΔS will depend on the relative heat capacities of the spins and the rest of the system, which will depend on various factors including the density of atoms and the lattice depth. In a sense, the spins are used as a "sponge" to soak up the entropy in the rest of the system. In the end, at very low gradients, nearly all the entropy can be transferred into the spins, and the final temperature of the system will be much colder. Indeed, if the starting entropy is low enough (below about $k_B \ln 2$ per lattice site), then in the limit as the gradient strength approaches zero, all of the entropy

could be absorbed into the domain wall.

This gives us a lower limit for the temperature that can be achieved by adiabatic spin gradient demagnetization. If the total starting entropy of the system is S_{total}, of which the spins initially contain S_{spin}, then applying equation 5.4 gives us an expression for the maximum cooling factor:

$$\frac{T_1}{T_2} = \frac{B_1'}{B_2'} \frac{S_{spin}}{S_{total}}. \tag{5.5}$$

For our experiment, the ratio of magnetic field gradients available is around 1000. If we have a starting temperature of about 5 nK, and about half the total entropy were initially in the spins, with half initially in the particle-hole degrees of freedom, this would suggest a lower limit of somewhere around 10 pK, assuming total transfer of entropy and no additional heating. This equation also applies for the nonequilibrium case, except that in that case, $\Delta S = 0$, so S_{spin}/S_{total} should be set to 1.

Another limit on the lowest achievable temperature stems from the effects of spin coherence, which will start to become important near the Curie temperature of the spin-ordered phases. Spin correlations reduce the heat capacity of the spin degrees of freedom, because a magnetic domain containing multiple sites can only hold as much entropy as a single site could in the absence of correlations. These practical and theoretical limits on spin gradient demagnetization cooling do not appear to preclude cooling below the Curie temperature of the spin-ordered phases. This technique thus provides a specific and realistic method of realizing magnetic phase transitions in lattice-trapped ultracold atoms.

5.2 Experimental Procedure

The initial state of the system is a two-component BEC at zero lattice depth in a strong gradient. The two components are the $|2, -2>$ and $|1, -1>$ hyperfine states

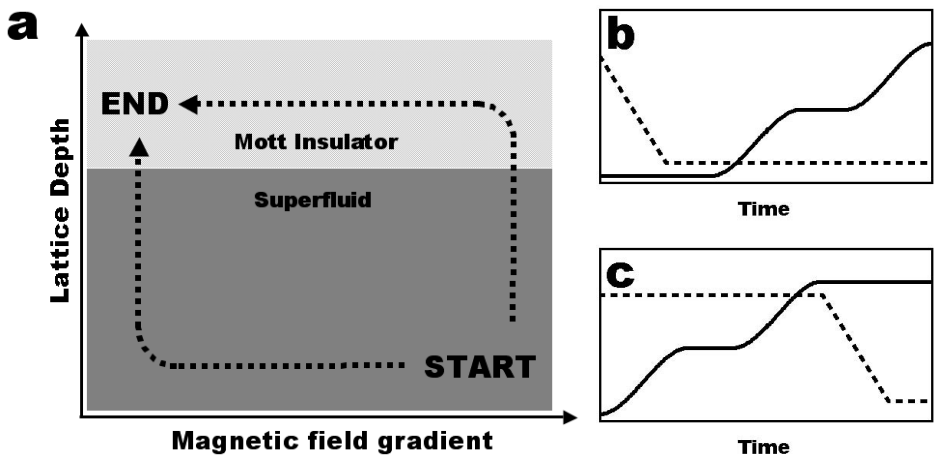

Figure 5-2: Details of two experimental cooling protocols. **a**: Experimental phase diagram of lattice depth vs. applied gradient. Dashed lines show two different paths along which one can move between the high-gradient superfluid state and the low-gradient Mott insulating state. **b**: Lattice depth (solid line) and gradient strength (dashed line) versus time for the lower path in panel **a**. **c**: Lattice depth (solid line) and gradient strength (dashed line) versus time for the upper path in panel **a**. The shape of the lattice rampup is designed to ensure maximum equilibration.

of ^{87}Rb, and the gradient strength is initially 2 G/cm. The final state will be one of high lattice depth, beyond the Mott insulator transition, and low gradient. The way this state is reached depends on what type of experiment is to be performed. The two experimental pathways used differ in which is done first: the lowering of the gradient or the raising of the lattice. Figure 5.2 depicts these two orderings as different paths in an experimental "phase space" of gradient vs lattice depth.

In the lower path, as shown in part b of figure 5.2, the gradient is first lowered with the lattice still at zero depth. Because this occurs in the superfluid, we can expect the change to be adiabatic so long as the rate of change of the gradient compares favorably to the trap frequency. The typical demagnetization time is $100ms$, which should be sufficiently slow when compared to the lowest trap frequency of $36Hz$. Next, the lattice is raised to a depth of $15E_{rec}$, which is above the Mott insulator transition point of $13.5E_{rec}$. The lattice is raised in three steps: a cubic spline to an intermediate

lattice depth (typically 6 or $7E_{rec}$), held for a brief time, then raised again in a cubic spline to its final depth. The process takes between 150 and $200ms$ in total. The reason for the intermediate hold is an attempt to maximize equilibration in the lattice. At higher lattice depths, tunneling slows down exponentially, while low lattice depths are sensitive to vibrational heating, so spending more time at intermediate depths helps ensure maximum equilibration without introducing too much extra heating.

This produces a system that has been cooled similar to the adiabatic case described in the theory section. Although the particle-hole and spin degrees of freedom may not be perfectly equilibrated—certainly they are frozen in at some point as the lattice crosses the Mott insulator transition—they are nevertheless in equilibrium to the greatest extent possible. As a result, the domain wall width will be widened significantly from its initial width, and will provide an estimate of the temperature of the system as a whole.

The upper path, on the other hand, is used to produce a nonequilibrium cooling of the spin degrees of freedom alone. This path is depicted in part c of figure 5.2. Here, the gradient is kept at a strength of 2 G/cm while the lattice is raised in the same, three-step manner as in the adiabatic case. At this point, the lattice is then held in the Mott insulating state, so the tunneling rate will very small, proportional to the superexchange term J^2/U, and the atoms can be treated as frozen in place. In this case, we can say that the particle-hole and spin degrees of freedom are isolated from each other, and will be essentially separate systems with fixed entropy and independent temperatures. The spin temperature can now be directly cooled by lowering the gradient. The gradient is lowered over the course of 100ms, which in this case is much faster than the tunneling rate, supporting the assertion that we are creating a spin temperature isolated from the rest of the system. Since the spins are isolated, they can even be brought to negative temperature distributions by reversing the direction of the gradient. These distributions should remain at a stable

temperature on timescales on the order of the superexchange time.

5.3 Experimental Results

Each of the two experimental procedures described above was performed over a variety of different values of final magnetic field gradient. The results of the nonadiabatic path are shown in figure 5.3. The simple nature of this experiment allows one to essentially set the temperature at whim by selecting a sufficiently low final field gradient value. For negative field gradients, this produces negative temperatures. The minimum temperature limit is ultimately set by one's optical resolution and ability to measure field gradient, so this procedure allowed the production of spin temperatures of 75 pK and -75 pK. Since the total energy is monotonic in $1/T$, these temperatures represent the most extreme (coldest and hottest) thermodynamic states ever measured in spin systems [33, 71]. Because these spin temperatures are well isolated from the bulk temperature, they display long lifetimes. The inset of figure 5.3 shows temperature versus hold time for both positive and negative spin distributions. If a negative temperature distribution is held for several seconds in the lattice, its temperature becomes more negative, as expected.

The results of the adiabatic path, on the other hand, are more difficult to model theoretically, and reach lower temperatures, but they are also more interesting in that they produce a system closer to true equilibrium. Figures 5.4 and 5.5 show the results of initial spin gradient demagnetization cooling experiments. As the field gradient is reduced, the width of the domain wall is observed to increase (see figure 5.4), indicating the transfer of entropy from the kinetic degrees of freedom to the spins. The width increases much less steeply than would be expected for an isothermal sample; this demonstrates cooling. The observed domain wall width can be converted to a temperature using spin gradient thermometry. The measured temperature falls

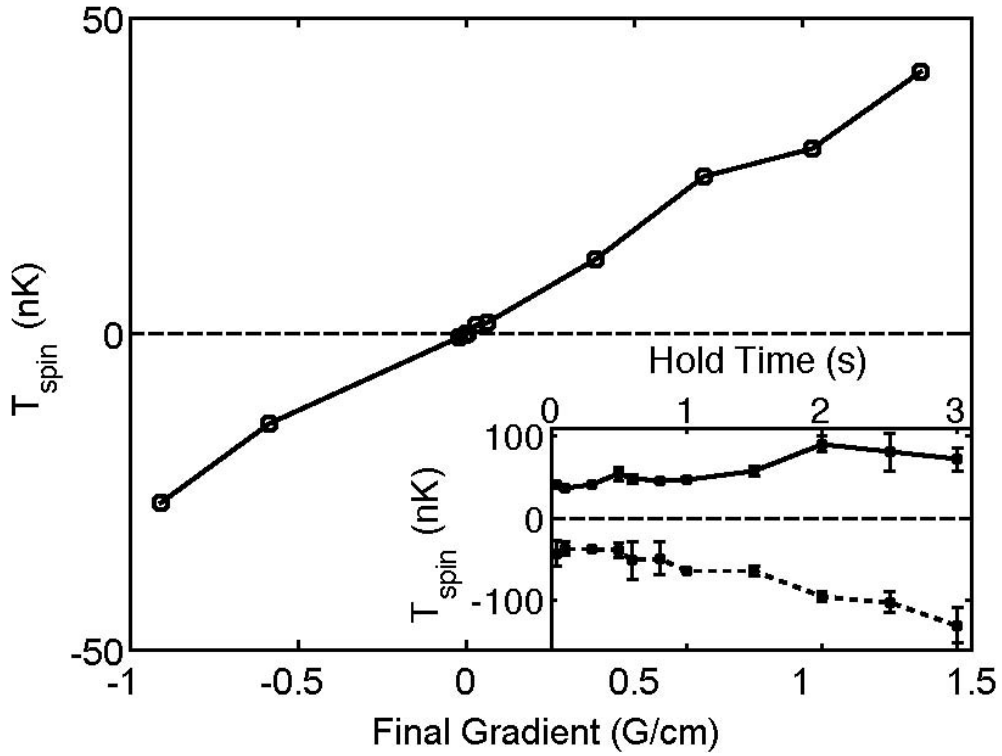

Figure 5-3: Preparation of arbitrary spin temperatures. **Main Plot**: measured spin temperature versus final gradient, for the case of rapid gradient change in the Mott insulating state. **Inset**: Temperature versus hold time in the lattice of spin distributions at negative (dashed line) and positive (solid line) initial temperature. Note that, as expected, the temperature of the negative distribution becomes more negative as it heats. Error bars represent the standard deviation of the data at each point.

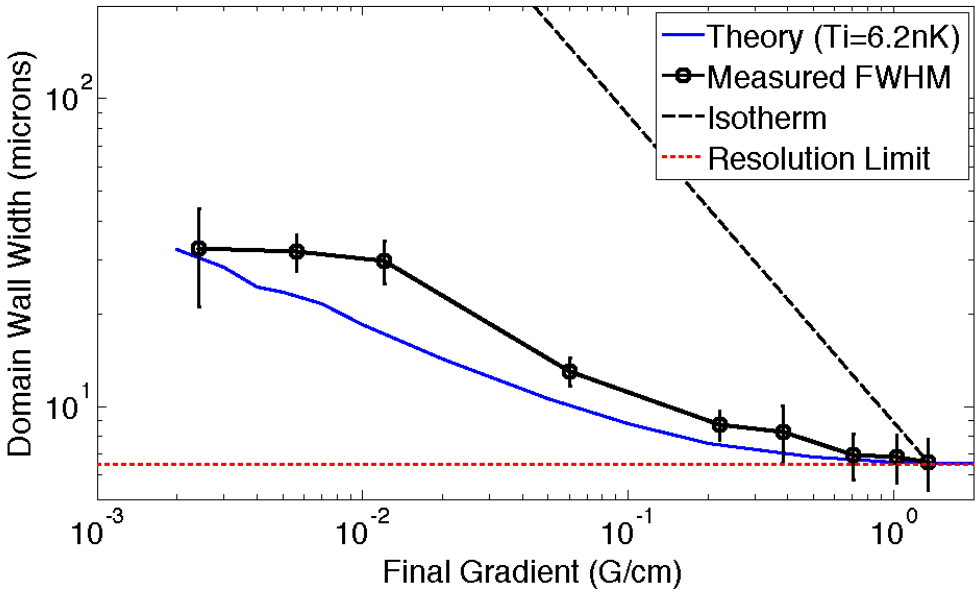

Figure 5-4: Plot of width vs. field gradient. Demonstration of spin gradient demagnetization cooling. Measured domain wall width vs. final magnetic field gradient, for the case of adiabatic gradient lowering in the superfluid state followed by lattice rampup. The dashed line is an isotherm, meaning that it represents the expected widening behavior assuming no cooling. The dotted line shows the minimum measurable width, given our optical resolution. The blue curve is the theoretical prediction, assuming adiabatic demagnetization from an initial temperature of 6.2 nK and including the effects of finite optical resolution.

rapidly as the gradient is lowered (see figure 5.5). The lowest measured temperature is on the order of 300 pK, which is within a factor of 2 of the expected Curie temperature of the XY ferromagnet [15]. Theoretical curves in the two figures show good agreement with the data and were fit with only one free parameter: the initial temperature prior to demagnetization.

5.4 Modelling the Adiabatic Case

Figures 5.4 and 5.5 include a theoretical fit to the cooling data, assuming an initial temperature of 6.2 nK, which is derived from a 1-paramater fit to the data. This section will explain the method used to model this case. The theory for the spin degrees

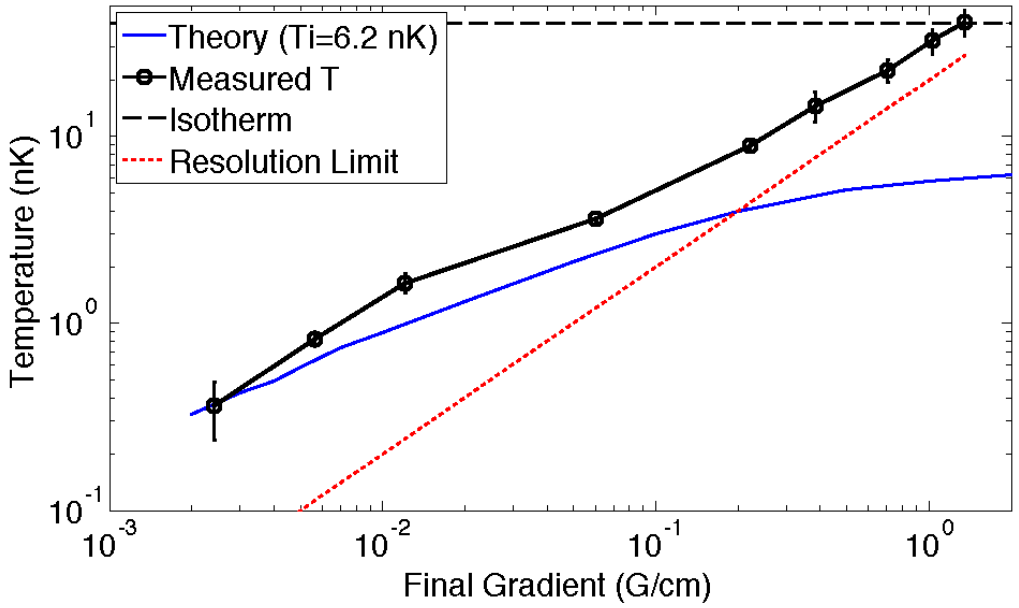

Figure 5-5: Plot of temperature vs. field gradient. Demonstration of spin gradient demagnetization cooling. Theoretical temperature and measured temperature vs. final magnetic field gradient, for the case of adiabatic gradient lowering in the superfluid state followed by lattice rampup. These measurements are the same as those plotted in Fig. 3. The dashed line follows the isothermal trajectory and the dotted line shows the optical resolution limit. The blue curve is the theoretical prediction, assuming an initial temperature of 6.2 nK and *not* including the effects of finite optical resolution.

of freedom is straightforward, as already discussed, but the particle-hole degrees of freedom are more complicated. To deal with them, we will follow the theoretical treatment from Refs. [29] and [35]. To calculate the partition function for the particle-hole degrees of freedom, we make two approximations: first, that $J = 0$, so that each site can be treated separately, and second, that the number of particles at a site is no more than one different than the $T = 0$ number, $n_0 = \lceil \mu/U \rceil$. This second approximation is called the particle-hole approximation, and gives a partition function

$$z_0 = 1 + \exp(-\beta(Un_0 - \mu)) + \exp(\beta(Un_0 - U + \mu)). \tag{5.6}$$

The particle-hole approximation is valid for $k_B T < 0.2U$, which is certainly true for the temperatures measured in our experiments. From this we can get the mean occupation number

$$\overline{n} \simeq n_0 + (\exp(-\beta(Un_0 - \mu)) - \exp(\beta(Un_0 - U + \mu)))/z_0. \tag{5.7}$$

Here we use the position-dependent chemical potential $\mu(r) = \mu - V_{trap}(r)$.

Now that we have both the partition function for the spin degrees of freedom (from equation 4.1) and the partition function for the particle-hole degrees of freedom, we can directly calculate the entropy of each as a function of temperature at varying gradients. Figure 5.6 shows calculated values for particle number and particle-hole entropy per site, while figure 5.7 shows a calculation of spin entropy per site and total entropy per site at a variety of gradients and temperatures. We can then plot a temperature vs. gradient curve given an initial temperature (which we treat as a fit parameter), a measurement of the total atom number and trap frequencies from our original data, and the assumption of fixed total entropy. The result is the fit curve shown in figures 5.4 and 5.5.

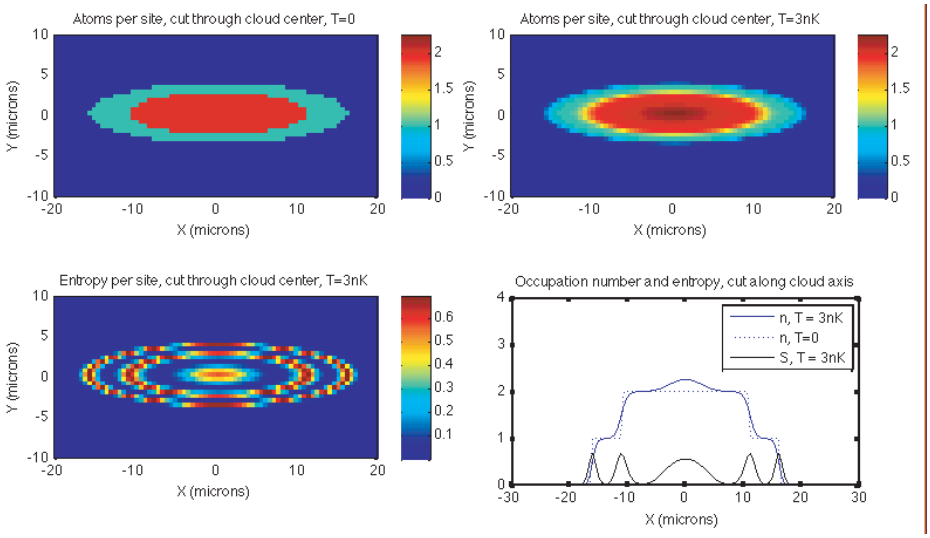

Figure 5-6: Particle-hole entropy distribution and number. The upper two plots show atom number as a function of position for two different temperatures, given our known trap frequencies and atom number. Each graph is a slice through the center of the trap. The lower right shows entropy per site for a the same slice. Finally, the lower right shows both atom number and entropy per site along a cut through the center.

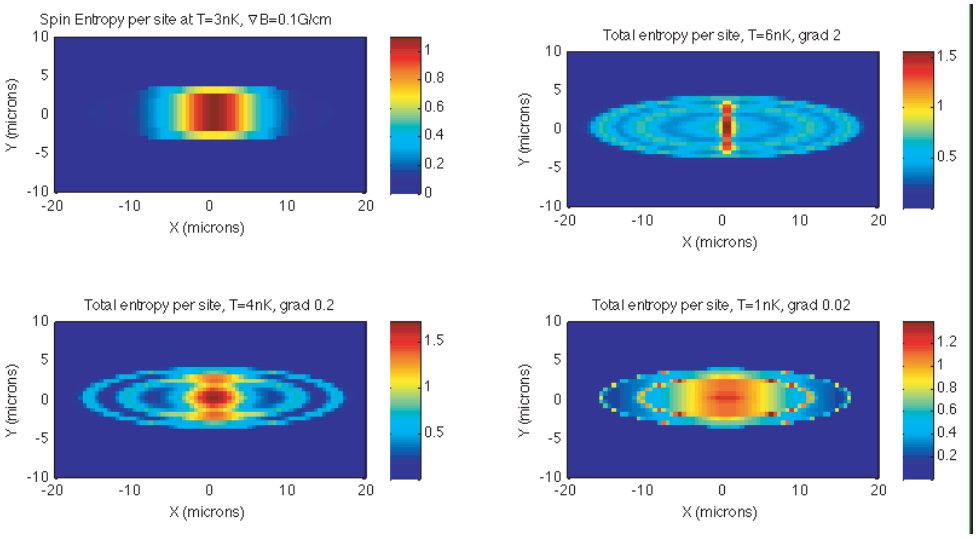

Figure 5-7: Spin entropy distribution. Calculated distributions of spin entropy per particle at various values of magnetic field gradient and temperature. The upper left diagram shows spin entropy alone, while the other three show total entropy, including both particle hole and spin entropies.

5.5 Equilibration and Adiabaticity

In the nonadiabatic path, lack of equilibration is a feature: we are interested in directly cooling the spins, so minimizing the thermal contact with the remainder of the system can only help. However, on the adiabatic path, we are interested in using the spins to cool the remainder of the system, so a lack of equilibration can be a serious obstacle. Hence, the degree to which the system remains in equilibrium along the adiabatic path is an important thing to assess. Since there are two steps along the path, we can estimate how well the atoms equilibrate along each of these steps by testing their reversibility. If a given step is adiabatic, it is reversible, and should also be in equilibrium at all times.

We have tested the reversibility of the gradient ramps used in spin gradient demagnetization cooling by decreasing, then increasing, then decreasing the gradient, and we observe no detectable difference between the resulting data and data produced by a single gradient ramp. This indicates that the gradient ramps used in spin gradient demagnetization cooling in the superfluid state are adiabatic, as is expected based on the trap frequencies (36, 141, and 156 Hz) and total demagnetization times (100 ms).

However, equilibration in the Mott insulator is more difficult to demonstrate because equilibration timescales get very long as the system approaches the Mott insulator transition. This makes it nearly certain that the system leaves equilibrium at some point during lattice rampup, so the question may really be whether this disequilibrium is significant. Still, the previously demonstrated agreement between spin gradient thermometry and trap width thermometry at high temperatures (as shown in chapter 4) indicates that the kinetic and spin degrees of freedom are reasonably well equilibrated in that regime. The strong fits in this colder regime to theoretical predictions is a further indication of good equilibration—both the hyperbolic tangent shape of the spin distribution and the good one-parameter fit to our model of

demagnetization (which assumes adiabaticity).

Nonetheless, when we perform the same test of reversibility on the lattice raising step as we did on the demagnetization step, heating is generally observed. Thus, we cannot rule out the existence of long-lived metastable excitations in the Mott insulating state which do not couple to the spin degrees of freedom and thus do not influence our temperature measurement. This result is consistent with other experiments which have also seen evidence of long equilibration times in the Mott insulator [41, 61]. On the bright side, the long lifetime of such excitations may mean they are so decoupled from the spin degrees of freedom as to be irrelevant to the bulk magnetic properties of the spin system. So if we are interested in using this cooling technique to observe spin ordering, these types of excitations may not interfere.

The reason for the poor equilibration of some of these excitations is the very small second-order tunneling rate, J^2/U, which for our system is on the order of $1Hz$ at the deepest lattice depths. How much of a problem this is depends on the degree of equilibration that happens at lower lattice depths, and how much remains to equilibrate above the Mott insulator transition. The same second-order tunneling rate governs the formation of spin-ordered domains, so the same problems would be faced if we were to try to achieve magnetic ordering in this system. Other, similar systems may not have so hard a time: for example, equilibration time of a lighter atomic species (e.g. ^7Li) would be faster by up to an order of magnitude due to the higher recoil energy, making such species ideal candidates for spin gradient demagnetization cooling.

5.6 Isothermal Demagnetization

An additional question closely related to the question of equilibration is the one posed in section 6 of chapter 4: why did the thermometry performed in those experiments

not show evidence of demagnetization cooling? In that section it was suggested that, although the experimental procedures of the thermometry were similar to those of demagnetization cooling, the very long time spent demagnetizing (about $1s$) may have allowed other heating processes to cancel it out.

To test this explanation, we set up our system in a way similar to our thermometry runs, and with higher optical trap depths to create similar starting temperatures (warmer than our best demagnetization runs). We then performed demagnetization runs alternately with fast demagnetization, as we normally do, and slow demagnetization, as we did in the original thermometry experiments. These showed a marked difference: the fast demagnetization runs showed cooling similar to what we have described above, while the slow demagnetization runs showed little to no cooling, producing an isothermal demagnetization just as we observed in our thermometry experiments. This indicates that our explanation in section 4-6 was probably accurate: demagnetization must be done rapidly, lest various uncontrolled heating mechanisms cancel it out and reduce it to an isothermal demagnetization. However, it is also worth noting that more aggressive demagnetization starting from the lowest possible initial temperature still showed some deviation from the isothermal line, even with the longer wait time. This suggests that some of our coldest results in the previous chapter, for example our quoted lowest temperature of 1 nK, may have inadvertently been the result of demagnetization cooling. The necessity of measuring these temperatures at very low gradients (to be able to resolve them optically) means also that they were subjuct to a large demagnetization, which may not all have been eliminated by heating before we imaged the atoms.

5.7 Future Prospects

Spin gradient demagnetization cooling represents a significant step forward in the field of quantum simulation. The lack of a method to cool atoms in an optical lattice has been an important stumbling block in the effort to probe Hamiltonians exhibiting quantum magnetism. Many cooling mechanisms have been proposed [6, 36, 37, 58], but await experimental realization. By contrast, the method presented here can be immediately implemented in existing experiments. We have demonstrated the ability to produce and measure spin distributions at arbitrary temperature by rapidly changing the magnetic field gradient applied to a two-component Mott insulator. In the same system, we have proposed and demonstrated a new cooling technique for the Mott insulator, based on adiabatic demagnetization of a domain wall prior to lattice rampup. This procedure has produced final temperatures of 300 pK, although we cannot rule out the presence of long-lived metastable excitations which do not couple to our thermometer. Ultimately, both of these techniques are capable of cooling a two-component Mott insulator below the superexchange temperature. It remains to be seen which technique will be of most use: the answer to this question depends on whether low spin temperature alone, or low temperature for the entire system is most important. However, the choice between these two techniques allows for the possibility of tailoring spin and particle-hole entropies to suit the needs of a given experiment. This opens a realistic path towards experimental observation of superexchange-driven phase transitions in optical lattices.

Chapter 6

Conclusion

It seems clear that quantum simulation will be a field of significant scientific interest and advancement in the coming years. The desire to understand quantum magnetic phenomena, especially those leading to exotic but incompletely understood behavours such as superconductivity, has attracted substantial interest in the field of ultracold atoms. The work presented in this thesis clears a significant hurdle in the path toward achieving these goals.

The development of spin gradient thermometry and spin gradient demagnetization cooling represents a significant step forward in the field of ultracold atoms. For the first time, we have the ability to measure temperatures in an optical lattice at whatever scale and precision we need. We also have the ability to cool atoms colder than ever before, with cooling of spin temperatures by a factor of 1000 within relatively easy reach. Moreover, the experimental technique is simple to implement and generalizable to nearly any system with at least two components with different magnetic moments. The cooling technique could even be used as a refrigerator for sympatetic cooling of a third species, if needed. The existence of these techniques, and the new realm of temperatures they allow, opens the door to new fields of study in quantum magnetism and simulation.

The next goal of the Rubidium lab will be to look for these orderings, beginning with the search for an xy-ferromagnetically ordered phase in the Mott insulator. To achieve this objective, a spin-dependent lattice will be implemented to tune the interactions between the two different spin states. In conjunction with the technique of spin gradient demagnetization cooling, advancements in this direction may be stunningly fast. However, other problems already touched on in this thesis, especially the long equilibration times observed in the Mott insulator, may hinder the observation of quantum magnetic phenomena in ^{87}Rb.

As an alternative approach, driven largely by the discoveries made while developing these techniques, a new lab is being founded in the Ketterle-Pritchard group to focus on using ^{7}Li in place of ^{87}Rb in an optical lattice. It is hoped that this substitution will be able to overcome the problem of equilibration we faced in ^{87}Rb. The high mass of ^{87}Rb made equilibration in the Mott insulator slow and uncertain; ^{7}Li's lower mass and correspondingly higher tunneling rate may help resolve this problem. All other things being equal, the tunneling rate near the Mott insulator transition is inversely proportional to the mass, so lighter elements have a natural advantage in this regard. Furthermore, the presence of usable Feschbach resonances in ^{7}Li, a feature lacking in ^{87}Rb, may allow the tuning of interactions without resorting to spin-dependent lattices. Still, regardless of which lab is best able to advance into this new regime, the outlook of the field is bright, and I have every expectation of success for both labs in the future.

Appendix A

Spin gradient thermometry for ultracold atoms in optical lattices

This appendix contains a reprint of Ref. [74]: David M. Weld, Patrick Medley, Hirokazu Miyake, David Hucul, David E. Pritchard, and Wolfgang Ketterle, *Spin gradient thermometry for ultracold atoms in optical lattices.* Phys. Rev. Lett., **103**(24):245301, (2009).

Spin Gradient Thermometry for Ultracold Atoms in Optical Lattices

David M. Weld, Patrick Medley, Hirokazu Miyake, David Hucul, David E. Pritchard, and Wolfgang Ketterle

MIT-Harvard Center for Ultracold Atoms, Research Laboratory of Electronics, and Department of Physics, Massachusetts Institute of Technology, Cambridge, Massachusetts 02139, USA

(Received 20 August 2009; revised manuscript received 10 October 2009; published 7 December 2009)

We demonstrate spin gradient thermometry, a new general method of measuring the temperature of ultracold atoms in optical lattices. We realize a mixture of spins separated by a magnetic field gradient. Measurement of the width of the transition layer between the two spin domains serves as a new method of thermometry which is observed to work over a broad range of lattice depths and temperatures, including in the Mott insulator regime. We demonstrate the thermometry using ultracold rubidium atoms, and suggest that interesting spin physics can be realized in this system. The lowest measured temperature is 1 nK, indicating that the system has reached the quantum regime, where insulating shells are separated by superfluid layers.

DOI: 10.1103/PhysRevLett.103.245301 PACS numbers: 67.85.−d, 03.75.Mn, 05.30.Jp, 75.10.Jm

Ultracold atoms trapped in optical lattices represent a new frontier for the investigation of many-body physics [1,2]. The existence of novel physics at decreasing energy scales drives the quest for lower temperatures in the atomic Mott insulator. Insulating Mott shells form at a temperature $T \sim 0.2U$, where U is the interaction energy. At the lower temperature $T \sim zJ$, where J is the tunneling amplitude and z is the number of nearest neighbors, the conducting layers become superfluid and the system enters a quantum insulator state [3]. At the even colder temperature scale $T \sim J^2/U$, superexchange-stabilized phases can exist in the two-component Mott insulator; this is the regime of quantum magnetism [4]. Various proposals [5,6] have focused on the realization of quantum spin Hamiltonians in this regime. Detection of superexchange-driven phase transitions in these systems remains a major goal of ultracold atomic physics. Perhaps the most important barrier to experimental detection of such a phase transition is the requirement of temperatures well below 1 nK [4]. Additional cooling methods [7–10] will be needed to reach this very interesting temperature scale. However, it is clear that to assess current methods and to validate future cooling techniques, low-temperature thermometry of the Mott insulator is needed.

Thermometry of systems in the Mott insulating state has remained a challenge [3,11–14]. In this Letter, we discuss and demonstrate a simple and direct method of thermometry using a magnetic field gradient which works in the two-component Mott insulator.

The theory behind this method of thermometry is straightforward. The system under consideration is an ensemble of atoms in a mixture of two hyperfine states loaded into a three-dimensional optical lattice in the presence of a weak magnetic field gradient. The two states have different magnetic moments, and are thus pulled towards opposite sides of the trapped sample by the gradient. At zero temperature, the spins will segregate completely, and a sharp domain wall will exist between the two spin domains (a small width due to superexchange coupling is typically negligible). This system has the same bulk physics as the single-component Mott insulator, but includes additional degrees of freedom in the form of spin excitations in the domain wall. At finite temperature, spin excitations will increase the width of the domain wall. This width will depend in a simple way on the field gradient, the differential Zeeman shift, and the temperature, and can thus be used as a thermometer.

For an incoherent mixture of two spins, the partition function for an individual lattice site can be approximately factorized as $Z = Z_\sigma Z_0$, where $Z_\sigma = \sum_\sigma \exp(-\beta \boldsymbol{\mu}_\sigma \cdot \mathbf{B}(x))$, β is $1/k_B T$, $\boldsymbol{\mu}_\sigma$ is the magnetic moment of the spin σ, $\mathbf{B}(x)$ is the spatially varying magnetic field, and Z_0 is the partition function of the particle-hole degrees of freedom (for which see [3]). This approximation is generally valid for the case of one atom per lattice site; for occupation number $n > 1$, it is valid when the mean of the intraspin interaction energies $\bar{U}_\sigma$ is equal to the interspin interaction energy $U_{\uparrow\downarrow}$, which is a good approximation in ^{87}Rb [15]. Since the total magnetization is fixed, the average value of the magnetic field is canceled by the corresponding Lagrange multiplier; we include this in the definition of $\mathbf{B}(x)$. We are free to treat the two states as having pseudospin $+1$ and -1; making that identification, the mean spin $\langle s \rangle$ as a function of position, gradient strength, and temperature has the simple form

$$\langle s \rangle = \tanh(-\beta \cdot \Delta\boldsymbol{\mu} \cdot \mathbf{B}(x)/2), \tag{1}$$

where $\Delta\boldsymbol{\mu}$ is the difference between the magnetic moments of the two states. A fit of the measured spin distribution with a function of this form will give the temperature of the system. When the Zeeman shift due to the magnetic field gradient is a linear function of position, imaging of the spin

distribution essentially corresponds to direct imaging of the Boltzmann distribution.

The apparatus used to produce ultracold ^{87}Rb atoms is described in Ref. [16]. After cooling, approximately 10^5 atoms are held in a far-red-detuned crossed optical dipole trap with trap frequencies between 100 and 200 Hz. A three-dimensional cubic optical lattice, formed by three retroreflected beams each of radius $\sim$150 μm, overlaps the trapping region. Since spin gradient thermometry does not depend on the number of atoms per lattice site n, we perform measurements at a range of n values between 1 and 4. The trapping and lattice beams are all derived from one fiber laser, with a wavelength λ of 1064 nm. Magnetic field gradients up to a few G/cm can be applied with external coils, and calibrated using Stern-Gerlach separation of the different spin states after release from the trap. The gradient is applied along the x direction, which is the weakest axis of the crossed dipole trap. Absorptive imaging of the atoms is performed with a camera pointing down along the vertical z axis.

The sequence of steps used to measure temperature is as follows. First, a sample of ^{87}Rb atoms in the $|F = 1, m_F = -1\rangle$ state is prepared by evaporation in the optical trap. Here F and m_F are the quantum numbers for the total spin and its projection on the z axis, respectively. The atoms are then placed into a mixture of the $|1, -1\rangle$ and $|2, -2\rangle$ states by a nonadiabatic magnetic field sweep through the microwave transition between the two states. This pair of states was chosen in order to avoid spin-exchange collisions. A magnetic field gradient of 2 G/cm is applied along the weak axis of the trap and results in additional evaporation, which is intended to remove the entropy created by the state preparation [17]. At this point, the field gradient is changed to the value to be used for measurement; lower gradients are used for lower-temperature measurements to keep the domain wall width larger than the imaging resolution. The optical lattice is then adiabatically ramped up, typically to a depth of $14.5E_R$, where $E_R = h^2/2m\lambda^2$ is the recoil energy and m is the atomic mass. The transition to the Mott insulator occurs at $13.5E_R$. At this point, the spin structure depends on the temperature as discussed above.

There are several ways to measure the resulting spin distribution. One way is to first take an image of the $F = 2$ atoms in the $14.5E_R$ lattice, then in a second run to illuminate the atoms with an optical repumper beam resonant with the $F = 1$ to $F' = 2$ transition for a few μs prior to imaging. This method gives an image of all atoms and an image of just the $F = 2$ atoms; appropriate subtraction can provide the spin distribution. It is possible to determine the temperature from a single image of one spin, but the data in this Letter were all taken using pairs of images to guard against systematic errors.

The temperature can then be measured by fitting the spin distribution to the hyperbolic tangent form. The resulting thermometer has high dynamic range and variable sensitivity, works at all accessible temperatures of interest, and requires only the simplest fitting procedures.

Figure 1 shows data of the type used for spin gradient thermometry. An image of the total atom density and an image of the spin density are obtained as discussed above. Both images are then integrated along the y direction, which is transverse to the gradient. The spin distribution is then fit by a function of the form $\rho(x)\tanh(\frac{3}{4}\beta\mu_B\frac{d|\mathbf{B}|}{dx}x)$, where $\rho(x)$ is the total density distribution. The only free parameters in this fit are a horizontal and vertical offset and the temperature $T = 1/k_B\beta$.

Figures 2 and 3 show the results of this thermometry on ultracold ^{87}Rb atoms in an optical lattice. Figure 2 shows the linear scaling of the inverse width of the domain wall as the magnetic field gradient is varied while holding the temperature constant. For widths larger than the optical resolution, the scaling is as predicted by Eq. (1). The two data sets plotted in Fig. 2 were taken at two different temperatures: 7 and 123 nK, according to the best-fit theoretical lines. Finite optical resolution or motion of the atoms during imaging will blur the measured spin profile and result in an overestimate of the domain wall width at high gradients. This effect was modeled by applying a Gaussian blur of radius 4 μm to the theoretical 7 nK spin profile at various gradients. The resulting curve, plotted as a dash-dotted line in Fig. 2, reproduces the saturation of measured width observed in the experimental data. The effect of finite resolution is always to overestimate the temperature.

Figure 3 shows the measured temperature plotted as a function of the power in the dipole trapping beam which confines the atoms in the direction of the magnetic field gradient (the x direction). Higher powers in this beam lead to less effective evaporation, and thus higher final tempera-

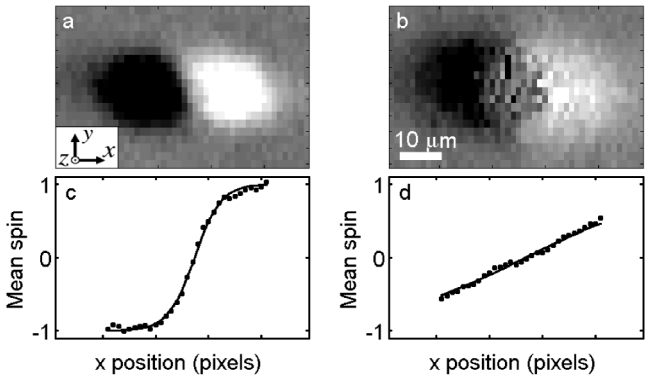

FIG. 1. Images used for spin gradient thermometry. Data on the left were taken at a lower optical trap power than data on the right. Panels (a) and (b) are images of the spin distribution. Panels (c) and (d) show the mean spin versus x position. The fit to (c) gives a temperature of 52 nK; the fit to (d) gives a temperature of 296 nK. The inset of (a) shows the axes referred to in the text. The bar in (b) is a size scale.

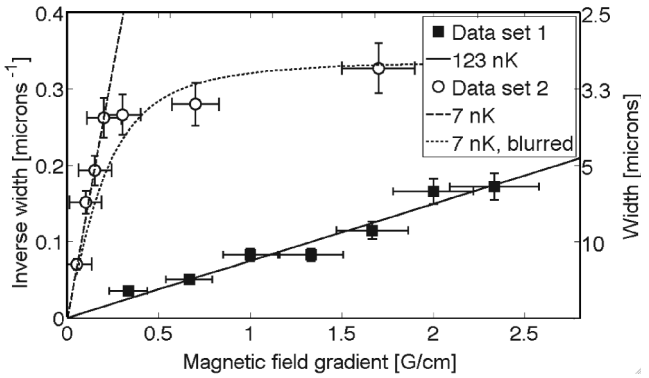

FIG. 2. Independence of the measured temperature on the applied field gradient. The inverse of the width of the spin profile is plotted as a function of magnetic field gradient for two data sets at two different temperatures. For constant temperature, a linear curve is expected. The width is defined as the distance from the center to the position where the mean spin is $1/2$. The solid (dashed) line assumes a temperature of 123 nK (7 nK) and perfect imaging. The measured width of the colder data set saturates at high gradient because of finite imaging resolution. The dotted line assumes a temperature of 7 nK and an imaging resolution of 4 μm.

tures. As a check of the new method of thermometry, Fig. 3 also presents an analysis of the same data using an existing method of thermometry, based on measurement of the in-trap width of the atomic cloud along the direction perpendicular to the gradient. This second method is based on the well-known relation $\sigma^2 = k_B T/m\omega^2$, where σ is the $1/e^2$ half-width of the atomic cloud and ω is the trap frequency

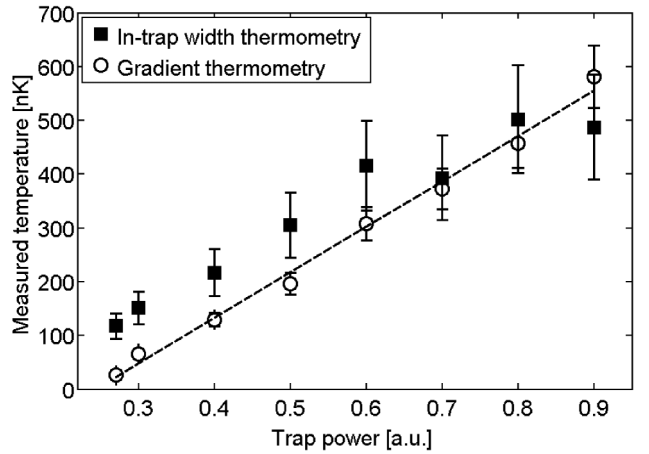

FIG. 3. Validation of spin gradient thermometry. Comparison of two measured temperatures versus final power in one of the optical trapping beams. Squares represent the results of in-trap cloud width thermometry, and circles represent the results of spin gradient thermometry (see text for details). Error bars represent estimated uncertainties. The dashed line is a linear fit to the spin gradient thermometry data. The closeness of this fit suggests that the temperature reached is proportional to the trap depth.

in the direction along which the width is measured [12]. The width is determined by a fit to the wings of the trapped cloud. Trap width thermometry is based on a noninteracting approximation, and will fail at temperatures less than U when the system starts to become incompressible. As in Ref. [12], all points on this plot are in the high-temperature single-band regime (T is less than the band gap but greater than the bandwidth). For the temperatures plotted in Fig. 3, the agreement between the two methods is reasonably good, and gives confidence in the use of spin gradient thermometry in regions of parameter space where no other thermometer exists.

The large dynamic range of spin gradient thermometry is evident in Fig. 3. Thermometry can be performed at temperatures so high that no condensate exists before lattice ramp-up. The lowest temperature we have measured was achieved by using the new thermometry as a feedback signal, enabling adjustment of experimental parameters for optimization of the final temperature in the Mott insulator. This method allowed us to achieve a measured temperature as low as 1 nK. At the lattice depth used here, U is 37 nK, and zJ is 6 nK. The measured temperature is thus well below $T_c = zJ$, the predicted critical temperature for the superfluid layer between the $n = 1$ and $n = 0$ Mott domains. According to the treatment of Ref. [3], at 1 nK the system should be well inside the quantum regime, with concentric quantum insulator shells separated by superfluid layers. This represents the first direct demonstration that this temperature regime has been achieved in the Mott insulator.

At a given value of the magnetic field gradient, very low temperatures will result in a width of the transition region smaller than the imaging optics can resolve (see Fig. 2). However, the width can be increased by decreasing the magnetic field gradient. The lowest measurable temperature will then depend on the minimum achievable gradient as well as the optical resolution, which are technical rather than fundamental limitations. In our apparatus, background gradients with all coils turned off are of order 10^{-3} G/cm, which, given our imaging resolution of a few μm, would in principle allow measurement of temperatures down to $\sim$50 pK or the superexchange scale, whichever is higher.

It is instructive to compare the useful range of this new method of thermometry with that of existing methods. To facilitate meaningful comparison with non-lattice-based methods, we discuss the range of entropy per particle S/Nk_B at which a given thermometer works, rather than the range of temperature. Condensate fraction thermometry works for $0.35 < S/Nk_B < 3.5$, where the lower limit is set by the difficulty of detecting a thermal fraction less than 10%, and the upper limit is set by disappearance of the condensate. Thermometry based on the thermal cloud size has a similar lower bound, but extends to arbitrarily high values of S/Nk_B. Quantitative thermometry based on the

visibility of interference peaks upon release from the lattice requires state-of-the-art quantum Monte Carlo calculations fitted to the data. This technique was recently used to measure temperatures as low as $0.08U$ in the superfluid phase near the Mott insulator transition [18]. This method cannot be applied deep in the Mott insulating state [11]. Measurement of the width of the conducting layers between the Mott shells is the only previously proposed method which works directly in the Mott insulating state [3,4,19]. However, this method requires tomographic techniques, and the useful range of entropy is rather narrow: $0.4 < S/Nk_B < \ln(2)$, where the upper limit is set by the melting of the Mott shells, and the lower limit is an estimate based on typical trapping parameters and optical resolution. Counting only spin excitations, the range of *spin* entropy per particle at which spin gradient thermometry works in our system is $0.1 < S_\sigma/Nk_B < \ln(2)$, where the lower limit is a function of optical resolution and sample size and the upper limit corresponds to the point at which the domain wall becomes as wide as the sample. It is important to note that spin gradient thermometry can work even if the entropy of the particle-hole excitations lies outside of this range in either direction. For example, spin gradient thermometry can work at arbitrarily high values of the total entropy per particle S/Nk_B, assuming the field gradient is increased to the point where $S_\sigma/Nk_B < \ln(2)$.

The method of thermometry presented here works because the two-component Mott insulator in a field gradient has a spectrum of soft and easily measurable spin excitations. The wide dynamic range of this method is a result of the fact that, in contrast to the gapped spectrum of the bulk one-component Mott insulator, the energy of the spin excitations can be tuned by adjusting the strength of the magnetic field gradient. The addition of a field gradient and a second spin component does not change the bulk properties of the Mott insulator and can be regarded as ''attaching'' a general thermometer to the first component.

The two-component Mott insulator in a field gradient is a rich system which can provide experimental access to novel spin physics as well as thermometry. In the work presented here, we have always allowed the spin distribution to equilibrate in the gradient before ramping up the optical lattice. However, changing the gradient after the atoms were already loaded into the lattice should open up several interesting scientific opportunities, in which the gradient is used to manipulate or perturb the atoms rather than as a diagnostic tool. If, for example, the gradient were suddenly changed after lattice ramp-up, one could probe nonequilibrium spin dynamics in a many-body quantum system. If the gradient were instead lowered adiabatically after ramp-up, adiabatic cooling of the Mott insulator could potentially be performed which, in contrast to [20], would not involve spin-flip collisions.

In conclusion, we have proposed and demonstrated a new method of thermometry for ultracold atoms in optical lattices. We have used the new method to measure temperatures in the Mott insulator as low as 1 nK. This temperature is to the best of our knowledge the lowest ever measured in a lattice, and it indicates that the system is deep in the quantum Mott regime.

The authors thank Eugene Demler, Takuya Kitagawa, David Pekker, and Lode Pollet for helpful discussions. This work was supported by the NSF, through a MURI program, and under ARO Grant No. W911NF-07-1-0493 with funds from the DARPA OLE program. H. M. acknowledges support from the NSF.

[1] I. Bloch, J. Dalibard, and W. Zwerger, Rev. Mod. Phys. **80**, 885 (2008).
[2] M. Lewenstein *et al.*, Adv. Phys. **56**, 243 (2007).
[3] F. Gerbier, Phys. Rev. Lett. **99**, 120405 (2007).
[4] T.-L. Ho and Q. Zhou, Phys. Rev. Lett. **99**, 120404 (2007).
[5] L. Duan, E. Demler, and M. Lukin, Phys. Rev. Lett. **91**, 090402 (2003).
[6] E. Altman, W. Hofstetter, E. Demler, and M. Lukin, New J. Phys. **5**, 113 (2003).
[7] M. Popp, J.-J. Garcia-Ripoll, K. G. Vollbrecht, and J. I. Cirac, Phys. Rev. A **74**, 013622 (2006).
[8] P. Rabl, A. J. Daley, P. O. Fedichev, J. I. Cirac, and P. Zoller, Phys. Rev. Lett. **91**, 110403 (2003).
[9] J.-S. Bernier *et al.*, Phys. Rev. A **79**, 061601 (2009).
[10] T.-L. Ho and Q. Zhou, Proc. Natl. Acad. Sci. U.S.A. **106**, 6916 (2009).
[11] L. Pollet, C. Kollath, K. V. Houcke, and M. Troyer, New J. Phys. **10**, 065001 (2008).
[12] D. McKay, M. White, and B. DeMarco, Phys. Rev. A **79**, 063605 (2009).
[13] A. Hoffmann and A. Pelster, Phys. Rev. A **79**, 053623 (2009).
[14] B. Capogrosso-Sansone, E. Kozik, N. Prokof'ev, and B. Svistunov, Phys. Rev. A **75**, 013619 (2007).
[15] For other atomic species, this treatment can readily be extended to include effects of finite $\Delta U = \bar{U}_\sigma - U_{\uparrow\downarrow}$. The leading correction changes the magnetic field gradient at the center of the sample B' to an effective gradient $B'(1 + (n-1)\Delta U/k_B T)$.
[16] E. W. Streed *et al.*, Rev. Sci. Instrum. **77**, 023106 (2006).
[17] C.-L. Hung, X. Zhang, N. Gemelke, and C. Chin, Phys. Rev. A **78**, 011604 (2008).
[18] S. Trotzky *et al.*, arXiv:0905.4882.
[19] S. Fölling, A. Widera, T. Müller, F. Gerbier, and I. Bloch, Phys. Rev. Lett. **97**, 060403 (2006).
[20] M. Fattori *et al.*, Nature Phys. **2**, 765 (2006).

Appendix B

Spin Gradient Demagnetization Cooling of Atoms in an Optical Lattice

This appendix contains a reprint of Ref. [5]: Patrick Medley, David M. Weld, Hirokazu Miyake, David E. Pritchard, and Wolfgang Ketterle, *Spin gradient demagnetization cooling of atoms in an optical lattice*. This paper is under revision and will be submitted for publication shortly.

Spin gradient demagnetization cooling of atoms in an optical lattice

BEC IV[1]

[1]*MIT-Harvard Center for Ultracold Atoms, Research Laboratory of Electronics, and Department of Physics, Massachusetts Institute of Technology, Cambridge MA 02139*

Attainment of lower temperatures has often led to discoveries of new physical phenomena. This observation has driven the search for new cooling methods which can be applied to neutral atoms in optical lattices. Such systems are expected to exhibit correlated magnetic quantum phases[1], but only below a Curie or Néel temperature which is typically on the order of 100 picokelvin. Realization of this low temperature in a lattice is a major goal of atomic physics. Here we present a general method of refrigeration which works in an optical lattice. We show that a time-varying magnetic field gradient applied to a lattice-trapped spin mixture can substantially cool the system. Cooling can be achieved either by nonadiabatic preparation of thermally isolated spin distributions at arbitrary (including negative) temperatures or by adiabatic reduction of the temperature of an equilibrated sample in a manner analogous to adiabatic demagnetization refrigeration[2,3]. We have prepared spin temperatures of +75 picokelvin and -75 picokelvin, and have used spin gradient demagnetization cooling to adiabatically reduce the temperature of an apparently equilibrated sample to 350 picokelvin, although the possibility of long-lived metastable excitations which do not couple to our thermometer cannot be ruled out. These are the lowest temperatures which have been

achieved in any system[4–6]. This new refrigeration technique appears to be capable of cooling below the Curie temperature of spin-ordered phases. These results open a realistic path to the observation of magnetic quantum phase transitions in optical lattices.

Application of a magnetic field gradient to a spin mixture will result in spatial segregation of the two spin components. In our experiments, these two spin domains always remain in thermal contact, with a "domain wall" of intermixed spins between them. In the Mott insulating state, the equilibrium spin distribution depends on the applied gradient $\nabla \mathbf{B}$ and the temperature T as $\langle s(x) \rangle = \tanh(-\beta \cdot \Delta \boldsymbol{\mu} \cdot \mathbf{B}(x)/2)$, where $\langle s(x) \rangle$ is the expectation value of the spin at position x, β is $1/k_B T$, and $\Delta \boldsymbol{\mu}$ is the difference between the magnetic moments of the two states. The recently developed technique of spin gradient thermometry[7] is based on the fact that the resulting domain wall width is proportional to T. The technique works because the two-component Mott insulator in a field gradient has a spectrum of soft and easily measurable spin excitations, the energy of which can be tuned by adjusting the strength of the magnetic field gradient.

This coupling between the applied gradient and the energy spectrum allows exploration of the system's response to a time-varying gradient. The gradient can be varied either quickly or slowly with respect to the spin relaxation timescale. If the gradient is changed in the deep Mott insulating state, the spin relaxation rate due to coupling to other degrees of freedom, which scales as J^2/U where J is the tunneling energy and U is the interaction energy, is so slow that the gradient can easily be varied much faster than the spin system can respond. This very slow relaxation enables the production of negative temperature distributions, and distributions with a very low

positive temperature typically set by the accuracy with which the field gradient can be measured. Conversely, if the gradient is changed at shallow or zero lattice depth, the spin relaxation is fast enough that adiabatic adjustment to the lowering of the gradient occurs. Fig. 1 shows these two possible paths in experimental phase space. Experiments performed in these two regimes give very different results.

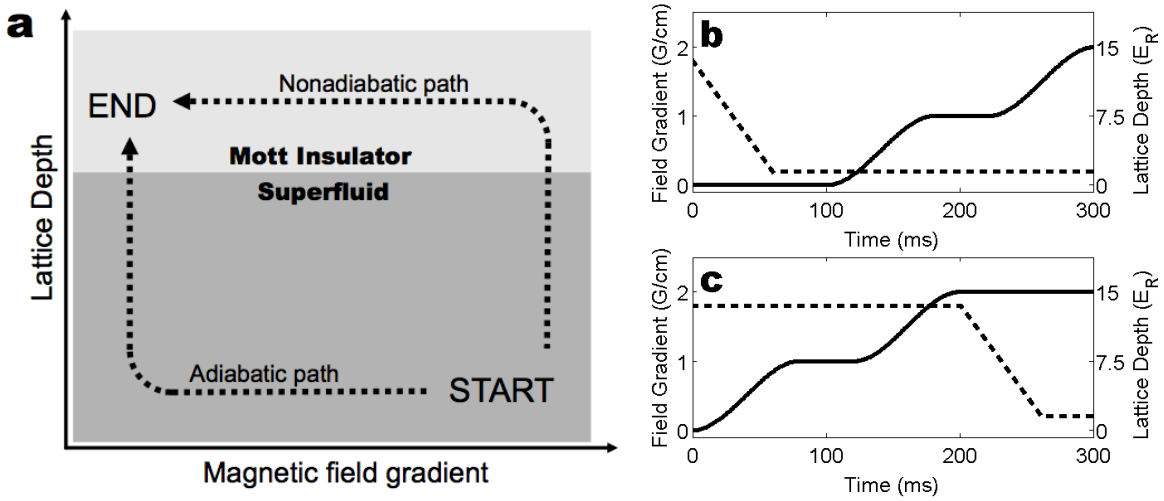

Figure 1: Details of two experimental cooling protocols. **a:** Experimental "phase diagram" of lattice depth vs. applied gradient. Dashed lines show two different paths along which one can move between the high-gradient superfluid state and the low-gradient Mott insulating state. **b:** Lattice depth (solid line) and gradient strength (dashed line) versus time for the lower path in panel **a**. **c:** Lattice depth (solid line) and gradient strength (dashed line) versus time for the upper path in panel **a**. The shape of the lattice rampup is designed to ensure maximum equilibration.

If instead of ensuring equilibration, we prevent it entirely, by lowering the gradient quickly deep in the Mott insulator, then the response of the system is so slow that we can achieve essen-

tially arbitrary spin temperatures. This includes negative temperatures. Figure 2 shows the results of such an experiment. Spin distributions at 75 pK and -75 pK have been prepared. Since the total energy is monotonic in $-1/T$, these temperatures represent the most extreme (coldest and hottest) thermodynamic states ever measured in spin systems[4,5]. The inset of Fig. 2 shows temperature versus hold time for both positive and negative spin distributions. If a negative temperature distribution is held for several seconds in the lattice, its temperature becomes more negative, as expected.

If the gradient is instead changed adiabatically, another intriguing possibility exists, which is based on an analogy with a common technique in experimental condensed matter physics: adiabatic demagnetization refrigeration[2,3]. Adiabatic demagnetization refrigeration in condensed matter systems typically makes use of a paramagnetic material, which is placed in a strong magnetic field and allowed to come to thermal equilibrium. The field is then slowly decreased, which reduces the energy of spin flip excitations and results in an effective increase in the heat capacity of the material. Energy and entropy flow from other degrees of freedom into the spin degrees of freedom; the non-magnetic degrees of freedom are thus cooled. In the two component Mott insulator, the total magnetization is fixed, so our proposed technique of "spin gradient demagnetization cooling" proceeds slightly differently. Instead of a magnetic field, a magnetic field *gradient* is reduced, which results in a decrease of the slope of the spin distribution. This decrease in slope can be thought of as an increase in the width of the domain wall between the spin-up and spin-down regions of the sample. Since each lattice site in the domain wall carries entropy, this pumps entropy into the domain wall from other (e.g. particle-hole) degrees of freedom, cooling them. If the initial

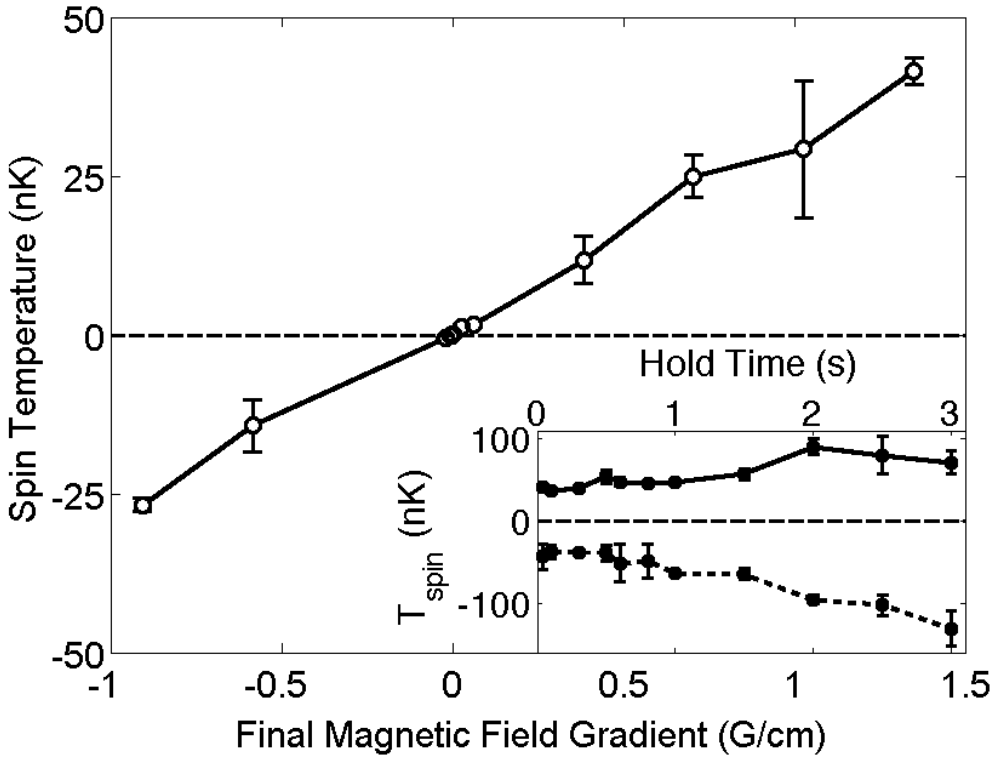

Figure 2: Preparation of arbitrary spin temperatures. **Main Plot:** measured spin temperature versus final gradient, for the case of rapid gradient change in the Mott insulating state. **Inset:** Temperature versus hold time in the lattice of spin distributions at negative (dashed line) and positive (solid line) initial temperature. Note that, as expected, the temperature of the negative distribution becomes more negative as it heats. Error bars are statistical.

entropy is low enough (less than about $k_{\mathrm{B}} \ln(2)$ per lattice site), then at some decreased value of the gradient all of the entropy of the system will be pumped into the domain wall. In principle, the entropy in the spin system could be removed at this point by optical pumping, resulting in a very cold single-component Mott insulator. Further adiabatic reduction of the gradient below this point cannot widen the domain wall further, and will thus linearly decrease the temperature of the spin

degrees of freedom.

The initial state of the system is a two-component BEC at zero lattice depth in a strong gradient. The gradient is adiabatically decreased, which cools the system as described above, and the lattice is then raised past the superfluid–Mott insulator transition. If the atoms are in a Mott insulator which is initially at a temperature low enough for the particle-hole approximation to hold, the maximum entropy per lattice site is about $k_{\mathrm{B}} \ln(2)$. The total entropy per site will be smaller by a factor of the ratio of conducting "shell" volume to total volume [8]. The maximum entropy per site for the spin degree of freedom in a very small gradient is $k_{\mathrm{B}} \ln(n+1)$, where n is the local number of indistinguishable bosons per site. For temperatures below the melting point of the Mott phase, the maximum heat capacity of the spin system is thus strictly larger than the heat capacity of the kinetic (i.e. particle-hole) degrees of freedom. This suggests that substantial cooling of the particle-hole degrees of freedom can be achieved with this method, even in a one-shot (non-cyclic) experiment. We have made a more quantitative analysis of the proposed technique by calculating entropy-versus-temperature curves of the two-component Mott insulator in various field gradients, using a model which is exact in the limit of no tunneling (manuscript in preparation). The results of these calculations (see theory curves in Figs. 3 and 4) confirm that spin gradient demagnetization cooling is in principle capable of reaching extremely low temperatures well below the expected Curie temperatures of spin-ordered states.

There are, however, both practical and theoretical limits on the temperatures which can be attained with spin gradient demagnetization cooling. In traditional magnetic refrigeration exper-

iments, the minimum temperature is often set by the minimum achievable magnetic field or the presence of unavoidable internal fields due to spin ordering in the material[9]. Analogues of both these limits are relevant to spin gradient demagnetization refrigeration. Practically, the ratio between the highest and lowest magnetic field gradients which can be applied to the system is an upper bound on the ratio between the initial and final temperatures. In our experiment, the maximum value of $\frac{\nabla B_i}{\nabla B_f}$ is about 1000, which would give a minimum temperature below 10 picokelvin assuming a typical initial temperature of 7 nanokelvin. Another limit on the lowest achievable temperature stems from the effects of spin coherence, which will start to become important near the Curie temperature of the spin-ordered phases. Spin correlations reduce the heat capacity of the spin degrees of freedom, because a magnetic domain containing multiple sites can only hold as much entropy as a single site could in the absence of correlations. These practical and theoretical limits on spin gradient demagnetization cooling do not appear to preclude cooling below the Curie temperature of the spin-ordered phases. This technique thus provides a specific and realistic method of realizing magnetic phase transitions in lattice-trapped ultracold atoms.

Figures 3 and 4 show the results of initial spin gradient demagnetization cooling experiments. As the field gradient is reduced, the width of the domain wall is observed to increase (see Fig. 3, indicating the transfer of entropy from the kinetic degrees of freedom to the spins. The width increases much less steeply than would be expected for an isothermal sample; this demonstrates cooling. The observed domain wall width can be converted to a temperature using spin gradient thermometry. The measured temperature falls rapidly as the gradient is lowered (see Fig. 4). The lowest measured temperature is 350 ± 50 picokelvin, which is within a factor of 2 of the expected

Curie temperature of the XY ferromagnet [10]. Theoretical curves in Figs. 3 and 4 show good agreement with the data. These curves were fitted to the measured data using only one variable parameter: the initial temperature at the maximum gradient. The initial temperature inferred from this fit is 7 nanokelvin. In light of these data, it seems possible that the 1 nanokelvin temperatures measured in our earlier work[7], which were observed at low field gradients, were in fact the result of adiabatic demagnetization cooling.

The idea behind spin gradient demagnetization cooling is straightforward, and if adiabaticity can be maintained then it is clear that cooling can be achieved. Our experimental protocol was designed to allow the system to equilibrate as much as possible at low lattice depths where the response times are short. However, equilibration timescales get very long as the system approaches the Mott insulator transition, and this can make it difficult to demonstrate perfect adiabaticity. We have tested the reversibility of the gradient ramps used in spin gradient demagnetization cooling by decreasing, then increasing, then decreasing the gradient, and we observe no detectable difference between the resulting data and data produced by a single gradient ramp. This indicates that the gradient ramps used in spin gradient demagnetization cooling in the superfluid state are adiabatic, as is expected based on the trap frequencies (36, 141, and 156 Hz) and total demagnetization times (100 ms). Equilibration in the Mott insulator is more difficult to demonstrate, although the previously demonstrated agreement between spin gradient thermometry and trap width thermometry at high temperatures[7] indicates that the kinetic and spin degrees of freedom are equilibrated in that regime. The fact that the spin distribution fits well to the hyperbolic tangent form expected of an equilibrated spin system is also indirect evidence for equilibration, as is the good one-parameter

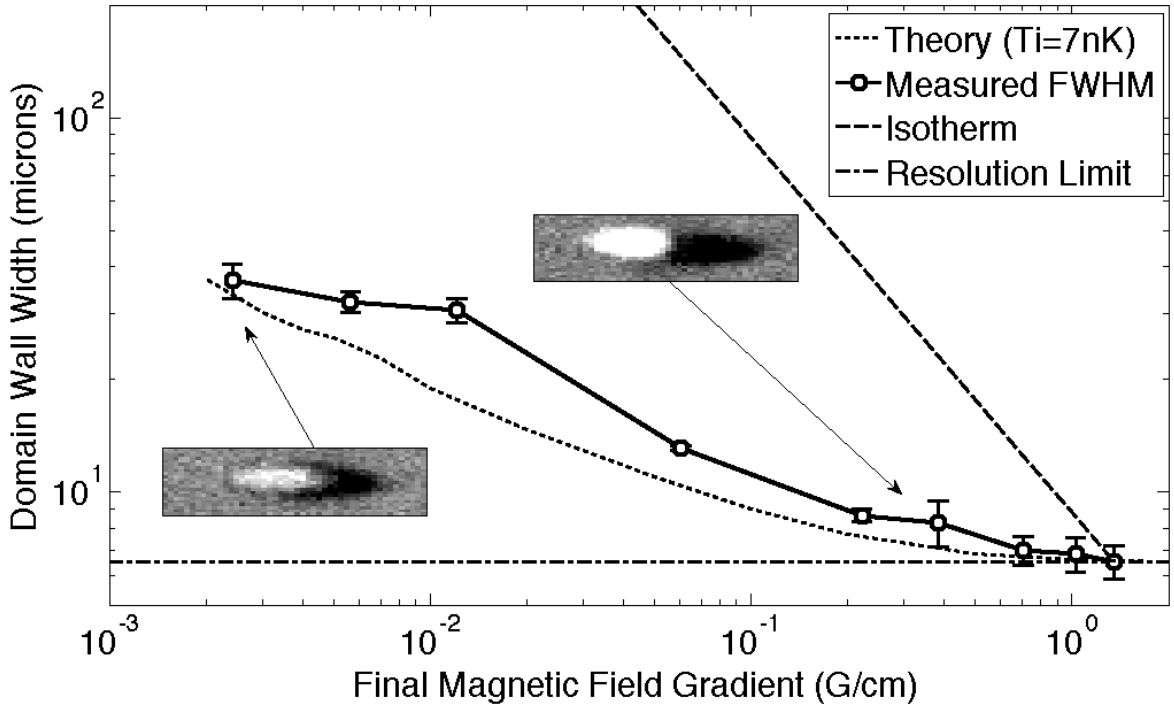

Figure 3: Demonstration of spin gradient demagnetization cooling. Circles represent measured domain wall width vs. final magnetic field gradient, for the case of adiabatic gradient lowering in the superfluid state followed by lattice rampup. Solid lines connect the points, and error bars are statistical. Insets show examples of spin images at the indicated point. The dashed line is an isotherm, meaning that it represents the expected widening behavior assuming no cooling. The dash-dotted line shows the minimum measurable width, given our optical resolution. The dotted curve is the theoretical prediction, assuming adiabatic demagnetization from an initial temperature of 7 nK and including the effects of finite optical resolution.

fit to our theoretical predictions (which assume adiabaticity). However, if the lattice is raised, then lowered to zero, then raised again, heating is generally observed. Thus, we cannot rule out the

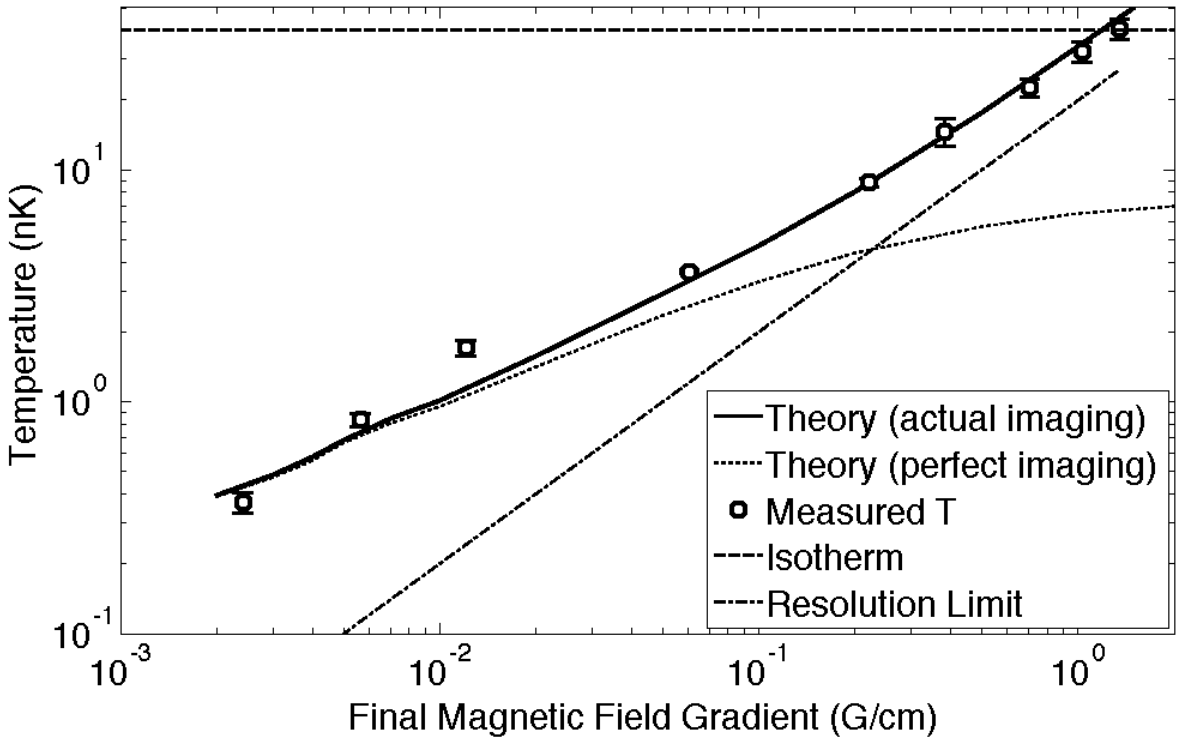

Figure 4: Demonstration of spin gradient demagnetization cooling. Circles represent measured temperature vs. final magnetic field gradient, for the case of adiabatic gradient lowering in the superfluid state followed by lattice rampup. Error bars are statistical. These measurements are the same as those plotted in Fig. 3. The dashed line follows the isothermal trajectory and the dash-dotted line shows the optical resolution limit. The solid line is the theoretical prediction, assuming an initial temperature of 7 nK and including the effects of finite optical resolution. The dotted line is the same theoretical prediction *without* the effects of optical resolution.

existence of long-lived metastable excitations in the Mott insulating state which do not couple to the spin degrees of freedom and thus do not influence our temperature measurement. Indeed, other experiments have seen evidence of long equilibration times in the Mott insulator[11,12]. However,

the long life of such excitations may mean they are so decoupled from the spin degrees of freedom as to be irrelevant to the bulk magnetic properties of the spin system. In this case, they would not prevent spin ordering. The slowest relevant timescale for the formation of spin-ordered domains is the second-order tunneling rate J^2/U (although dynamics in the single-component Mott insulator at the faster timescale of U have recently been observed)[13]. For ^{87}Rb at the highest lattice depths used in our system, this time is of order 1 Hz, although faster ordering could be achieved if, as is expected, some equilibration takes place at lower lattice depths. Additionally, equilibration time of a lighter atomic species (e.g. ^{7}Li) would be faster by up to an order of magnitude due to the higher recoil energy, making such species ideal candidates for spin gradient demagnetization cooling.

Although spin gradient demagnetization cooling was inspired by (and is locally similar to) magnetic refrigeration in condensed matter systems, there are important differences between the techniques. For example, it was generally believed that demagnetization cooling required spin-flips. However, spin gradient demagnetization cooling, because it uses a magnetic field gradient instead of a spatially homogeneous field, proceeds via spin transport in a system with fixed magnetization. In contrast to a previously reported technique in atomic systems[14], spin gradient demagnetization cooling involves no spin-flip collisions, and thus avoids heating effects associated with such collisions. On a practical level, it is easier to achieve very small magnetic field gradients than very small magnetic fields. In our system, an energy resolution of $k_B \times 25$ picokelvin can be relatively easily achieved with a gradient of 1 milligauss/cm and an optical resolution of 5 μm, while similar energy resolution in a homogeneous system would require control of the magnetic field at the microgauss level. Thus our results extend the applicability of magnetic refrigeration

techniques beyond their previously accepted limits.

The Hubbard Hamiltonian describing a mixture of pseudo-spin-1/2 bosons in a lattice can be reduced to an XXZ Heisenberg spin hamiltonian[1]. This observation has generated substantial interest in the possibility of studying magnetic phase transitions in such a system. Recent quantum Monte Carlo calculations studying the XY-ferromagnetic ground state in a system with the same parameters as our experiment indicate a critical entropy per particle of $0.35k_B$ and a critical temperature of 200 picokelvin at $U_{\uparrow\downarrow}/U_\sigma = 0.5$[10]. The critical entropy for the antiferromagnetic state is higher, at $0.5k_B$. The nonadiabatic cooling technique presented here has achieved spin temperatures and entropies well below these critical values, and the total entropies and temperatures we observe after adiabatic spin gradient demagnetization cooling are within reach of the critical values. This indicates the feasibility of achieving spin-ordering using one of these cooling techniques. It is not yet clear which of the two cooling methods is better suited to the production of spin-ordered states; the answer will depend on the achievable initial entropy and the ratio of heating timescales to ordering timescales.

Ultracold atoms trapped in optical lattices have the potential to be used as flexible quantum simulators of strongly interacting many-body systems. Progress in this field has depended upon the development of a cooling method which works in a lattice. Many such methods have been proposed[15–18] but await experimental realization. The method presented here can be immediately implemented in existing experiments. We have produced and measured spin distributions at arbitrary spin temperatures as low as 75 picokelvin by rapidly changing the magnetic field gra-

dient applied to a two-component Mott insulator. Using the same system, we have proposed and demonstrated an adiabatic cooling technique for the Mott insulator, based on demagnetization of a domain wall. Using the adiabatic cooling we have measured final equilibrated temperatures of 350 picokelvin, although we cannot rule out the presence of long-lived metastable excitations which do not couple to our thermometer. Ultimately, this technique is capable of cooling a two-component Mott insulator below the superexchange temperature. This work opens a realistic path towards experimental observation of superexchange-driven phase transitions in optical lattices.

Methods

The apparatus used to produce ultracold ^{87}Rb atoms is described elsewhere[19]. After being trapped and pre-cooled with RF evaporation, the atoms are delivered to the experimental vacuum chamber by translation of a far-detuned optical tweezer beam. The atoms are then loaded into a crossed optical dipole trap. Evaporation is performed by decreasing the power in the trapping beams, which cools the atoms below T_c, the critical temperature for Bose-Einstein condensation. The atoms are then placed into a mixture of the $|F = 1, m_F = -1\rangle$ and $|F = 2, m_F = -2\rangle$ hyperfine states by a nonadiabatic magnetic field sweep through the microwave transition between the states. Further evaporative cooling in a 2 Gauss/cm magnetic field gradient removes the entropy created by state preparation, and shifts the two spin states to opposite sides of the trap. A three-dimensional cubic optical lattice, formed by three retroreflected beams, overlaps the trapping region. This lattice is raised using the profile shown in Fig. 1, which includes a pause at intermediate lattice depths. This profile was observed to improve spin equilibration. Magnetic field gradients up to a few Gauss/cm

can be applied with external coils, and measured using Stern-Gerlach separation. The gradient is applied along the weak axis of the crossed dipole trap, and can point in either direction. The zero-crossing point is measured by observing the point at which the $|1,-1\rangle$ and $|2,-2\rangle$ atoms swap sides as the gradient is reversed in the superfluid state. Absorption imaging of the atoms is typically performed with a camera pointing down along the vertical axis, which is perpendicular to the direction of applied field gradient. In order to resolve the density profile of the optically dense thick atomic cloud, the saturation parameter of the imaging beam is typically greater than 1. The saturated images are corrected and calibrated according to a standard procedure[20].

1. Duan, L., Demler, E. & Lukin, M. Controlling spin exchange interactions of ultracold atoms in optical lattices. *Phys. Rev. Lett.* **91**, 090402 (2003).

2. Giauque, W. F. A thermodynamic treatment of certain magnetic effects. a proposed method of producing temperatures considerably below 1° absolute. *J. Amer. Chem. Soc.* **49**, 1864–1870 (1927).

3. Debye, P. Einige bemerkungen zur magnetisierung bei tiefer temperatur. *Ann. Phys.* **386**, 1154–1160 (1926).

4. Hakonen, P. J., Vuorinen, R. T. & Martikainen, J. E. Nuclear antiferromagnetism in rhodium metal at positive and negative nanokelvin temperatures. *Phys. Rev. Lett.* **70**, 2818–2821 (1993).

5. Tuoriniemi, J. T. *et al.* Double-spin-flip resonance of rhodium nuclei at positive and negative spin temperatures. *Phys. Rev. Lett.* **84**, 370–373 (2000).

6. Leanhardt, A. *et al.* Cooling bose-einstein condensates below 500 picokelvin. *Science* **301**, 1513 (2003).

7. Weld, D. M. *et al.* Spin gradient thermometry for ultracold atoms in optical lattices. *Phys. Rev. Lett.* **103**, 245301 (2009).

8. Ho, T.-L. & Zhou, Q. Intrinsic heating and cooling in adiabatic processes for bosons in optical lattices. *Phys. Rev. Lett.* **99**, 120404 (2007).

9. Oja, A. S. & Lounasmaa, O. V. Nuclear magnetic ordering in simple metals at positive and negative nanokelvin temperatures. *Rev. Mod. Phys.* **69**, 1–136 (1997).

10. Capogrosso-Sansone, B., Söyler, i. m. c. G., Prokof'ev, N. V. & Svistunov, B. V. Critical entropies for magnetic ordering in bosonic mixtures on a lattice. *Phys. Rev. A* **81**, 053622 (2010).

11. Hung, C.-L., Zhang, X., Gemelke, N. & Chin, C. Slow mass transport and statistical evolution of an atomic gas across the superfluid–mott-insulator transition. *Phys. Rev. Lett.* **104**, 160403 (2010).

12. Sensarma, R. *et al.* Lifetime of double occupancies in the Fermi-Hubbard model. *arXiv:1001.3881* (2010).

13. Greiner, M. Private communication.

14. Fattori, M. *et al.* Demagnetization cooling of a gas. *Nat Phys* **2**, 765–768 (2006).

15. Rabl, P., Daley, A. J., Fedichev, P. O., Cirac, J. I. & Zoller, P. Defect-suppressed atomic crystals in an optical lattice. *Phys. Rev. Lett.* **91**, 110403 (2003).

16. Bernier, J.-S. *et al.* Cooling fermionic atoms in optical lattices by shaping the confinement. *Phys. Rev. A* **79**, 061601 (2009).

17. Ho, T.-L. & Zhou, Q. Squeezing out the entropy of fermions in optical lattices. *Proceedings of the National Academy of Sciences* **106**, 6916–6920 (2009).

18. Ho, T. & Zhou, Q. Universal Cooling Scheme for Quantum Simulation. *arXiv:0911.5506* (2009).

19. Streed, E. W. *et al.* Large atom number bose-einstein condensate machines. *Rev. Sci. Instrum.* **77**, 023106 (2006).

20. Reinaudi, G., Lahaye, T., Wang, Z. & Guéry-Odelin, D. Strong saturation absorption imaging of dense clouds of ultracold atoms. *Opt. Lett.* **32**, 3143–3145 (2007).

Acknowledgements It is a pleasure to acknowledge discussions with Eugene Demler, Takuya Kitagawa, David Pekker, and Aditi Mitra.

Competing Interests The authors declare that they have no competing financial interests.

Correspondence Correspondence and requests for materials should be addressed to A.B.C. (email: abc@abc.edu).

Appendix C

Phase Diagram for a Bose-Einstein Condensate Moving in an Optical Lattice

This appendix contains a reprint of Ref. [53]: Jongchul Mun, Patrick Medley, Gretchen K. Campbell, Luis G. Marcassa, David E. Pritchard, and Wolfgang Ketterle, *Phase Diagram for a Bose-Einstein Condensate Moving in an Optical Lattice*. While not discussed in detail in this thesis, this paper is a good example of the sort of quantum simulation work already performed in this lab, and the desire to extend this work to two component systems led to the development of the cooling and thermometry techniques this thesis presents.

Phase Diagram for a Bose-Einstein Condensate Moving in an Optical Lattice

Jongchul Mun, Patrick Medley, Gretchen K. Campbell,* Luis G. Marcassa,† David E. Pritchard, and Wolfgang Ketterle

MIT-Harvard Center for Ultracold Atoms, Research Laboratory of Electronics, and Department of Physics, MIT, Cambridge, Massachusetts 02139, USA

(Received 26 June 2007; published 12 October 2007)

The stability of superfluid currents in a system of ultracold bosons was studied using a moving optical lattice. Superfluid currents in a very weak lattice become unstable when their momentum exceeds 0.5 recoil momentum. Superfluidity vanishes already for zero momentum as the lattice deep reaches the Mott insulator (MI) phase transition. We study the phase diagram for the disappearance of superfluidity as a function of momentum and lattice depth between these two limits. Our phase boundary extrapolates to the critical lattice depth for the superfluid-to-MI transition with 2% precision. When a one-dimensional gas was loaded into a moving optical lattice a sudden broadening of the transition between stable and unstable phases was observed.

DOI: 10.1103/PhysRevLett.99.150604 PACS numbers: 05.60.Gg, 03.75.Kk, 03.75.Lm, 05.30.Jp

The realization of condensed matter systems using ultracold atoms brings the precision and control of atomic physics to the study of many-body physics. Many studies have focused on Mott insulator physics, an important paradigm for the suppression of transport by particle correlations. Previous studies of the superfluid (SF)-to-Mott insulator (MI) transition in optical lattices with ultracold bosons [1–8] addressed the quenching of superfluidity below a critical lattice depth. Here we extend these studies into a second dimension by studying stability of superfluid current as a function of momentum and lattice depth as suggested in Ref. [9]. These transport measurements show the stability of superfluid at finite current, which is in nonequilibrium.

Transport measurements extend previous work on stationary systems in two regards. First, superfluidity near the MI transition has only been indirectly inferred from coherence measurements, whereas in this work, we characterize the superfluid regime by observing a critical current for superfluid flow through the onset of dissipation. Second, previous studies [1–8] were not able to precisely locate the phase transition, since the observed excitation spectrum and atomic interference pattern did not abruptly change [3,5,6], partially due to the inhomogeneous density. In contrast, the sudden onset of dissipation provides a clear distinction between the two quantum phases. In the SF phase, current flows without dissipation if the momentum does not exceed a critical momentum, while in the MI phase the critical momentum vanishes and transport is dissipative.

Bosonic atoms in an optical lattice are often described by the Bose-Hubbard Model where the tunneling between nearest neighbor lattice sites is characterized by the hopping matrix element J and the repulsive interactions by the on-site matrix element U [1,10–12]. The dimensionless interaction energy $u \equiv U/J$ determines the quantum phase of the system. For $u > u_c$, the system is in the MI phase, for $u < u_c$, the SF phase. u_c increases with the number of atoms N per site.

For weak interactions ($u \to 0$), the system approaches single-particle physics in a periodic potential well described by Bloch states and band structure. The critical momentum for a stable current-carrying state is 0.5 p_r ($p_r = h/\lambda$ is the recoil momentum of an atom, where λ is the wavelength of the optical lattice light) [13]. At the critical momentum, it becomes possible for two atoms in the same initial Bloch state to scatter into two other states and conserve energy and quasimomentum [14,15]. Instabilities in a 1D optical lattice were studied theoretically using a linear stability analysis of the Gross-Pitaevskii equation [13,16], and experimentally [14,17,18]. The theoretical studies predicted that for increasing lattice depth or increasing atomic interactions the stability of superfluid flow should increase [13,16]: the dynamic instability would stay near 0.5 p_r, whereas the Landau critical velocity and therefore the energetic instability would shift to larger momenta (For more discussions on dynamic and energetic instability, see Refs. [19,20]). However, these analyses neglect the growing importance of quantum correlations for larger lattice depth which leads to the SF-MI phase transition, where the critical momentum for a superfluid current vanishes. In this Letter, we study the decrease of the critical momentum from its value for the weakly interacting regime towards zero at the MI transition (Fig. 1).

Most studies of the SF-MI phase transition monitor the coherence in the superfluid phase through an interference pattern observed in the ballistic expansion resulting from a sudden turn-off of the confining potential and lattice. Previous observations of the phase transition found the experimental transition point to lie in the range between 10 and 13 E_R (with the recoil energy defined as $E_R = p_r^2/2m$, where m is the atomic mass) [3]. This uncertainty is related to the inhomogeneous density profile of trapped atoms and to the fact that the visibility of the interference extends beyond the transition point due to short-range coherence in the MI phase [6]. It has been suggested that observed kinks in the visibility are linked to the formation

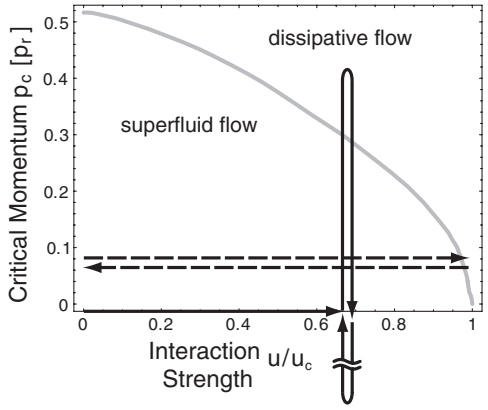

FIG. 1. Phase diagram showing the stability of superfluid flow in an optical lattice and the experimental procedure. The gray curve shows the predicted boundary between superfluid flow and dissipative flow phases for a three-dimensional gas with a commensurate filling of $N = 1$ atom per site [9]. The solid (dashed) arrows illustrate the experimental trajectory used for small (large) lattice depths (see text for details).

of the MI shells with occupation numbers $N = 2$ and 3 [6]. Several authors have suggested other features in the momentum distribution beyond coherent interference peaks as a more distinct signature of the phase transition [21,22]. Here we show that the disappearance of the critical momentum for superfluid flow provides such a signature and allows the determination of the transition point with high precision.

Our measurement was not limited by the inhomogeneous density profile. For our range of lattice depths, low critical momenta and the onset of dissipation occur only near the formation of MI shells with integer occupation numbers N [9]. The onset of dissipation related to the $N = 1$ domains occurs at smaller momentum than for other N domains. For instance, with increasing momentum p the $N = 1$ domain becomes unstable first, and this triggers dissipation over the whole atomic cloud [9]. Therefore, the breakdown of superfluid flow in the system was determined by the formation of the $N = 1$ domain and was not smeared out by the inhomogeneous density. Our criterion, the sudden onset of dissipation, depended on the formation of an insulating shell surrounded by a superfluid region, which occurs only in the inhomogeneous case.

In our experimental setup, a Bose-Einstein condensate (BEC) of ^{87}Rb atoms in the $5S_{1/2}$ $|1, -1\rangle$ state was prepared and trapped in a combination of an Ioffe-Pritchard magnetic trap and an optical dipole trap. The number of atoms in the BEC was typically 2×10^5. The magnetic trap frequencies were $\omega_{x,y} = 40$ Hz radially and $\omega_z = 4.6$ Hz axially. The laser beam for the optical dipole trap was oriented along the x axis. This laser beam was retroreflected and the polarization of the retroreflected beam was rotated in order to minimize interference between the two beams. Along the vertical direction (y axis) a lattice was formed by a retroreflected laser beam. For the z axis, a moving lattice was created by introducing a small frequency detuning δf between the two counterpropagating laser beams using acousto-optical modulators driven by phase-locked frequency generators. The 3D optical lattice was ramped up exponentially in 160 ms. All lattice beams were derived from the same laser operating at $\lambda = 1064$ nm and had an $1/e^2$ waist of 100–200 μm. The lattice depth was calibrated with 1% accuracy by applying a 12.5 μs lattice laser pulse to a BEC and comparing the observed Kapitza-Dirac diffraction pattern of a BEC to theory.

For transport measurements, we moved an optical lattice [17,23] which provides more flexibility to change the momentum than exciting a dipole oscillation by displacement of the BEC [24,25]. A moving optical lattice with velocity $v = \lambda \delta f/2$ was created along the long axis of the BEC by introducing a small frequency detuning δf between two counterpropagating lattice beams. If the velocity $v(t)$ changes slowly enough not to induce interband excitations, the initial Bloch state $|p = 0\rangle$ of the condensate in the optical lattice adiabatically evolves into the current-carrying state $|p(t) = -mv(t)\rangle$ where p is the quasimomentum. For increasing lattice depth, the effective mass of atoms $m^* = [\partial^2 E(p)/\partial p^2]^{-1}$ increases, and the group velocity $v_g = -(m/m^*)v(t)$ decreases. As a consequence, atoms prepared in a moving lattice with quasimomentum $p = -mv$ travel in the frame of the moving lattice with v_g and in the lab frame with velocity $\Delta v = v + v_g = (1 - m/m^*)v$, which approaches v in a deep lattice. Consequently, we observed that in a deep moving lattice atoms were dragged along to the edge of the trapping region limiting the experimental time scale to probe for dissipation. This became an issue for larger values of p and was addressed by first ramping up the lattice with $p = 0$ and then alternating the velocity of the moving lattice, thus performing a low-frequency ac transport measurement instead of dc.

We have used two sets of experimental procedures (Fig. 1), and our results were consistent for both. Close to the SF-MI phase transition, the lattice was increased to V_{latt} with a fixed (and small) value of momentum p (dashed arrows in Fig. 1). After a variable hold time t_{hold} at V_{latt} the lattice was ramped down to zero, and the magnetic trap switched off. After 33 ms of ballistic expansion, the atoms were imaged and the condensate fraction was determined as a function of momentum by using a bimodal fitting function. For smaller lattice depths, the lattice was ramped up with $p = 0$ (Fig. 1). Then a sinusoidal momentum modulation of the moving lattice with amplitude p_M was applied by modulating the frequency detuning δf between the counterpropagating lattice beams. The 10 ms period of this momentum modulation was slow enough to meet the adiabaticity condition, but fast enough to limit the displacement of the atomic cloud to less than a few μm. Both the trapping potential and the optical lattice were then turned off suddenly. After 33 ms of ballistic expansion, the condensate fraction of the center peak of the

superfluid interference pattern was recorded as a function of the momentum modulation amplitude p_M. Several cycles (typically, three to five) of the momentum modulation were applied to obtain a high contrast between the stable and dissipative regimes [Fig. 2(a)].

Figure 2(a) shows how the transition between superfluid and dissipative currents became sharper with increasing number of cycles of the momentum modulation. The critical momentum was determined from a log-log plot of the condensate fraction as a function of momentum p [Fig. 2(c)]. The intersection between two linear fit functions was taken as the critical momentum. Our result was found to be independent of the time period and number of cycles of the momentum modulation at a few percent level.

In the MI phase, stable superfluid flow is not possible and the critical momentum should vanish. However, using the procedure described above, we measured a small critical momentum of 0.02 p_r for lattice depths $V_{\mathrm{latt}} = 14$, 15, 16 E_R. Up to this momentum, the SF-MI phase transition remained reversible. We interpret the nonzero critical momentum as a finite-size effect. For our cloud size of 60 μm, the corresponding Heisenberg momentum uncertainty of 0.018 p_r agrees with our measured critical momentum. In cold atom experiments, some sloshing motion of the cloud in the trapping potential is unavoidable. The momentum uncertainty determined above indicates how much sloshing motion can be tolerated without affecting the observed phase transition.

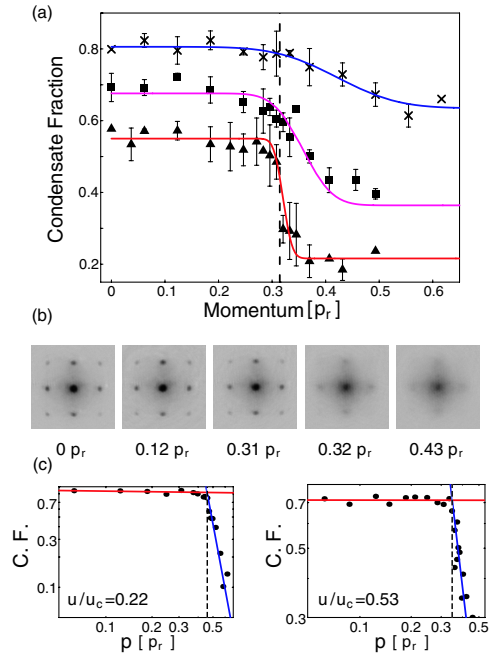

FIG. 2 (color online). Determination of the critical momentum of superfluid flow. Shown is the condensate fraction as a function of a momentum p. (a) Condensate fraction with $u/u_c = 0.61$ for a variable number of cycles of the momentum modulation (one cycle: × and blue line, two cycles: ■ and purple line, three cycles: ▲ and red line). A dashed vertical line indicates the critical momentum where instability begins to occur. The two and three-cycle data are offset vertically for clarity. These data were fitted with an error function to guide the eye. (b) Images of interference patterns released from an optical lattice at $u/u_c = 0.61$ moving with variable momentum. Instability occurred between $p = 0.31p_r$ and $0.32p_r$. Some of the triangular data points in (a) were obtained from these images. (c) Condensate fraction on a log-log scale for two different interaction strengths.

The critical lattice depth for the SF-MI phase transition can be determined as the point where the critical momentum vanishes. Using the predicted functional form [9] of the approach towards zero, $p_c \propto \sqrt{1 - u/u_c}$, as a fit function for the data points close to the SF-MI phase transition (the data points shown in the inset of Fig. 3) we determined the critical value $u_c = 34.2$ (± 2.0) corresponding to a lattice depth of 13.5(± 0.2) E_R. Our result agrees with the mean-field theory prediction $u_c = 5.8 \times 6 = 34.8$ for $N = 1$ SF-MI phase transition [1] and deviates by 2 σ from the predictions of $u_c = 29.34(2)$ of quantum Monte Carlo (QMC) simulation [26,27], which includes corrections beyond the mean-field theory. This demonstrates that our method has the precision to identify non-mean-field corrections. However, to turn precision into accuracy, experiments or QMC simulations [21,26,27] have to address corrections due to finite size, finite temperature, and finite time to probe the onset of the instability [27]. In our experiment, these corrections seemed to be small, but have not been characterized at the level of 1% in lattice depth.

The mean-field prediction for stable superfluid flow in 1D is similar to that for the 3D system [9]. However, it is well known that fluctuations play a much more important role in 1D. For studying a 1D system, we prepared an array of one-dimensional gas tubes by ramping two pairs of optical lattice beams up to lattice depths of $V_x = V_y = 30\ E_R$ suppressing hopping between the tubes. After a hold time of 10 ms, a moving optical lattice was ramped up along the z axis. As in our 3D experiment, a momentum modulation was applied, after which the moving optical lattice was ramped down to zero, followed by the other two optical lattices. The condensate fraction was determined after 33 ms of ballistic expansion as a function of the

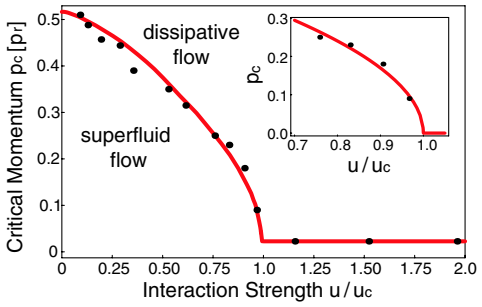

FIG. 3 (color online). Critical momentum for a condensate in a 3D lattice. The solid line shows the theoretical prediction for the superfluid region. The horizontal solid line is a fit to the data points in the MI phase. (Inset) Fit of critical momenta near the SF-MI phase transition.

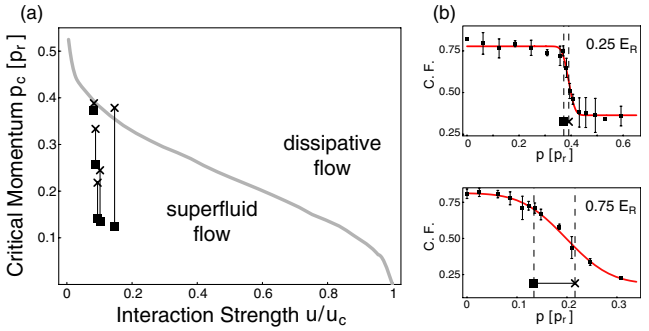

FIG. 4 (color online). Critical momentum for a 1D gas in an optical lattice. (a) The gray line indicates the mean-field theory prediction. The interaction strengths are normalized by the mean-field prediction for $u_c = 5.8 \times 2$ [1,4]. Squares (crosses) represent the measured critical momentum (the center of the transition). Measurements were taken at lattice depths of 0.25, 0.50, 0.75, 1.0, 2.0 E_R. The lines between crosses and squares indicate the width of the transition region. (b) Condensate fraction measured at 0.25 E_R and 0.75 E_R. The data were fitted with an error function. Squares (the critical momentum) and crosses (the center of the transition) are indicated on the plots.

momentum modulation amplitude. The critical momentum, where the onset of dissipation begins, was identified from a log-log plot as in the 3D case. Since the transitions became very broad, we characterized them by an error function fit, with the center of the fitted error function taken as the center of the transition (Fig. 4).

In the 1D system, at a very shallow lattice depth of 0.25 E_R (corresponding to $u/u_c = 0.08$) a sharp transition was observed, and the measured critical momentum agreed very well with the prediction [9,28] of a critical momentum of 0.39 p_r. However, a slight increase of the interaction strength (to $u/u_c = 0.09$ at a lattice depth of 0.5 E_R) led to a significant decrease of the critical momentum as well as a dramatic broadening of the transition as shown in Fig. 4. For lattice depths larger than 2 E_R, the transition became very broad and showed complex behavior, and we could not obtain quantitative fits. Our results show a significant deviation from the mean-field theory predictions and are in agreement with previous works [25,29,30].

The observed broadening of the transition confirms theoretical studies which emphasize the importance of quantum fluctuations in the 1D system. Quantum tunneling out of metastable states which are ignored in the mean-field description can lead to a decay of the superfluid current at very low momenta [28]. In addition to quantum fluctuations, thermal fluctuations provide a mechanism for current decay [28]. In our experiment, we used a "pure" BEC without a discernible thermal component. The close agreement with $T = 0$ predictions indicates that thermal fluctuations were not dominant.

In conclusion, we have used transport studies to connect a well-known dynamical instability for weakly interacting bosons with the equilibrium superfluid to Mott insulator transition. A comparison of 3D and 1D systems confirms the applicability of a mean-field description in three dimensions and the crucial importance of fluctuations in one dimension. The disappearance of superfluid currents at the SF-MI phase transition precisely located the phase transition. Our results illustrate the control and precision of condensed matter physics experiments done with ultracold atoms and their suitability to test many-body theories.

This work was funded by NSF through the grant for CUA. L. G. M. acknowledges support from Coordenacao de Aperfeicoamento de Pessoal de Nivel Superior. We thank E. Demler and A. Polkovnikov for insightful discussions, and David Weld for a critical reading of the manuscript.

*Present address: JILA, Boulder, Colorado 80309, USA.
†Permanent address: Instituto de Fisica de São Carlos, University of São Paulo, São Carlos, 13560-970, SP, Brazil.

[1] D. Jaksch *et al.*, Phys. Rev. Lett. **81**, 3108 (1998).
[2] C. Orzel *et al.*, Science **291**, 2386 (2001).
[3] M. Greiner *et al.*, Nature (London) **415**, 39 (2002).
[4] T. Stöferle *et al.*, Phys. Rev. Lett. **92**, 130403 (2004).
[5] S. Fölling *et al.*, Nature (London) **434**, 481 (2005).
[6] F. Gerbier *et al.*, Phys. Rev. Lett. **95**, 050404 (2005).
[7] G. K. Campbell *et al.*, Science **313**, 649 (2006).
[8] S. Fölling *et al.*, Phys. Rev. Lett. **97**, 060403 (2006).
[9] E. Altman *et al.*, Phys. Rev. Lett. **95**, 020402 (2005).
[10] M. P. A. Fisher *et al.*, Phys. Rev. B **40**, 546 (1989).
[11] W. Krauth, M. Caffarel, and J.-P. Bouchaud, Phys. Rev. B **45**, 3137 (1992).
[12] J. K. Freericks and H. Monien, Europhys. Lett. **26**, 545 (1994).
[13] B. Wu and Q. Niu, Phys. Rev. A **64**, 061603(R) (2001).
[14] G. K. Campbell *et al.*, Phys. Rev. Lett. **96**, 020406 (2006).
[15] K. M. Hilligsøe and K. Mølmer, Phys. Rev. A **71**, 041602(R) (2005).
[16] M. Modugno, C. Tozzo, and F. Dalfovo, Phys. Rev. A **70**, 043625 (2004).
[17] L. Fallani *et al.*, Phys. Rev. Lett. **93**, 140406 (2004).
[18] M. Cristiani *et al.*, Opt. Express **12**, 4 (2004).
[19] L. De Sarlo *et al.*, Phys. Rev. A **72**, 013603 (2005).
[20] B. Wu and J. Shi, arXiv:cond-mat/0607098.
[21] S. Wessel *et al.*, Phys. Rev. A **70**, 053615 (2004).
[22] V. A. Kashurnikov, N. V. Prokof'ev, and B. V. Svistunov, Phys. Rev. A **66**, 031601(R) (2002).
[23] M. Ben Dahan *et al.*, Phys. Rev. Lett. **76**, 4508 (1996).
[24] F. S. Cataliotti *et al.*, Science **293**, 843 (2001).
[25] C. D. Fertig *et al.*, Phys. Rev. Lett. **94**, 120403 (2005).
[26] J. K. Freericks and H. Monien, Phys. Rev. B **53**, 2691 (1996).
[27] B. Capogrosso-Sansone, N. V. Prokof'ev, and B. V. Svistunov, Phys. Rev. B **75**, 134302 (2007).
[28] A. Polkovnikov *et al.*, Phys. Rev. A **71**, 063613 (2005).
[29] A. Polkovnikov and D.-W. Wang, Phys. Rev. Lett. **93**, 070401 (2004).
[30] J. Ruostekoski and L. Isella, Phys. Rev. Lett. **95**, 110403 (2005).

Bibliography

[1] E. Altman, A. Polkovnikov, E. Demler, B. I. Halperin, and M. D. Lukin. Superfluid-insulator transition in a moving system of interacting bosons. *Phys. Rev. Lett.*, 95(2):020402, Jul 2005.

[2] Ehud Altman, Walter Hofstetter, Eugene Demler, and Mikhail D Lukin. Phase diagram of two-component bosons on an optical lattice. *New Journal of Physics*, 5(1):113, 2003.

[3] Ehud Altman, Walter Hofstetter, Eugene Demler, and Mikhail D Lukin. Phase diagram of two-component bosons on an optical lattice. *New Journal of Physics*, 5(1):113, 2003.

[4] M. H. Anderson, J. R. Ensher, M. R. Matthews, C. E. Wieman, and E. A. Cornell. Observation of bose-einstein condensation in a dilute atomic vapor. *Science*, 269(5221):198, July 1995.

[5] BECIV. Spin gradient demagnetization cooling of atoms in an optical lattice. *arXiv:to be submitted*, Jun 2010.

[6] Jean-Sébastien Bernier, Corinna Kollath, Antoine Georges, Lorenzo De Leo, Fabrice Gerbier, Christophe Salomon, and Michael Köhl. Cooling fermionic atoms in optical lattices by shaping the confinement. *Phys. Rev. A*, 79(6):061601, Jun 2009.

[7] Immanuel Bloch, Jean Dalibard, and Wilhelm Zwerger. Many-body physics with ultracold gases. *Rev. Mod. Phys.*, 80(3):885–964, Jul 2008.

[8] Micah Boyd, Erik W. Streed, Patrick Medley, Gretchen K. Campbell, Jongchul Mun, Wolfgang Ketterle, and David E. Pritchard. Atom trapping with a thin magnetic film. *Phys. Rev. A*, 76(4):043624, Oct 2007.

[9] Micah S Boyd. *Novel Trapping Techniques For Shaping Bose-Einstein Condensates*. PhD thesis, Massachusetts Institute of Technology, Cambridge, Massachusetts, Oct 2006.

[10] Gretchen K Campbell. *^{87}Rubidium Bose-Einstein Condensates in Optical Lattices*. PhD thesis, Massachusetts Institute of Technology, Cambridge, Massachusetts, Sep 2006.

[11] Gretchen K. Campbell, Aaron E. Leanhardt, Jongchul Mun, Micah Boyd, Erik W. Streed, Wolfgang Ketterle, and David E. Pritchard. Photon recoil momentum in dispersive media. *Phys. Rev. Lett.*, 94(17):170403, May 2005.

[12] Gretchen K. Campbell, Jongchul Mun, Micah Boyd, Patrick Medley, Aaron E. Leanhardt, Luis G. Marcassa, David E. Pritchard, and Wolfgang Ketterle. Imaging the Mott Insulator Shells by Using Atomic Clock Shifts. *Science*, 313(5787):649–652, 2006.

[13] Gretchen K. Campbell, Jongchul Mun, Micah Boyd, Erik W. Streed, Wolfgang Ketterle, and David E. Pritchard. Parametric amplification of scattered atom pairs. *Phys. Rev. Lett.*, 96(2):020406, Jan 2006.

[14] B. Capogrosso-Sansone, N. V. Prokof'ev, and B. V. Svistunov. Phase diagram and thermodynamics of the three-dimensional bose-hubbard model. *Phys. Rev. B*, 75(13):134302, Apr 2007.

[15] B. Capogrosso-Sansone, S. G. Soyler, N. V. Prokofev, and B. V. Svistunov. Counterflow superfluidity of two-species ultracold atoms in a commensurate optical lattice. *arXiv:0912.1865*, Dec 2009.

[16] Barbara Capogrosso-Sansone, Evgeny Kozik, Nikolay Prokof'ev, and Boris Svistunov. On-site number statistics of ultracold lattice bosons. *Phys. Rev. A*, 75(1):013619, Jan 2007.

[17] E. A. Cornell and C. E. Wieman. Nobel lecture: Bose-einstein condensation in a dilute gas, the first 70 years and some recent experiments. *Rev. Mod. Phys.*, 74(3):875–893, Aug 2002.

[18] Franco Dalfovo, Stefano Giorgini, Lev P. Pitaevskii, and Sandro Stringari. Theory of bose-einstein condensation in trapped gases. *Rev. Mod. Phys.*, 71(3):463–512, Apr 1999.

[19] K. B. Davis, M. O. Mewes, M. R. Andrews, N. J. van Druten, D. S. Durfee, D. M. Kurn, and W. Ketterle. Bose-einstein condensation in a gas of sodium atoms. *Phys. Rev. Lett.*, 75(22):3969–3973, Nov 1995.

[20] P. Debye. Einige bemerkungen zur magnetisierung bei tiefer temperatur. *Annalen der Physik*, 386(25):1154–1160, 1926.

[21] L.-M. Duan, E. Demler, and M. D. Lukin. Controlling spin exchange interactions of ultracold atoms in optical lattices. *Phys. Rev. Lett.*, 91(9):090402, Aug 2003.

[22] L.-M. Duan, E. Demler, and M. D. Lukin. Controlling spin exchange interactions of ultracold atoms in optical lattices. *Phys. Rev. Lett.*, 91(9):090402, Aug 2003.

[23] M. AU Fattori, T. AU Koch, S. AU Goetz, A. AU Griesmaier, S. AU Hensler, J. AU Stuhler, and T. Pfau. Demagnetization cooling of a gas. *Nature Phys.*, 2:765, 2006.

[24] S. Fölling, F. Gerbier, A. Widera, O. Mandel, T. Gericke, and I. Bloch. Quantum phase transition from a superfluid to a mott insulator in a gas of ultracold atoms. *Nature*, 415:39, 2002.

[25] S. Fölling, F. Gerbier, A. Widera, O. Mandel, T. Gericke, and I. Bloch. Spatial quantum noise interferometry in expanding ultracold atom clouds. *Nature*, 434:481, 2005.

[26] Simon Fölling, Artur Widera, Torben Müller, Fabrice Gerbier, and Immanuel Bloch. Formation of spatial shell structure in the superfluid to mott insulator transition. *Phys. Rev. Lett.*, 97(6):060403, Aug 2006.

[27] Simon Fölling, Artur Widera, Torben Müller, Fabrice Gerbier, and Immanuel Bloch. Formation of spatial shell structure in the superfluid to mott insulator transition. *Phys. Rev. Lett.*, 97(6):060403, Aug 2006.

[28] J. K. Freericks and H. Monien. Strong-coupling expansions for the pure and disordered bose-hubbard model. *Phys. Rev. B*, 53(5):2691–2700, Feb 1996.

[29] Fabrice Gerbier. Boson mott insulators at finite temperatures. *Phys. Rev. Lett.*, 99(12):120405, Sep 2007.

[30] Fabrice Gerbier, Artur Widera, Simon Fölling, Olaf Mandel, Tatjana Gericke, and Immanuel Bloch. Phase coherence of an atomic mott insulator. *Phys. Rev. Lett.*, 95(5):050404, Jul 2005.

[31] W. F. Giauque. Paramagnetism and the third law of thermo-dynamics. interpretation of the low-temperature magnetic susceptibility of gadolinium sulfate. *J. Amer. Chem. Soc.*, 49(8):1870–1877, 1929.

[32] A. Griffin, D.W. Snoke, and S. Stringari, editors. *Bose-Einstein Condensation*. Cambridge University Press, New York, 1995.

[33] P. J. Hakonen, R. T. Vuorinen, and J. E. Martikainen. Nuclear antiferromagnetism in rhodium metal at positive and negative nanokelvin temperatures. *Phys. Rev. Lett.*, 70(18):2818–2821, May 1993.

[34] D. M. Harber, H. J. Lewandowski, J. M. McGuirk, and E. A. Cornell. Effect of cold collisions on spin coherence and resonance shifts in a magnetically trapped ultracold gas. *Phys. Rev. A*, 66(5):053616, Nov 2002.

[35] Tin-Lun Ho and Qi Zhou. Intrinsic heating and cooling in adiabatic processes for bosons in optical lattices. *Phys. Rev. Lett.*, 99(12):120404, Sep 2007.

[36] Tin-Lun Ho and Qi Zhou. Squeezing out the entropy of fermions in optical lattices. *Proceedings of the National Academy of Sciences*, 106(17):6916–6920, 2009.

[37] Tin-Lun Ho and Qi Zhou. Universal cooling scheme for quantum simulation. *arXiv:0911.5506*, Nov 2009.

[38] Alexander Hoffmann and Axel Pelster. Visibility of cold atomic gases in optical lattices for finite temperatures. *Phys. Rev. A*, 79(5):053623, May 2009.

[39] David Hucul. Magnetic super-exchange with ultra cold atoms in spin dependent optical lattices. Master's thesis, Massachusetts Institute of Technology, Cambridge, Massachusetts, Jun 2009.

[40] Chen-Lung Hung, Xibo Zhang, Nathan Gemelke, and Cheng Chin. Accelerating evaporative cooling of atoms into bose-einstein condensation in optical traps. *Phys. Rev. A*, 78(1):011604, Jul 2008.

[41] Chen-Lung Hung, Xibo Zhang, Nathan Gemelke, and Cheng Chin. Slow mass transport and statistical evolution of an atomic gas across the superfluid–mott-insulator transition. *Phys. Rev. Lett.*, 104(16):160403, Apr 2010.

[42] D. Jaksch, C. Bruder, J. I. Cirac, C. W. Gardiner, and P. Zoller. Cold bosonic atoms in optical lattices. *Phys. Rev. Lett.*, 81(15):3108–3111, Oct 1998.

[43] W. Ketterle, D. S. Durfee, and D. M. Stamper-Kurn. Making, probing and understanding bose-einstein condensates. *Varenna Summer School*, 1999.

[44] Wolfgang Ketterle. Nobel lecture: When atoms behave as waves: Bose-einstein condensation and the atom laser. *Rev. Mod. Phys.*, 74(4):1131–1151, Nov 2002.

[45] A. B. Kuklov and B. V. Svistunov. Counterflow superfluidity of two-species ultracold atoms in a commensurate optical lattice. *Phys. Rev. Lett.*, 90(10):100401, Mar 2003.

[46] A. E. Leanhardt, T. A. Pasquini, M. Saba, A. Schirotzek, Y. Shin, D. Kielpinski, D. E. Pritchard, and W. Ketterle. Cooling Bose-Einstein Condensates Below 500 Picokelvin. *Science*, 301(5639):1513–1515, 2003.

[47] Anthony J. Leggett. Bose-einstein condensation in the alkali gases: Some fundamental concepts. *Rev. Mod. Phys.*, 73(2):307–356, Apr 2001.

[48] M. Lewenstein, A. Sanpera, V. Ahufinger, B. Damski, A. Sen, and U. Sen. Ultracold atomic gases in optical lattices: mimicking condensed matter physics and beyond. *Advances in Physics*, 56(2):243–379, Jul 2007.

[49] Olaf Mandel, Markus Greiner, Artur Widera, Tim Rom, Theodor W. Hänsch, and Immanuel Bloch. Coherent transport of neutral atoms in spin-dependent optical lattice potentials. *Phys. Rev. Lett.*, 91(1):010407, Jul 2003.

[50] M. P. Marder. *Condensed Matter Physics*. Wiley Interscience, New York, 2000.

[51] D. McKay, M. White, and B. DeMarco. Lattice thermodynamics for ultracold atoms. *Phys. Rev. A*, 79(6):063605, Jun 2009.

[52] Jongchul Mun. *Bose-Einstein Condensates in Optical Lattices: The Superfluid to Mott Insulator Phase Transition*. PhD thesis, Massachusetts Institute of Technology, Cambridge, Massachusetts, May 2008.

[53] Jongchul Mun, Patrick Medley, Gretchen K. Campbell, Luis G. Marcassa, David E. Pritchard, and Wolfgang Ketterle. Phase diagram for a bose-einstein condensate moving in an optical lattice. *Phys. Rev. Lett.*, 99(15):150604, Oct 2007.

[54] C. Orzel, A. K. Tuchman, M. L. Fenselau, M. Yasuda, and M. A. Kasevich. Squeezed States in a Bose-Einstein Condensate. *Science*, 291(5512):2386–2389, 2001.

[55] C. J. Pethick and H. Smith. *Bose-Einstein Condensation in Dilute Gases*. Cambridge University Press, New York, 2002.

[56] Lode Pollet, Corinna Kollath, Kris Van Houcke, and Matthias Troyer. Temperature changes when adiabatically ramping up an optical lattice. *New Journal of Physics*, 10(6):065001, 2008.

[57] M. Popp, J.-J. Garcia-Ripoll, K. G. Vollbrecht, and J. I. Cirac. Ground-state cooling of atoms in optical lattices. *Phys. Rev. A*, 74(1):013622, Jul 2006.

[58] P. Rabl, A. J. Daley, P. O. Fedichev, J. I. Cirac, and P. Zoller. Defect-suppressed atomic crystals in an optical lattice. *Phys. Rev. Lett.*, 91(11):110403, Sep 2003.

[59] G. Reinaudi, T. Lahaye, Z. Wang, and D. Guéry-Odelin. Strong saturation absorption imaging of dense clouds of ultracold atoms. *Opt. Lett.*, 32(21):3143–3145, 2007.

[60] C. M. Savage and M. P. Das, editors. *Bose-Einstein Condensation*. World Scientific, London, 2000.

[61] R. Sensarma, D. Pekker, E. Altman, E. Demler, N. Strohmaier, D Greif, R J/"ordens, L. Tarruell, H. moritz, and T. Esslinger. Lifetime of double occupancies in the fermi-hubbard model. *arXiv:1001.3881*, Jan 2010.

[62] J. Shlens. A tutorial on principal component analysis.

[63] L. I. Smith. A tutorial on principal component analysis.

[64] Dan M Stampur-Kurn. *Peeking and poking at a new quantum fluid: Studies of gaseous Bose-Einstein condensates in magnetic and optical traps*. PhD thesis, Massachusetts Institute of Technology, Cambridge, Massachusetts, Feb 2000.

[65] J. Steinhauer, R. Ozeri, N. Katz, and N. Davidson. Excitation spectrum of a bose-einstein condensate. *Phys. Rev. Lett.*, 88(12):120407, Mar 2002.

[66] Thilo Stöferle, Henning Moritz, Christian Schori, Michael Köhl, and Tilman Esslinger. Transition from a strongly interacting 1d superfluid to a mott insulator. *Phys. Rev. Lett.*, 92(13):130403, Mar 2004.

[67] Erik W Streed. ^{87}*Rubidium Bose-Einstein condensates: Machine Construction and Quantum Zeno Experiments*. PhD thesis, Massachusetts Institute of Technology, Cambridge, Massachusetts, Jan 2006.

[68] Erik W. Streed, Jongchul Mun, Micah Boyd, Gretchen K. Campbell, Patrick Medley, Wolfgang Ketterle, and David E. Pritchard. Continuous and pulsed quantum zeno effect. *Phys. Rev. Lett.*, 97(26):260402, Dec 2006.

[69] EW Streed, AP Chikkatur, TL Gustavson, M Boyd, Y Torii, D Schneble, GK Campbell, DE Pritchard, and W Ketterle. Large atom number Bose-Einstein condensate machines. *REVIEW OF SCIENTIFIC INSTRUMENTS*, 77(2), FEB 2006.

[70] S. Trotzky, L. Pollet, F. Gerbier, U. Schnorrberger, I. Bloch, N. V. Prokof'ev, B. Svistunov, and M. Troyer. Suppression of the critical temperature for superfluidity near the Mott transition: validating a quantum simulator. *ArXiv:0905.4882*, May 2009.

[71] J. T. Tuoriniemi, T. A. Knuuttila, K. Lefmann, K. K. Nummila, W. Yao, and F. B. Rasmussen. Double-spin-flip resonance of rhodium nuclei at positive and negative spin temperatures. *Phys. Rev. Lett.*, 84(2):370–373, Jan 2000.

[72] Matthew Turk and Alex Pentland. Eigenfaces for recognition. *Journal of Cognitive Neuroscience*, 3(1):71–86, 1991.

[73] E. G. M. van Kempen, S. J. J. M. F. Kokkelmans, D. J. Heinzen, and B. J. Verhaar. Interisotope determination of ultracold rubidium interactions from three high-precision experiments. *Phys. Rev. Lett.*, 88(9):093201, Feb 2002.

[74] David M. Weld, Patrick Medley, Hirokazu Miyake, David Hucul, David E. Pritchard, and Wolfgang Ketterle. Spin gradient thermometry for ultracold atoms in optical lattices. *Phys. Rev. Lett.*, 103(24):245301, Dec 2009.